Washington University in St. Louis
Washington University Open Scholarship

Arts & Sciences Electronic Theses and Dissertations

Arts & Sciences

Summer 8-15-2019

Magic Angle Spinning Spheres and Improved Microwave Coupling for Magnetic Resonance

Pin-Hui Chen
Washington University in St. Louis

Follow this and additional works at: https://openscholarship.wustl.edu/art_sci_etds

 Part of the Engineering Commons, and the Physical Chemistry Commons

Recommended Citation

Chen, Pin-Hui, "Magic Angle Spinning Spheres and Improved Microwave Coupling for Magnetic Resonance" (2019). *Arts & Sciences Electronic Theses and Dissertations*. 1893.
https://openscholarship.wustl.edu/art_sci_etds/1893

This Dissertation is brought to you for free and open access by the Arts & Sciences at Washington University Open Scholarship. It has been accepted for inclusion in Arts & Sciences Electronic Theses and Dissertations by an authorized administrator of Washington University Open Scholarship. For more information, please contact digital@wumail.wustl.edu.

WASHINGTON UNIVERSITY IN ST. LOUIS

Department of Physics

Dissertation Examination Committee:
Kater Murch, Chair
Alexander B. Barnes
Anders E. Carlsson
Sophia E. Hayes
Erik Henriksen

Magic Angle Spinning Spheres and Improved Microwave Coupling for Magnetic Resonance

by
Pin-Hui Chen

A dissertation presented to
The Graduate School
of Washington University in
partial fulfillment of the
requirements for the degree
of Doctor of Philosophy

August 2019
St. Louis, Missouri

© 2019, Pin-Hui Chen

Table of Contents

List of Figures

List of Tables

Acknowledgments

First, I would like to thank my advisor Professor Alexander Barnes for his guidance over the past few years. I always enjoy having science discussions and brainstorming with him. He has provided a nice collaborative environment in the lab and given me great opportunities to attend conferences and to work in Germany.

Many thanks to my dissertation committee members, Professors Kater Murch, Erik Henriksen, Anders Carlsson, and Sophia Hayes, who have provided great feedback on my research. Special thanks to Kater about helpful discussions on microwave simulations before my qualifying exam.

I always feel lucky to work with so many great people in the Barnes Lab. I would like to thank Dr. Brice Albert and Dr. Faith Scott for teaching me how to use Inventor when I joined the lab. Dr. Chukun Gao has helped me a lot with the microwave simulations. Working with Dr. Erika Sesti, Dr. Eddie Saliba, Patrick Judge, Nick Alaniva, Lauren Price, Nathan Soper, Dr. Tom Popp, and Dr. Sarah Overall has been fun because they always have great ideas when we talk about science.

I would like to thank our collaborators in Germany. Many thanks to Professor Jan Korvink, Dr. Vlad Badilita, and Professor Jens Anders for providing great work environments and giving me helpful advice. I also thank the colleagues I worked with at KIT and University of Stuttgart. Science discussions with them were always fun and helpful.

I would also like to thank those friends in St. Louis who made my life so colorful. I did not know anyone four years ago when I moved here. So many friends helped me start the new life and explore the city. Now they are like my family here. My Ph. D journey would not have been so great had I not have met them.

Finally, I would like to thank my family and friends back in Taiwan who have always been very supportive. My parents' encouragement helped me go through the hard times within these four

years. My uncle and aunt, who are great scientists, have motivated me to come to the States for my Ph. D ever since I was a kid. I would not have become the scientist I am today without them.

Pin-Hui Chen (Sabrina)

Washington University in St. Louis

August 2019

Dedicated to my family,
for their love and support.

ABSTRACT OF THE DISSERTATION

Magic Angle Spinning Spheres and Improved Microwave Coupling for Magnetic Resonance

by

Pin-Hui Chen

Doctor of Philosophy in Department of Physics

Washington University in St. Louis, 2019

Professor Kater Murch, Chair

Nuclear magnetic resonance (NMR) is a nondestructive technique used to characterize molecular structure and dynamics with atomic resolution. In solid-state NMR, magic angle spinning (MAS) is commonly implemented to improve spectral resolution by partially averaging anisotropic interactions. To further improve NMR sensitivity, dynamic nuclear polarization (DNP) is utilized to transfer the polarization from electron spins to nuclei of interest using microwaves. Advanced MAS DNP NMR instrumentation, such as spherical rotors for stable and fast spinning, dielectric lenses to effectively couple the microwaves into the sample, and the separation of receiving and transmitting circuits to decrease measurement noise, are developed to improve NMR resolution and sensitivity in different aspects. The stable spinning of 9.5 mm outer diameter (OD) spherical rotors is demonstrated at 10.6 kHz with helium gas. 240 μm OD spherical rotors and stators can be fabricated by three-dimensional direct laser writing (3D-DLW) for ultra-fast MAS. Moreover, dielectric lenses for cylindrical and spherical rotors are analyzed to increase electron Rabi frequencies. A double-lens insert and 0.5 mm diamond spheres are proposed as potential strategies to improve microwave coupling. To effectively decrease NMR measurement noise, the receiving and transmitting circuits of the probe are separated along with placing the pre-amplifier in close proximity to the receive coil. This design can lead to an improved signal-to-noise ratio. The

improved MAS DNP NMR instrumentation will allow for sufficient sensitivity to investigate complicated biological systems.

Chapter 1: Introduction

1.1 Nuclear Magnetic Resonance (NMR)

Nuclear magnetic resonance (NMR) is a technique that probes the nuclear spin states of NMR-active nuclei (spin ½ or higher). When an NMR-active nucleus is exposed to an external magnetic field at a resonant frequency, the nuclear spins can be manipulated and detected. Analyzing the induced electromagnetic signals that contains information about the molecules enables characterization of molecular structure and dynamics with atomic resolution.

1.1.1 Zeeman Interaction and Polarization

The NMR Hamiltonian contains several interactions- among them include the Zeeman interaction, dipolar coupling, and chemical shift anisotropy. At high magnetic fields, the Zeeman interaction dominates the NMR Hamiltonian and the other interactions act as perturbations to the Zeeman interaction.

Nuclear spins interact with a magnetic field through the Zeeman interaction. The Zeeman Hamiltonian is given by

$$H_Z = -\gamma\hbar\vec{I}\cdot\vec{B} \qquad (1.1)$$

where γ is the gyromagnetic ratio, $\hbar$ is the reduced Plank's constant, I is the spin moment and B is the external magnetic field. The gyromagnetic ratio, defined as the ratio of a particle's magnetic moment to its angular momentum, represents the strength of interaction between the spin and the magnetic field.

Nuclear spins may occupy $2I + 1$ states, where I represents the spin quantum number. The nuclei must have a non-zero spin quantum number to be NMR-active. For I =½, $2I + 1 = 2$ states occur:

$$E_{\frac{1}{2}} = \frac{-\gamma\hbar B_0}{2} \tag{1.2}$$

$$E_{-\frac{1}{2}} = \frac{+\gamma\hbar B_0}{2} \tag{1.3}$$

Under the Zeeman interaction, the energy difference between these states is proportional to the strength of the external magnetic field. Therefore, the energy difference is

$$\Delta E = \gamma\hbar B_0 = \hbar\omega_0 \tag{1.4}$$

where ω_0 is called the Larmor frequency.

The polarization, or the population difference between the two energy states, is determined by the Boltzmann distribution and is given by

$$P = \frac{e^{\frac{-E_{1/2}}{k_B T}} - e^{\frac{-E_{-1/2}}{k_B T}}}{e^{\frac{-E_{1/2}}{k_B T}} + e^{\frac{-E_{-1/2}}{k_B T}}} \tag{1.5}$$

By substituting in equation 1.2 and 1.3, equation 1.5 can be written as

$$P = \frac{e^{\frac{\gamma\hbar B_0}{2k_B T}} - e^{\frac{-\gamma\hbar B_0}{2k_B T}}}{e^{\frac{\gamma\hbar B_0}{2k_B T}} + e^{\frac{-\gamma\hbar B_0}{2k_B T}}} \tag{1.6}$$

Note that equation 1.6 is a hyperbolic tangent function and can be simplified as

$$P = \tanh\left(\frac{\gamma\hbar B_0}{2k_B T}\right) \tag{1.7}$$

Equation 1.7 indicates that increasing the magnetic field B_0 or decreasing the temperature T can improve the polarization P, and thus the sensitivity in NMR[1–3]. Choosing nuclei with higher gyromagnetic ratio γ is also an effective method to improve the polarization.

1.1.2 Bulk Magnetization

When the magnetic field is zero, the nuclear spin states degenerate and thus there is no net polarization. Another way to look at this is that the nuclear magnetic moments in the sample are oriented randomly, leading to zero net magnetization. When the sample is placed in a magnetic field, the nuclear magnetic moments tend to align along the magnetic field, resulting in a net bulk magnetization oriented in the direction of the external magnetic field.

Suppose that a magnetic field, B_0, points along the z axis and the bulk magnetization vector is tipped away from the z axis. The magnetization vector precesses about B_0 at a the Larmor frequency ω_0 (in rad/s), given by

$$\omega_0 = -\gamma B_0 \tag{1.8}$$

The frequency can also be represented in Hz, as given by

$$\nu_0 = -\frac{1}{2\pi}\gamma B_0 \tag{1.9}$$

1.1.3 NMR Detection

The precession of the magnetization vector is what we detect in NMR spectroscopy. In order to detect the precession, a radiofrequency (RF) coil is placed around the sample. The RF coil can detect the electromotive force induced due to the change of the magnetization vector on the transverse plane, and the detected signal is called the free-induction decay (FID). Manipulating nuclear spins in the sample and detecting the FID enables the study of molecular structure and dynamics. To manipulate the magnetization in the sample, a RF magnetic field must be applied which is resonant with the Larmor frequency of the nucleus. This condition is called being on resonance, and is critical to the NMR experiment.

1.1.4 A Simple NMR Experiment

Figure 1.1 A displays a simple NMR pulse sequence with a 90° on-resonance RF pulse. When the RF pulse (~kV) is applied, the magnetization vector is rotated into the transverse plane. After the pulse (~μs), an electromotive force (~μV) is induced in the coil due to the precession of the magnetization vector in the transverse plane. The induced current, which can be amplified and recorded, is the time-domain NMR signal (**Figure 1.1 B**). Fourier transforming the time-domain FID provides an NMR spectrum in the frequency domain (**Figure 1.1 C**).

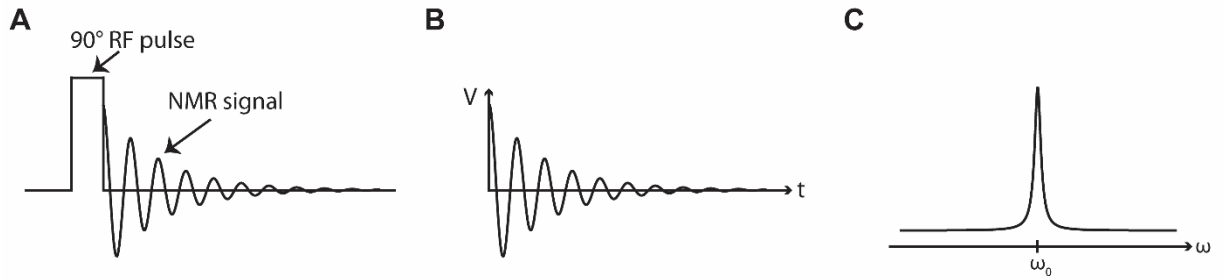

Figure 1.1. A simple NMR experiment. (A) A 90° RF pulse. (B) Time-domain NMR signal. (C) Frequency-domain NMR spectrum. V: voltage; t: time; ω: frequency; ω_0: Larmor frequency.

1.1.5 The Probe

An NMR probe contains an RF coil that can generate pulses to manipulate nuclear spins and detect FID signals. The RF coil can be part of a tuned circuit containing the coil and tuning and matching capacitors (**Figure 1.2**). In the tuned circuit, the resonance effect occurs when the inductive reactance ($\omega_0 L$) and the capacitive reactance $\left(\frac{1}{\omega_0 C}\right)$ are equal in magnitude. The relation between the resonant frequency ω_0, the inductance L, and the capacitance C, and of the circuit is given by,

$$\omega_0 = \frac{1}{\sqrt{LC}} \qquad (1.10)$$

The RF coil can be tuned to the Larmor frequency by the tuning capacitor. The characteristic impedance of the probe and the source impedance can be matched by the matching capacitor to maximize the power transferred.

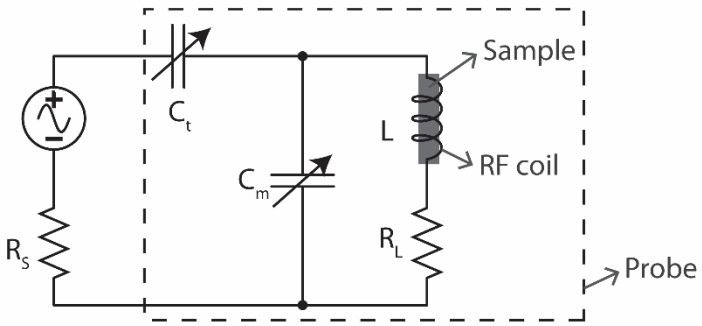

Figure 1.2. Schematic of the key parts of the probe. L: inductance; C_t: tuning capacitance; C_m: matching capacitors; R_L: load resistance; R_S: source resistance.

1.1.6 Magic Angle Spinning (MAS)

In solution-state NMR, anisotropic interactions are averaged to zero due to fast molecular tumbling, leading to narrow resonances in solution-state spectra. However, in solid-state NMR, anisotropic interactions are present and result in broad resonances. Several of these anisotropic interactions in the NMR Hamiltonian, such as dipolar coupling and chemical shift anisotropy, contain an orientation-dependent term ($3\cos^2\theta$-1) that is zero when $\theta = 54.7°$. If a solid sample is rotated about an axis inclined at 54.7° with respect to the external magnetic field, these interactions containing this orientation-dependent term can be averaged to zero, leading to narrow resonances and improved spectral resolution[4]. This technique is known as magic angle spinning (MAS)[5,6].

Cylindrical rotors are typically used for MAS[7–10] (**Figure 1.3 A**). To spin the cylindrical rotors, the bearing gas is required to suspend the rotor body and reduce friction, while the drive gas provides the propulsion and maintains the angular momentum on the turbine insert of the rotor (**Figure 1.3 B**). A spinning frequency of 3 kHz can average chemical shift anisotropy and weak dipolar couplings. Smaller rotors enable higher spinning frequencies, resulting in higher spectral resolution; for instance, spinning frequencies >100 kHz significantly average homonuclear proton interactions[11–18]. Access to higher spinning frequencies is still ongoing because the current

technology is not able to average strong dipolar interactions and hyperfine interactions, which can be 1-10 MHz.

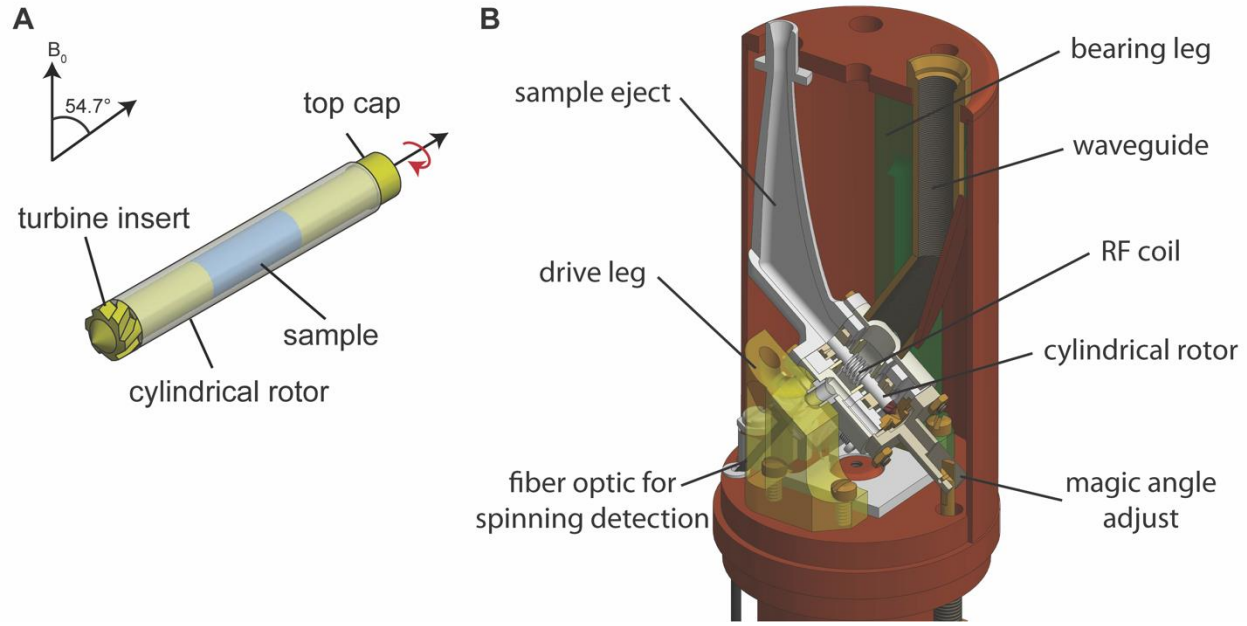

Figure 1.3 Cylindrical rotor conventionally used for MAS. (A) 3.2 mm outer diameter (OD) cylindrical rotor. (B) Probe head for 3.2 mm OD cylindrical rotors. The bearing gas is used to reduce friction and the drive gas provides the propulsion for spinning.

1.2 Dynamic nuclear polarization (DNP)

Characterizing the structure of low-concentration biological samples, such as membrane proteins and endogenous heterogeneous membranes, requires excellent sensitivity in NMR. Dynamic nuclear polarization (DNP) can enhance NMR sensitivity by transferring the polarization from high-γ electron radicals to low-γ nuclei of interest by irradiation of microwaves at specific matching conditions (Equation 1.7)[1,2,19–22]. The theoretical gain of proton polarization from electron spins is 657 times. The DNP enhancement is determined by NMR signal intensity with the microwaves on divided by NMR signal intensity with the microwaves off.

During DNP experiments, polarization is transferred from electron radicals to nuclei of interest using microwaves. Typically, samples are doped with exogenous stable radicals, known as

polarizing agents. Continuous-wave DNP mechanisms include the solid effect and the cross effect are commonly observed at an external magnetic field of 7 T.

1.2.1 Solid Effect

The solid effect mechanism involves one nucleus and one unpaired electron. Narrow-line radicals are typically used for the solid effect as polarizing agents. The solid effect occurs when the microwave frequency matches the electron Larmor frequency ($\omega_{0,e}$) plus or minus the nuclear Larmor frequency ($\omega_{0,n}$)[23,24]. For positive-γ nuclei such as ^{1}H and ^{13}C, maximum positive DNP enhancement can be observed at the matching condition $\omega_{0,e}$-$\omega_{0,n}$, while maximum negative DNP enhancement occurs at the matching condition $\omega_{0,e}$+$\omega_{0,n}$. The solid effect is not as efficient at high magnetic fields because its DNP enhancements scale inversely with B_0^2.[23]

1.2.2 Cross Effect

Different from the solid effect, the cross effect DNP enhancements are inversely related to B_0. The cross effect requires one nucleus and two unpaired electrons, where the two electron resonant frequencies are separated by the nuclear Larmor frequency. Therefore, broad-line radicals such as nitroxide are commonly used as polarizing agents. The DNP enhancement typically depends on the sample but a maximum enhancement of 300 can be achieved through the cross effect mechanism[25–27].

1.3 MAS DNP NMR Instrumentation

MAS DNP requires specialized instrumentation including a microwave source, a cryogenic MAS DNP NMR probe, and cryogenic gas supply. Microwave irradiation is required to transfer the polarization from electron spins to nuclear spins. The polarization is transferred more efficiently at cryogenic temperatures due to the extension of electron relaxation times. Continuous-wave DNP mechanisms such as the solid effect and the cross effect do not perform as well at room temperature

and high magnetic fields[28–34]. A promising route to DNP at room temperature is time-domain DNP with subsequent pulsed electron decoupling[35]. Time-domain DNP can be performed with a custom MAS DNP NMR spectrometer, including a frequency-agile gyrotron (**Figure 1.4**).

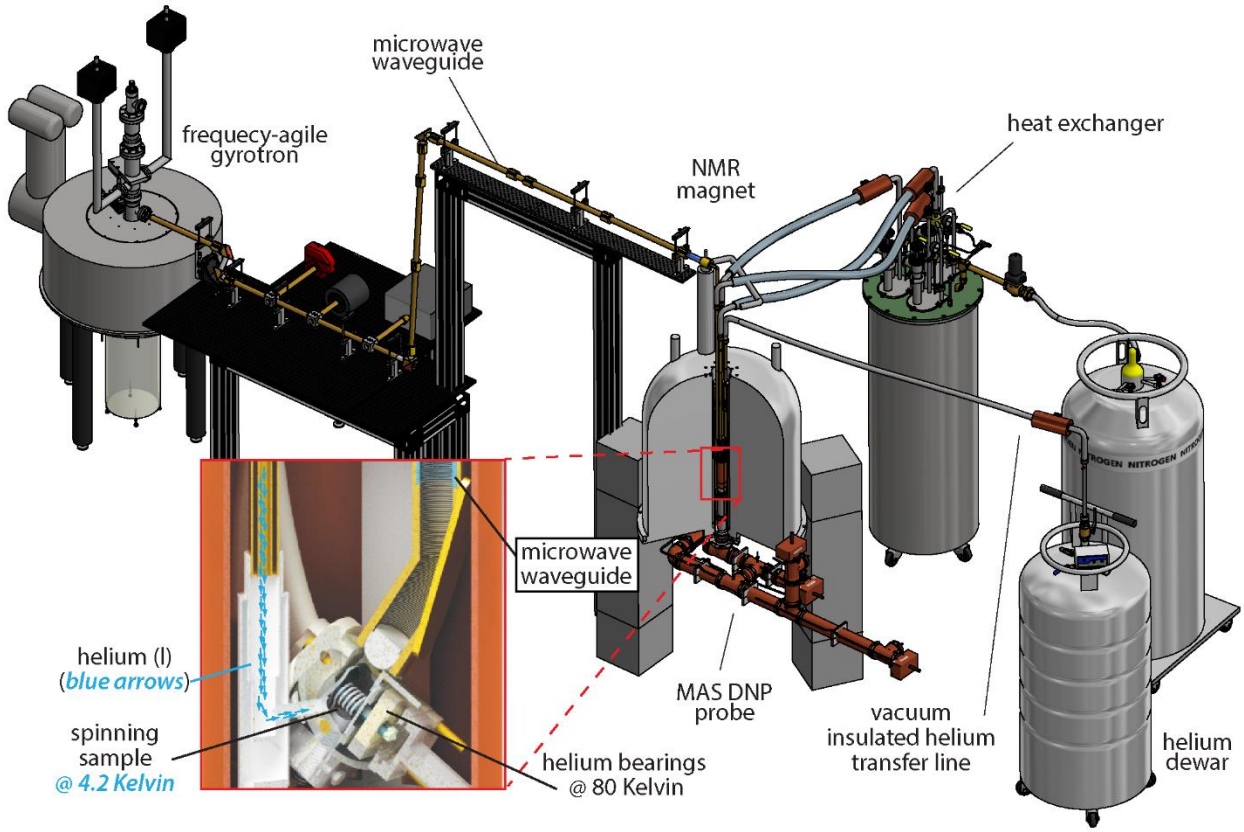

Figure 1.4 Schematic of the helium-cooled DNP spectrometer. The frequency-agile gyrotron (top left) can generate 198 GHz microwaves for DNP. The microwaves are coupled to waveguides and transmitted to the NMR probe. A helium dewar (bottom right) and transfer lines deliver helium to the probe for sample cooling to 4.2 K. A liquid nitrogen heat exchanger cools the helium drive and bearing gas to 90 K.

The 198 GHz microwaves are generated by a custom-built, frequency-agile gyrotron[36], coupled to an overmoded corrugated waveguide, and then transmitted into the DNP-NMR probe within a 7 T superconducting magnet. Gyrotrons can produce chirped pulses for time-domain DNP and electron decoupling. The current gyrotron operates at 198 GHz, contains an output power of 110 W, and can sweep over a bandwidth of 670 MHz. The DNP-NMR probe is a custom-built transmission-line probe[10,37] and can investigate ^{1}H, ^{13}C, ^{15}N, and ^{31}P. The DNP experiments are usually

performed at 90 K where liquid nitrogen is delivered to the probe by a heat exchanger and a transfer line system. The nitrogen drive and bearing gas for spinning the rotor is cooled to 90 K by a liquid nitrogen heat exchanger[27]. In order to cool the sample below 6 K, 90 K helium gas is used for drive and bearing and 4.2 K liquid helium mist is sprayed on the rotor [38].

1.4 Aims and Scope

Chapter 2 introduces the first MAS spheres for solid-state NMR. In contrast to conventional cylindrical rotors, spherical rotors require only one single gas stream to spin stably. This geometry allows implementation of a simplified vertical sample exchange and better access to microwave illumination for cryogenic MAS DNP.

Chapter 3 provides perspectives about microwave coupling with dielectric lenses for cylindrical and spherical MAS rotors. By solving the Maxwell equations with a commercial simulation package, the propagation and focusing of millimeter waves (198 GHz) are determined and the electron Rabi frequency, ν_{1s}, is calculated. Several strategies are discussed to increase the ν_{1s} to better control the electron spins.

Chapter 4 presents sub-millimeter spherical rotors and stators fabricated by three-dimensional direct laser writing (3D-DLW) in order to develop ultra-fast MAS spheres for advanced DNP NMR instrumentation. Novel microstructures on an adaptor are fabricated by ultraviolent (UV) lithography to bridge the gap between the sub-millimeter stators and supra-centimeter NMR probes.

Chapter 5 introduces a strategy to decrease measurement noise by separating the NMR receiving and transmitting circuits and installing a pre-amplifier in close proximity to the receive coil. A

printed circuit board (PCB) is designed to install the receiving circuit in the MAS DNP NMR probe head.

Chapter 6 concludes and summarizes this research. Several future directions are proposed to improve the MAS DNP NMR instrumentation.

1.5 References

1. Barnes, A. B. *et al.* High-field dynamic nuclear polarization for solid and solution biological NMR. *Appl. Magn. Reson.* **34**, 237–263 (2008).
2. Maly, T. *et al.* Dynamic nuclear polarization at high magnetic fields. *J. Chem. Phys.* **052211**, (2008).
3. Thurber, K. & Tycko, R. Low-temperature dynamic nuclear polarization with helium-cooled samples and nitrogen-driven magic-angle spinning. *J. Magn. Reson.* **264**, 99–106 (2016).
4. Stejskal, E. O., Schaefer, J. & Waugh, J. S. Magic-angle spinning and polarization transfer in proton-enhanced NMR. *J. Magn. Reson.* **28**, 105–112 (1977).
5. Lowe, I. J. Free induction decays of rotating solids. *Phys. Rev. Lett.* **2**, 285–287 (1959).
6. Andrew, E. R., Bradbury, A. & Eades, R. G. Nuclear Magnetic Resonance Spectra from a Crystal Rotated at High Speed. *Nature* **182**, 1659 (1958).
7. Eckman, R., Alla, M. & Pines, A. Deuterium NMR in solids with a cylindrical magic angle sample spinner. *J. Magn. Reson.* **41**, 440–446 (1980).
8. Lee, J. N. *et al.* Cylindrical spinner and speed controller for magic angle spinning nuclear magnetic resonance. *Rev. Sci. Instrum.* **55**, 516–520 (1984).
9. Barnes, A. B. *et al.* Cryogenic sample exchange NMR probe for magic angle spinning dynamic nuclear polarization. *J. Magn. Reson.* **198**, 261–270 (2009).
10. Scott, F. J. *et al.* A Versatile Custom Cryostat for Dynamic Nuclear Polarization Supports Multiple Cryogenic Magic Angle Spinning Transmission Line Probes. *J. Magn. Reson.* **297**, 23–32 (2018).
11. Chevelkov, V. *et al.* H-1 detection in MAS solid-state NMR Spectroscopy of biomacromolecules employing pulsed field gradients for residual solvent suppression. *J. Am. Chem. Soc.* **125**, 7788–7789 (2003).
12. Zhou, D. H., Graesser, D. T., Franks, W. T. & Rienstra, C. M. Sensitivity and resolution in proton solid-state NMR at intermediate deuteration levels: Quantitative linewidth characterization and applications to correlation spectroscopy. *J. Magn. Reson.* **178**, 297–

307 (2006).

13. Wickramasinghe, N. P. & Ishii, Y. Sensitivity enhancement, assignment, and distance measurement in C-13 solid-state NMR spectroscopy for paramagnetic systems under fast magic angle spinning. *J. Magn. Reson.* **181**, 233–243 (2006).

14. Wickramasinghe, A. *et al.* Evolution of CPMAS under fast magic-angle-spinning at 100 kHz and beyond. *Solid State Nucl. Magn. Reson.* **72**, 9–16 (2015).

15. Andreas, L. B. *et al.* Structure of fully protonated proteins by proton-detected magic-angle spinning NMR. *Proc. Natl. Acad. Sci. U. S. A.* **113**, 9187–92 (2016).

16. Zhang, R., Mroue, K. H. & Ramamoorthy, A. Proton-Based Ultrafast Magic Angle Spinning Solid-State NMR Spectroscopy. *Acc. Chem. Res.* **50**, 1105–1113 (2017).

17. Xue, K. *et al.* Magic-Angle Spinning Frequencies beyond 300 kHz Are Necessary to Yield Maximum Sensitivity in Selectively Methyl Protonated Protein Samples in Solid-State NMR. *J. Phys. Chem. C* **122**, 16437–16442 (2018).

18. Penzel, S. *et al.* Spinning faster: protein NMR at MAS frequencies up to 126 kHz. *J. Biomol. NMR* **73**, 19–29 (2019).

19. Ni, Q. Z. *et al.* High frequency dynamic nuclear polarization. *Acc. Chem. Res.* **46**, 1933–1941 (2013).

20. Rossini, A. J., Zagdoun, A., Lelli, M., Lesage, A. & Cop, C. Dynamic Nuclear Polarization Surface Enhanced NMR Spectroscopy. *Acc. Chem. Res.* **46**, (2013).

21. Tycko, R. NMR at Low and Ultralow Temperatures. *Acc. Chem. Res.* **46**, 1923–1932 (2013).

22. Can, T. V., Ni, Q. Z. & Griffin, R. G. Mechanisms of dynamic nuclear polarization in insulating solids. *J. Magn. Reson.* **253**, 23–35 (2015).

23. Corzilius, B. *et al.* Solid effect in magic angle spinning dynamic nuclear polarization Solid effect in magic angle spinning dynamic nuclear polarization. **137**, (2012).

24. Smith, A. A., Corzilius, B., Barnes, A. B., Maly, T. & Griffin, R. G. Solid effect dynamic nuclear polarization and polarization pathways. *J. Chem. Phys.* **136**, (2012).

25. Matsuki, Y. *et al.* Dynamic nuclear polarization with a rigid biradical. *Angew. Chemie - Int. Ed.* **48**, 4996–5000 (2009).

26. Zagdoun, A. *et al.* Large molecular weight nitroxide biradicals providing efficient dynamic nuclear polarization at temperatures up to 200 K. *J. Am. Chem. Soc.* **135**, 12790–12797 (2013).

27. Albert, B. J. *et al.* Instrumentation for cryogenic magic angle spinning dynamic nuclear polarization using 90 L of liquid nitrogen per day. *J. Magn. Reson.* **283**, 71–78 (2017).

28. Becerra, L. R., Gerfen, G. J., Temkin, R. J., Singel, D. J. & Griffin, R. G. Dynamic

nuclear polarization with a cyclotron resonance maser at 5 T. *Phys. Rev. Lett.* **71**, 3561–3564 (1993).

29. Lelli, M. *et al.* Solid-State Dynamic Nuclear Polarization at 9.4 and 18.8 T from 100 K to Room Temperature. *J. Am. Chem. Soc.* **137**, 14558–14561 (2015).

30. Akbey, Ü. *et al.* Dynamic nuclear polarization of deuterated proteins. *Angew. Chemie - Int. Ed.* **49**, 7803–7806 (2010).

31. Sauvøe, C. *et al.* Highly Efficient , Water-Soluble Polarizing Agents for Dynamic Nuclear Polarization at High Frequency. *Angew. Chemie Int. Ed.* **52**, 10858–10861 (2013).

32. Afeworki, M., McKay, R. A. & Schaefer, J. Dynamic nuclear polarization enhanced nuclear magnetic resonance of polymer-blend interfaces. *Mater. Sci. Eng. A* **162**, 221–228 (1993).

33. Afeworki, M., Schaefer, J. & Vega, S. Direct Electron-to-Carbon Polarization Transfer in Homogeneously Doped Polycarbonates. *Macromolecules* **25**, 4100–4105 (1992).

34. Afeworki, M. & Schaefer, J. Mechanism of DNP-Enhanced Polarization Transfer across the Interface of Polycarbonate/Polystyrene Heterogeneous Blends. *Macromolecules* **25**, 4092–4096 (1992).

35. Saliba, E. P. *et al.* Electron Decoupling with Dynamic Nuclear Polarization in Rotating Solids. *J. Am. Chem. Soc.* **139**, 6310–6313 (2017).

36. Scott, F. J. *et al.* Frequency-agile gyrotron for electron decoupling and pulsed dynamic nuclear polarization. *J. Magn. Reson.* **289**, 45–54 (2018).

37. Schaefer, J. & McKay, R. A. Multi-Tuned Single Coil Transmission Line Probe for Nuclear Magnetic Resonance Spectrometer. *United States Pat.* (1999). doi:10.1016/0375-6505(85)90011-2

38. Sesti, E. L. *et al.* Magic angle spinning NMR below 6 K with a computational fluid dynamics analysis of fluid flow and temperature gradients. *J. Magn. Reson.* **286**, 1–9 (2018).

Chapter 2: Magic Angle Spinning Spheres

In solution-state NMR, molecular tumbling can average anisotropic interactions, leading to narrow resonances in the spectra; however, solid-state NMR lacks this advantage, so broad resonances are usually observed. Magic angle spinning (MAS) is employed in solid-state NMR to partially average anisotropic interactions, improving sensitivity and spectral resolution. To perform MAS on cylindrical rotors, the bearing gas is utilized to suspend the rotor, while the drive gas provides the propulsion. A variable temperature line is also generally used to regulate sample temperature. This chapter introduces spherical rotors that exhibit several advantages over cylindrical rotors. Spherical rotors require only a single gas stream that serves as drive, bearing, and variable temperature. Simplified geometry provides easier reinsertion of samples via a vertical sample ejection line. Spheres will also improve dynamic nuclear polarization (DNP) techniques by allowing for better coupling of microwaves to the sample. Fast and stable MAS spheres can significantly improve NMR spectral resolution for biological research. This chapter is adapted from "Magic Angle Spinning Spheres" published in *Science Advances*, volume 4, article eaau1540, September 2018, by Pinhui Chen, Brice J. Albert, Chukun Gao, Nicholas Alaniva, Lauren E. Price, Faith J. Scott, Edward P. Saliba, Erika L. Sesti, Patrick T. Judge, Edward W. Fisher, Alexander B. Barnes. DOI: 10.1126/sciadv.aau1540 under Creative Commons Attribution 4.0 International License (https://creativecommons.org/licenses/by/4.0/).

Abstract

Magic angle spinning (MAS) is commonly used in nuclear magnetic resonance (NMR) of solids to improve spectral resolution. Rather than employing cylindrical rotors for MAS, we demonstrate that spherical rotors can be spun stably at the magic angle. Spherical rotors conserve valuable space in the probe head and simplify sample exchange and microwave coupling for dynamic

nuclear polarization (DNP). In this current implementation of spherical rotors, a single gas stream provides bearing gas to reduce friction, drive propulsion to generate and maintain angular momentum, and variable temperature control for thermostating. Grooves are machined directly into zirconia spheres, thereby converting the rotor body into a robust turbine with high torque. We demonstrate that 9.5 mm outside diameter spherical rotors can be spun at frequencies up to 4.6 kHz with N_2 (g) and 10.6 kHz with He (g). Angular stability of the spinning axis is demonstrated by observation of ^{79}Br rotational echoes out to 10 ms from KBr packed within spherical rotors. Spinning frequency stability of ±1 Hz is achieved with resistive heating feedback control. A sample size of 36 μL can be accommodated in 9.5 mm diameter spheres with a cylindrical hole machined along the spinning axis. We further show that spheres can be more extensively hollowed-out to accommodate 161 μL of sample, which provides superior signal-to-noise compared to traditional 3.2 mm diameter cylindrical rotors.

2.1 Introduction

Magic angle spinning (MAS) nuclear magnetic resonance (NMR) experiments partially average anisotropic spin interactions in the magnetic resonance Hamiltonian through mechanical rotation of samples about the magic angle (54.7^o with respect to the static magnetic field, B_0). The spatial averaging extends spin relaxation times and improves the resolution of solid-state NMR spectroscopy[1,2]. Single resonances can often be assigned to chemically distinct nuclear spins to yield site-specific signatures encoding structural information and molecular dynamics[3–7]. MAS-NMR is, therefore, a powerful technique to characterize diverse molecular architectures including membrane proteins[8–15], amyloid fibrils[16–19], bacterial biofilms[20,21], and also materials and surfaces[22–25].

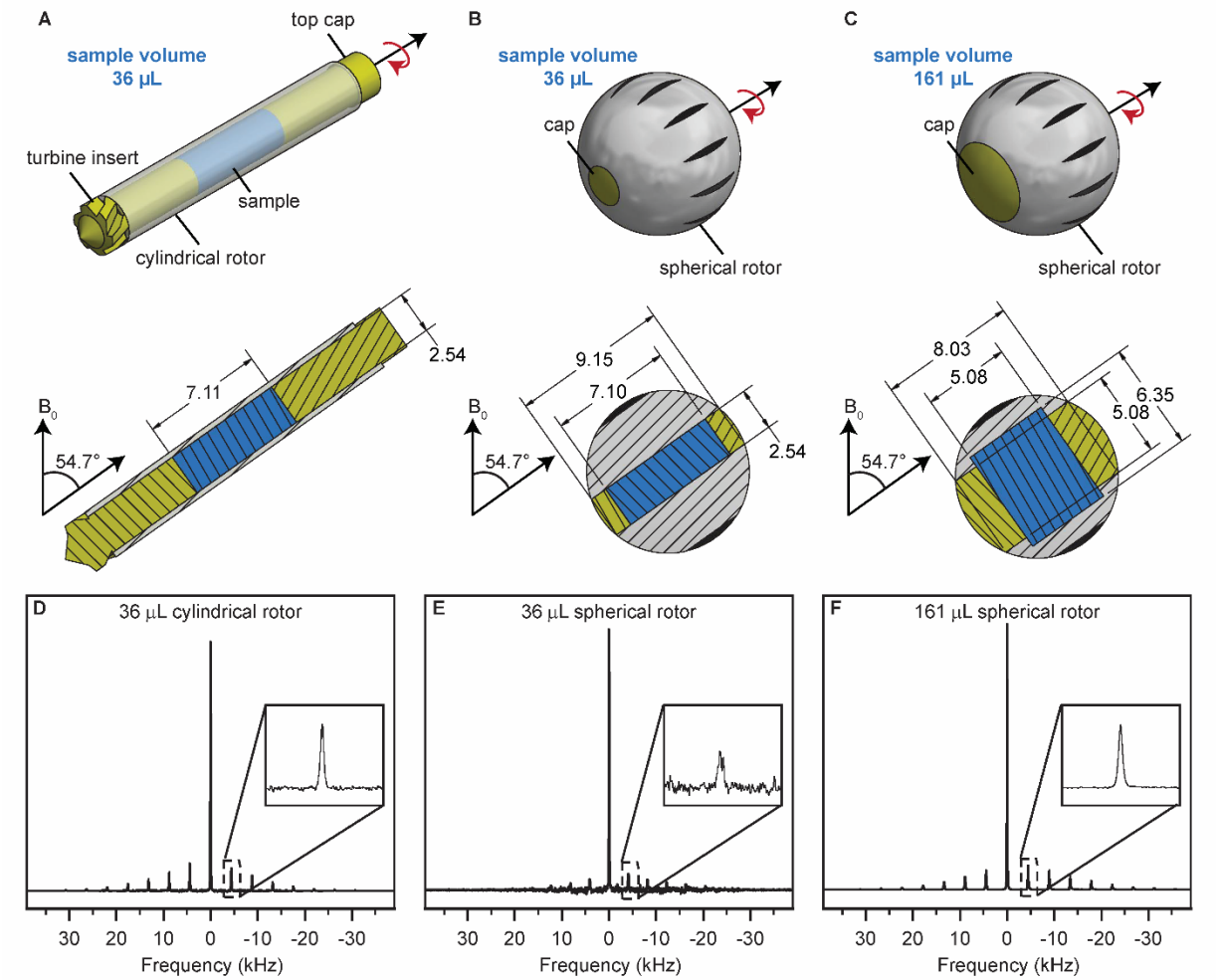

Figure 2.1 Rotors for MAS NMR. (A) 3.2 mm cylindrical rotor with 36 µL sample volume. 9.5 mm spherical rotors include equatorial turbine grooves cut into the surface to generate angular momentum. Two sample chambers have been machined, (B) 36 µL and (C) 161 µL. All linear dimensions are in millimeters. The first-order sidebands in ^{79}Br spectra of KBr were used to analyze NMR sensitivity of (D) 3.2 mm cylindrical rotors, (E) 36 µL spherical rotors, and F) 161 µL spherical rotors. Each spectrum is an average of 256 transients.

Mechanical sample rotation must be comparable to, or greater than, the frequency of the internal anisotropic spin interaction to produce significant averaging. Spinning frequencies less than 3 kHz averaged chemical shift anisotropy and weak dipole couplings at the advent of MAS. Currently available spinning frequencies of > 150 kHz are sufficiently high to attenuate proton homonuclear couplings and yield spectra of solids with resolution approaching that observed in solution-state NMR[26–29]. Over the past 60 years of MAS, samples have typically been packed into hollow cylindrical sample containers (rotors), with turbine inserts to supply drive propulsion (**Figure 2.1 A**).

The long, narrow cylindrical shape of these rotors and the necessity for them to rotate at the magic angle complicates the sample exchange process. Sample exchanges for cylindrical rotors mandate an angle adjustment of either the rotor or the stator for insertion or ejection within the magnet bore. This alignment typically requires considerable space within the magnet[30]. Furthermore, cylindrical rotors for cryogenic MAS dynamic nuclear polarization (DNP) experiments, aimed at improving NMR signal-to-noise, present significant challenges to microwave coupling into the sample.[31–33]

We sought to improve MAS instrumentation in order to simplify sample exchange, improve DNP, reduce cryogen usage, and access spinning frequencies > 150 kHz[34]. Macroscopic metallic spherical rotors have been spun up to 667 kHz employing electromagnetic bearings and drive energy[35]. Although such technology cannot be directly translated into MAS within superconducting magnets, the fact that macroscopic spheres can be spun effectively is important and exploitable. We therefore turned to spherical rotors for MAS.

Spherical rotors have distinct advantages over cylindrical rotors. Wobbling about the long axis of cylindrical rotors results in bearing collisions that can destroy the sample and stator. The isotropic spherical rotor alleviates these issues, since wobbling about an axis other than the primary spinning axis does not result in stator collisions. Furthermore, our implementation of a spherical rotor enables a simplified vertical sample exchange, while providing better access for microwave illumination. Here we introduce spheres for MAS, demonstrating MAS-NMR spectroscopy of samples packed within spherical rotors spinning stably at the magic angle.

2.2 Materials and Methods

Commercial sources of relatively low-cost, high-precision spheres are available as industrial lubricants and ball bearings. We machined 36 μL or 161 μL sample chambers into yttria-stabilized

zirconia (ZrO_2) solid spheres with a diameter of 9.525 mm (**Figure 2.1 B-C**). Twelve turbine grooves were cut into the spherical rotor longitudinally (O'Keefe Ceramics, Woodland Park, CO). Kel-F spacers and epoxy were used to seal the sample chambers (**Figure 2.1 B-C**). Stators to house the spherical rotors were 3D printed from an acrylonitrile-butadiene-styrene material (Form2 SLA printer, Clear V4 Resin, Formlabs, Somerville, MA).

All experiments were performed at a B_0 = 7.05 T corresponding to a ^{79}Br Larmor frequency of 75.214 MHz. Spectra were recorded with a custom-built 2-channel, transmission line probe resonating a split solenoid sample coil. A Bloch decay with a pulse length of 20 μs was employed for spherical rotors, with a 1 s recycle delay. Spinning frequencies were measured on a testing apparatus outside the magnet with a LT-880 laser tachometer (Terahertz Technologies Inc., Oriskany, NY) as mentioned in section **2.2.2**. Spinning frequencies during the NMR experiments were measured with fiber optics and a MAS control unit (TecMag, TX).

2.2.1 Rapid Prototyping by 3D Printing

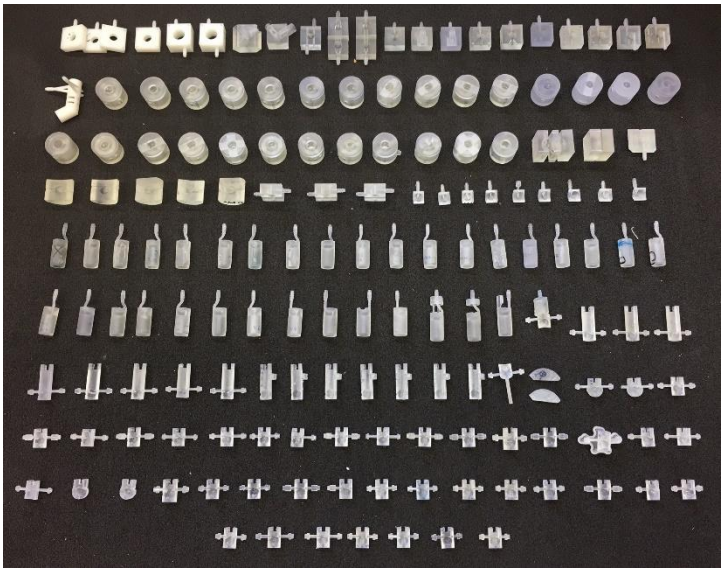

Figure 2.2 3D-printed stators for spherical rotors. Shown above is a selection of the 232 different stators that were designed, printed, and evaluated experimentally for optimal spinning at the magic angle.

Stators that house the spherical rotors and provide fluid dynamics suitable for high-frequency stable magic angle spinning (MAS) were 3D printed (Form2 SLA printer, Formlabs, Somerville, MA). 3D printing permitted rapid prototyping and greatly accelerated this initial design phase. 232 stators were designed, fabricated, and tested as shown in **Figure 2.2** which displays various stages of our designs. The goal of this rapid prototyping was to design a stator that provides stable MAS, spinning frequency detection, and sample ejection for spherical rotors.

2.2.2 Magic Angle Spinning Test Station for 3D-Printed Stators

Spherical rotor frequencies were detected with a LT-880 laser tachometer (Terahertz Technologies Inc., Oriskany, NY) which was connected to an oscilloscope (Tektronix MDO3034). To improve spinning stability regulation, four marks were placed on the spherical rotor instead of one (**Figure 2.3 A**). A 12 Ω nichrome wire was installed on the gas inlet to heat the gas for spinning regulation[1] (**Figure 2.3 B-C**).

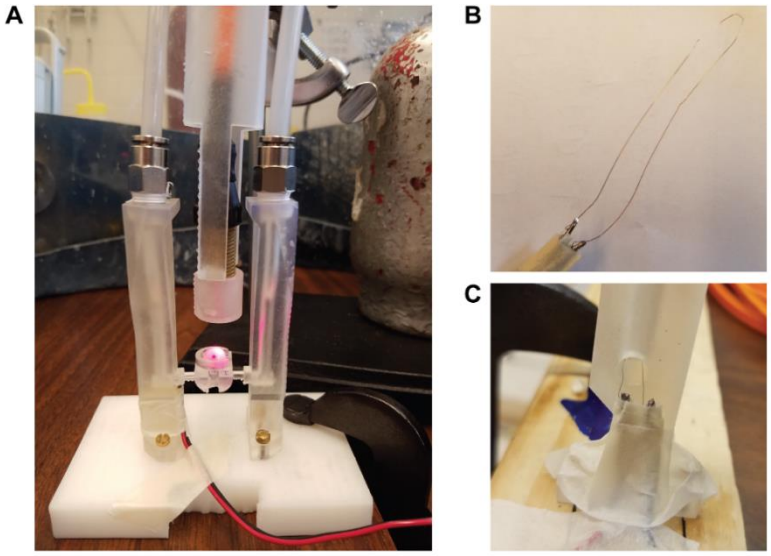

Figure 2.3 Spinning test station for spherical rotors in 3D-printed stators. **(**A) Spinning test station. The spherical rotor and the stator were connected to the stator legs where the gas was introduced. The sensor head of the LT-880 laser tachometer was installed from the top to detect the spinning frequency. (B) Nichrome wire for heating of the gas for spinning regulation. (C) The nichrome wire was installed on the gas inlet.

2.3 Results and Discussion

2.3.1 Spherical Rotor Design

The spherical rotors contain cylindrical sample chambers and equatorial turbine grooves cut into the surface of the rotor. A large moment of inertia and improved spinning stability is achieved by ensuring the mass distribution of high-density zirconia is distant from the spinning axis. The 36 μL sample chamber in spherical rotors matches the 3.2 mm cylindrical rotor (**Figure 2.1 A-B**), and we further hollowed out the 9.5 mm peripheral diameter rotors to accommodate 161 μL of sample (**Figure 2.1 C**).

Converting the zirconia rotor body into a turbine, rather than relying on turbine inserts, delivers a robust drive platform with high torque. The combination of cylindrical sample chambers and grooves establishes a preferred axis of rotation about a single axis (**Figure 2.1 B-C**). This allows the spherical rotor to be inserted at arbitrary orientations within the stator. When spinning gas is applied, the sphere quickly samples different orientations until rotation about the preferred axis is established.

2.3.2 Stator for Spherical Rotor

Prototyping stator geometries with 3D printing greatly accelerated the production of a successful stator design (**Figure 2.2**). We chose to use relatively large dimensions (9.5 mm diameter) to leverage rapid prototyping with resolution readily available for 3D printing. For instance, we have now printed and tested 232 stators to spin spherical rotors. We expect improved spinning performance as the fluid flow is further optimized within precision-fabricated stators.

Figure 2.4 shows a selection of four stator designs that demonstrate progression to the current implementation. Initially, the stator was enclosed and multiple gas streams (**Figure 2.4 A**), comparable to bearings and drive cups within cylindrical MAS stators, were employed. However,

these designs lead to spinning instability due to poor fluid flow dynamics. Simplification of the design to a single gas stream resulted in spinning about a single axis. Spinning stability with the single-stream stator was greatly improved by adding a pathway to guide the exhausting gas (**Figure 2.4 B**). Positioning the gas inlet aperture within the hemispherical stator at the complement to the magic angle resulted in stable MAS (**Figure 2.4 C**). Additionally, **Figure 2.4 D** shows a vertical extrusion of 2 mm that improves fluid flow, resulting in faster spinning. Blind holes for fiber optics pass sufficient light to enable spinning frequency detection without impacting fluid flow (**Figure 2.4 D**).

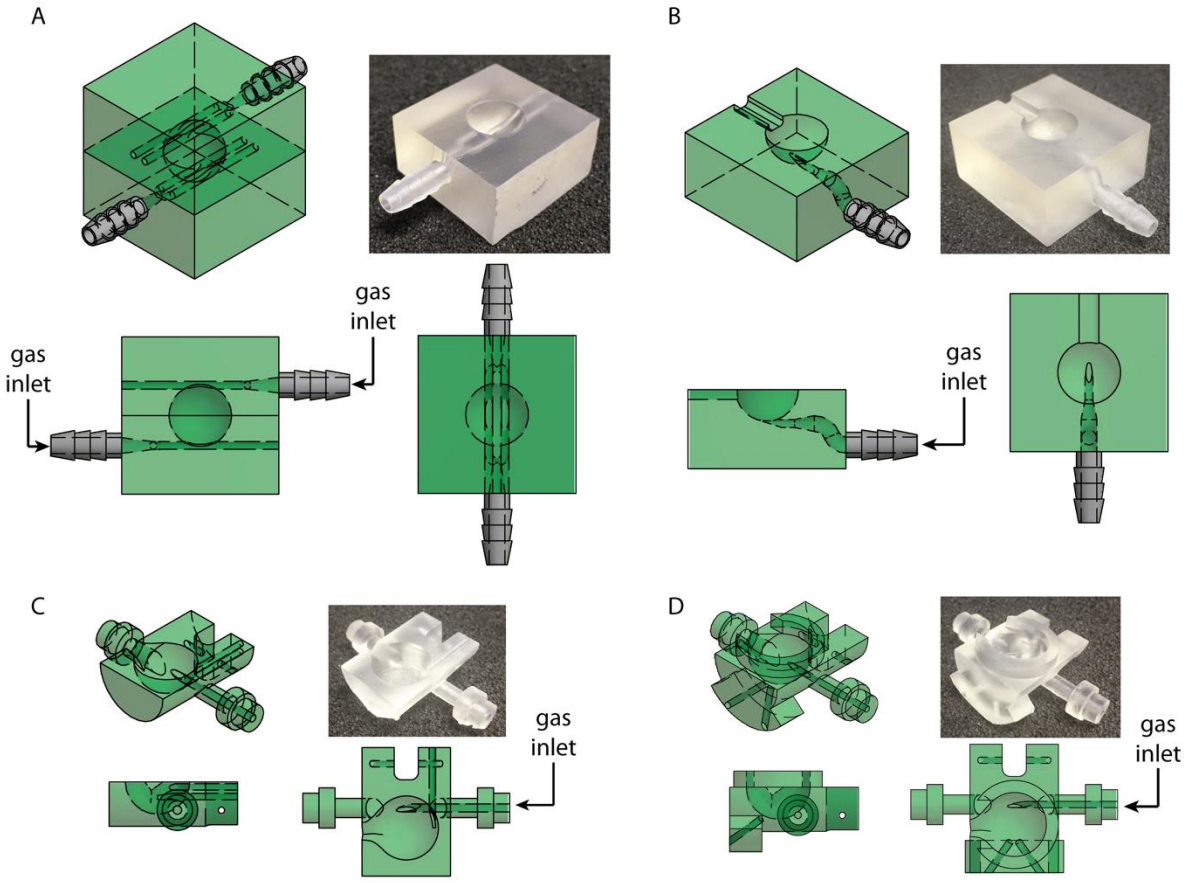

Figure 2.4 A selection of the four 3D-printed stators for spherical rotors. (A) Enclosed design with multiple gas streams for spinning. (B) Open-face design with a single gas stream and a pathway to guide exhaust gas. (C) Design complete with single gas stream, exhaust pathway, and pivots for adjustment of the magic angle. (D) In comparison to (C), a vertical extrusion of 2 mm is added above the cup of the stator and blind holes have been added to accept fiber optics for spinning frequency detection.

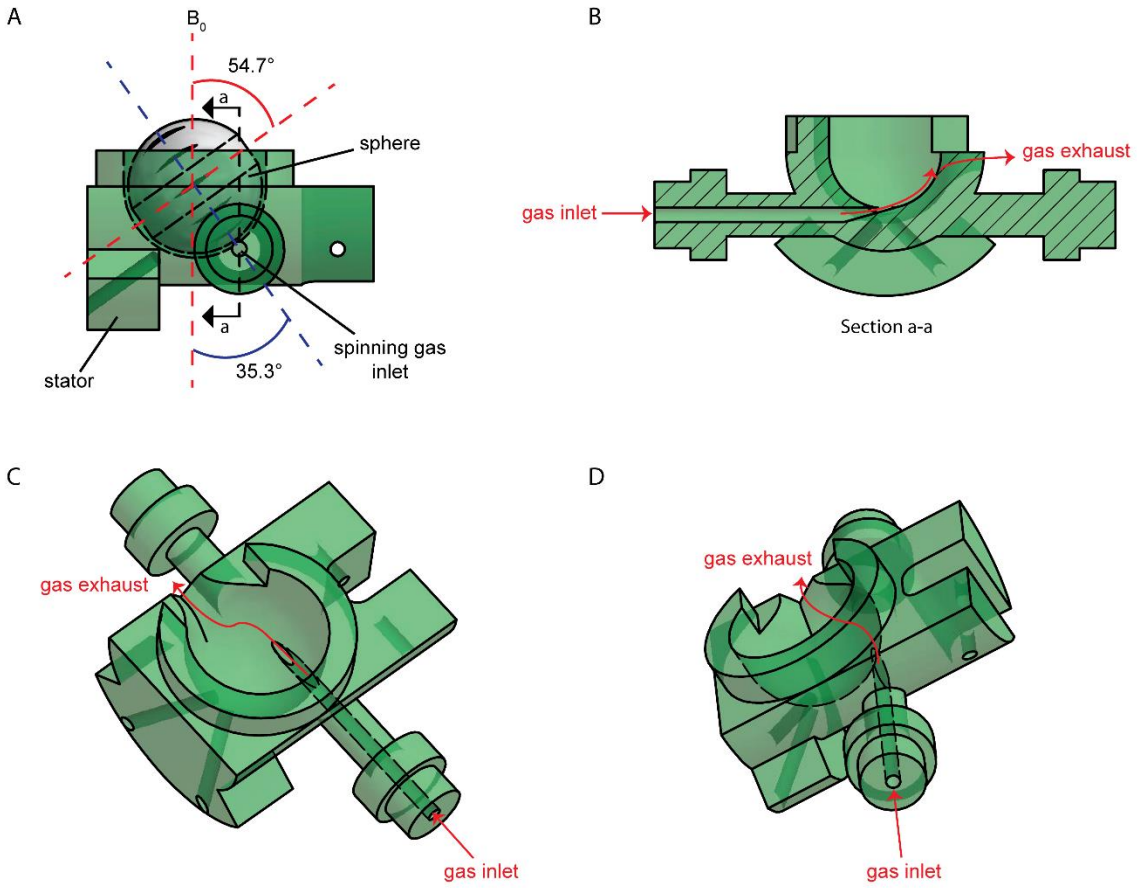

Figure 2.5 Our current stator design with a single gas stream. (A) The gas introduced under the sphere 35.3° off of B_0 suspends the sphere and aligns its spinning axis with the magic angle. (B) A section view from (A), shows the gas inlet path and how the gas is directed into the drive cup by a tangent plane. (C) and (D) show the overall flow path of the spinning gas from two separate isometric views.

Our current stator design (**Figure 2.4 D** and **Figure 2.5**) incorporates only a single gas stream, which simultaneously provides bearing gas to reduce friction, propulsion to generate and maintain angular momentum, and variable temperature control for thermostating. Introducing this gas stream under the sphere 35.3° off of B_0 suspends the sphere and generates rotation of the sample at the magic angle of 54.7° (**Figure 2.5 A**). A plane at the end of the gas inlet, which is tangent to the hemispherical drive cup, guides the spinning gas into the stator (**Figure 2.5 B**). The spinning gas then exits through the exhaust opposite of the gas inlet. The gas inlet and exhaust are designed in a common plane which is perpendicular to the spinning axis of the rotor. **Figure 2.5 C-D** shows the flow path of the spinning gas through the stator.

2.3.3 NMR Probes

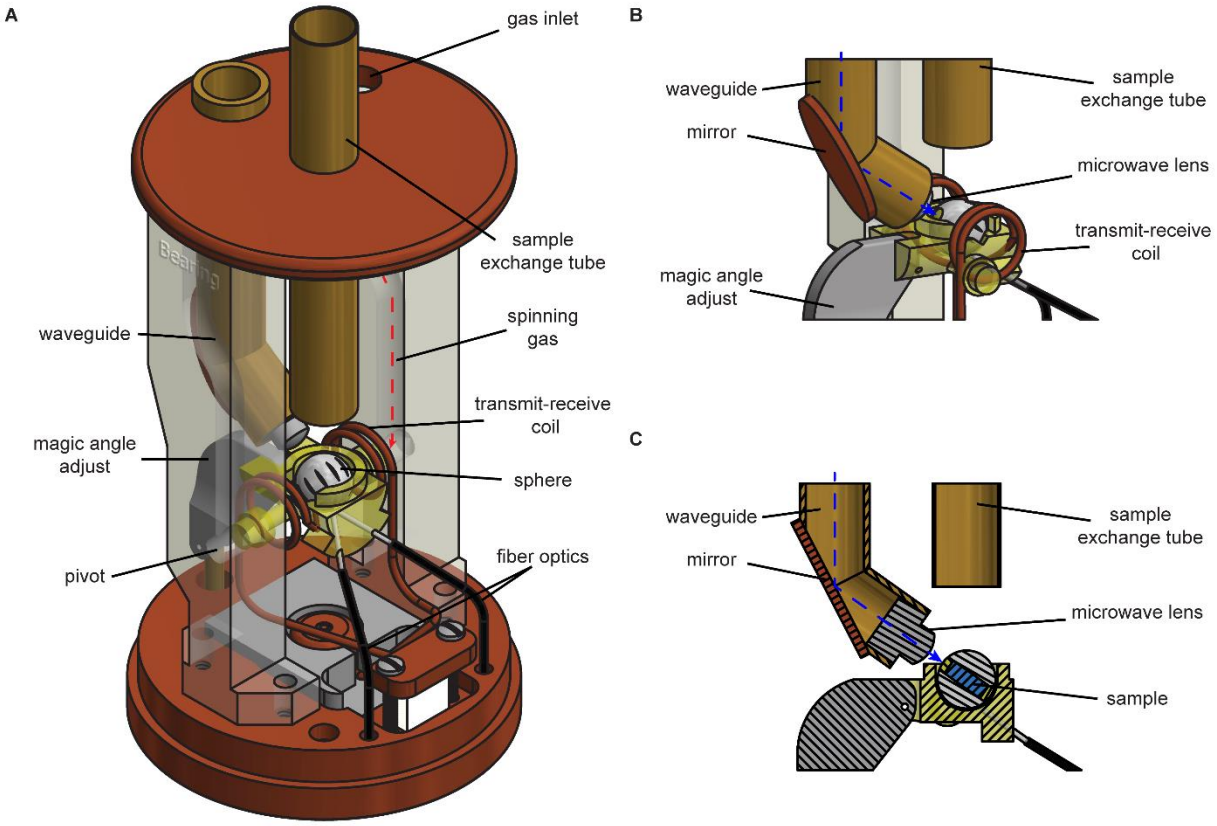

Figure 2.6 Implementation of rotating spheres into a transmission line probe previously employed in cryogenic MAS-DNP. (A) The pivots of the 3D-printed stator serve as the gas inlet and as the pivot point for the magic angle adjustment. The complete NMR probe head includes fiber optics for spinning frequency detection, magic angle adjustment via a threaded adjustment assembly, waveguide to transmit microwaves to the sample for DNP, tube for sample exchange, and a 3D-printed post for connection of the stator to the gas supply. An isometric view (B) and a section view (C) show the path for the introduction of microwaves to the sample for DNP.

The transmit-receive coil is a four-turn split-solenoid wrapped around the stator. This design allows for vertical access to the sample, albeit with decreased NMR sensitivity due to a low filling factor. We designed stators that were compatible with our current NMR probes. The design interfaces to an adjustment apparatus for magic angle optimization and also improves microwave illumination for DNP (**Figure 2.6**). Implementation of spherical rotors simplified sample exchange by allowing vertical access to the sample. This eliminated the need for rotation of either the rotor or the stator prior to sample exchange, as is necessary for cylindrical rotors[30]. The sample exchange now mimics systems typically used in solution NMR instrumentation. A simple tube connected to

a wet/dry vacuum (model 3VE20, Dayton Electric Mfg. Co., Lake Forest, IL) was used to extract and insert the sphere. With minor adjustments, this new compact MAS NMR stator and rotor design could be implemented in a wide variety of NMR probes for both narrow and wide bore magnets.

2.3.4 Results with KBr

^{79}Br yields quadrupolar spinning sidebands that are used to optimize the magic angle[36]. Rotational echoes were observed at 10 ms in the time domain (**Figure 2.7 A**). The Fourier transform of the signal showed sidebands separated by the spinning frequency of 4297 Hz (**Figure 2.7 B**). The central resonance had a width of 123 Hz at half height, while the first sideband had a width of 143 Hz at half height, indicating spinning closely matching to 54.7° off the B_0 magnetic field. **Figure 2.7 C** shows peak height ratios of the center band and 2nd sidebands versus deviation from the magic angle, similar to the description by Frye and Maciel[36]. The relative height of the center band compared to the sidebands decreases as the angle of rotation approaches the magic angle. **Figure 2.7 C** clearly indicates the ability to optimize the magic angle in MAS NMR experiments. **Figure 2.7 D-E** shows the regulated and unregulated spinning frequency over 22 minutes. Regulation of spinning frequency utilized a 12 Ω nichrome wire heating element to regulate the gas temperature (**Figure 2.3**)[37]. **Figure 2.7 F** indicates that 98% of the frequencies measured fall within 4560±1 Hz. This frequency regulation system which improves spinning stability in the spheres has yet to be implemented with NMR signal detection.

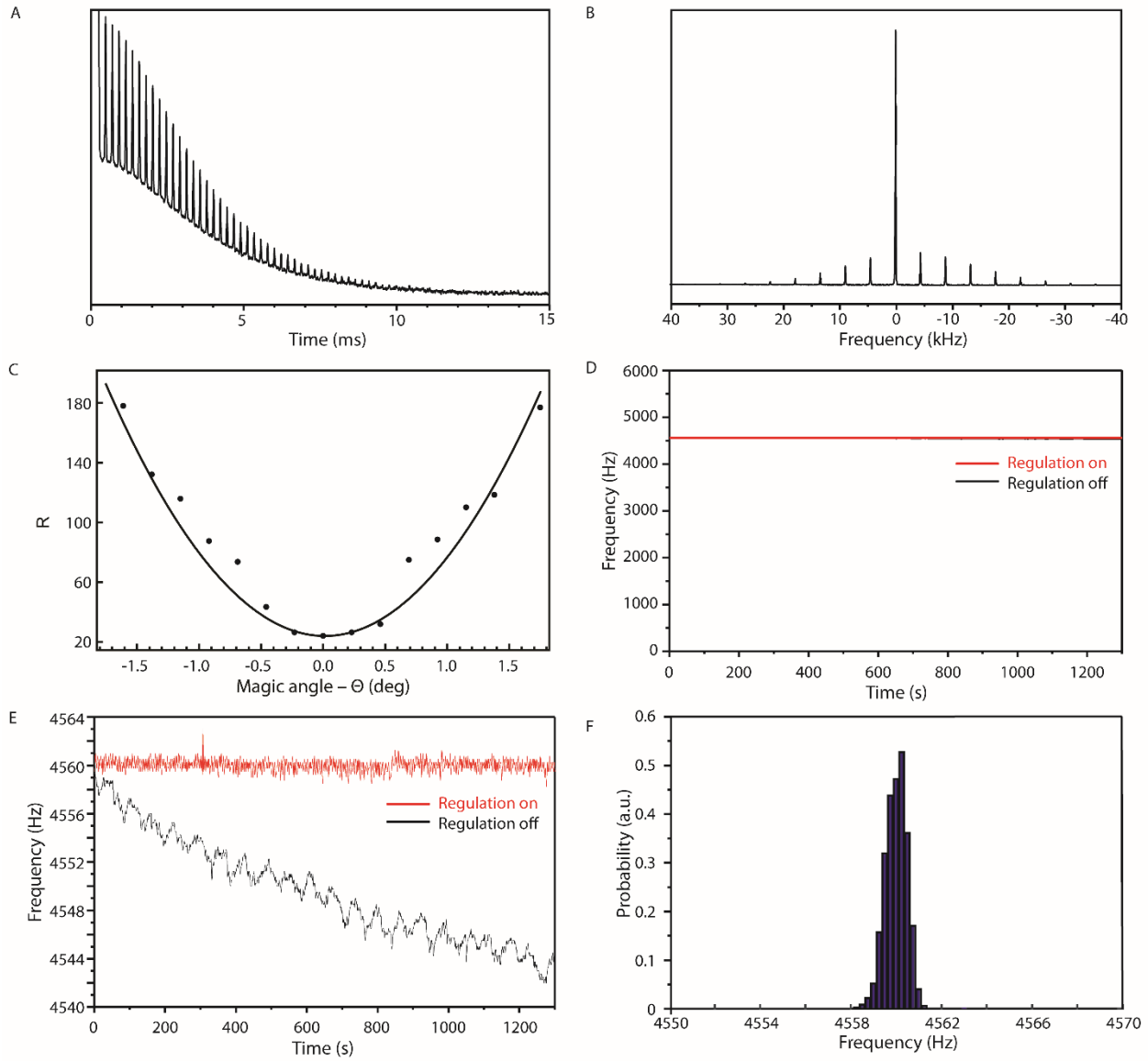

Figure 2.7 Magic angle adjustment and spinning stability regulation of MAS with spherical rotors. ^{79}Br magnetic resonance of magic angle spinning spheres packed with KBr. (A) Free induction decay (FID) of 64 transients with rotational echoes observed out to 10 ms. (B) Spinning sidebands in the frequency domain indicate spinning of 4.3 kHz stably at the magic angle. (C) Optimization of the magic angle at a spinning frequency of 2.5 kHz. The height ratio (R) of the center band peak relative to the 2nd sideband decreases as the angle of rotation approaches 54.7^{o} from B_0.[36] (D) Spinning frequency stability over 22 minutes with and without spinning regulation controlled through a resistive heating element circuit. (E) Expansion of spinning frequency shows moderate excursion in spinning frequency of less than 20 Hz without regulation, and improved frequency stability with regulation. (F) Histogram of spinning frequencies showing the rotor spinning at 4560±1 Hz for 98% of the 22 minutes observed.

The first-order sidebands in ^{79}Br spectra of KBr were used to compare NMR sensitivity of three MAS rotor geometries: a 3.2 mm cylindrical rotor, a 36 μL spherical rotor, and a 161 μL spherical rotor (**Figure 2.1 D-F**). Each spectrum is an average of 256 transients. Though the filling factor of

the spherical rotors in a split-solenoid coil is not ideal, the 161 µL spherical rotor yields better signal-to-noise ratios than the 3.2 mm cylindrical rotor.

We also investigated mechanical advantages imparted by the spherical shape of the rotors through further increasing centrifugal forces from spinning. Helium gas at high pressure resulted in > 10 kHz spinning of the 9.5 mm diameter spherical rotors. Rotors within the stator design shown in **Figure 2.4 D** and **Figure 2.5** were spun to 10.6 kHz using 11 bar He (g) on a testing apparatus outside the magnet (**Figure 2.8**). The sphere maintained spinning stability above 10 kHz, similar to that demonstrated in **Figure 2.7 D**. This observation provides promise that with further optimization of fluid flow and scaling to smaller sizes, spinning frequencies of > 150 kHz can be achieved.

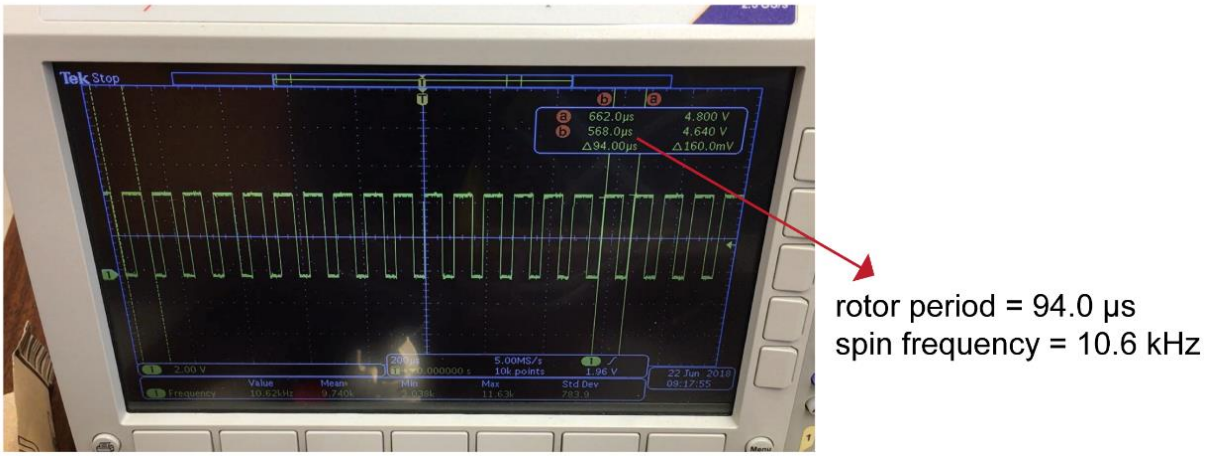

Figure 2.8 Spherical rotor spun at 10.6 kHz with helium gas.

2.3.5 Spinning Frequency Reproducibility

In order to ensure spinning frequency reproducibility, multiple spherical rotors and multiple copies of the stator were tested. Four different spherical rotors were tested with the same stator, as shown in **Table 2.1**. The spinning stability of less than 5 Hz for rotors tested demonstrates that spinning frequency and spinning stability did not depend on packing inconsistency to a substantial extent.

Eleven different copies of the same stator were tested with one spherical rotor (**Table 2.2**). The spinning stability for ten of the eleven stator copies is less than 2 Hz, indicating excellent reproducibility of the 3D printed design.

Table 2.1 Spinning test with same stator and different spherical rotors.

	Pressure (psi)	Frequency (Hz)
Spherical rotor #1	85	5508 ± 2
Spherical rotor #2	90	5478 ± 3
Spherical rotor #3	90	5446 ± 1
Spherical rotor #4	90	5540 ± 5

Table 2.2 Spinning test with same spherical rotor and different stator copies.

	Pressure (psi)	Frequency (Hz)
Stator copy #1	85	5508 ± 2
Stator copy #2	90	5628 ± 2
Stator copy #3	90	5290 ± 2
Stator copy #4	90	5189 ± 1
Stator copy #5	90	5541 ± 1
Stator copy #6	90	5414 ± 5
Stator copy #7	90	5444 ± 1
Stator copy #8	90	5245 ± 2
Stator copy #9	90	5476 ± 1
Stator copy #10	90	5473 ± 1
Stator copy #11	90	5493 ± 1

2.3.6 Correlation Between Temperature and Spinning Frequency

The correlation between temperature and the spinning frequency was recorded as the spherical rotor was spun up to 5.5 kHz and back down to a stop using air (**Figure 2.9**). The temperatures were recorded using an infrared (IR) thermometer (Fluke 62 MAX IR Thermometer) at about 6 in. away from the object to be measured. The temperature of the table with the spinning test station was measured as the ambient temperature to ensure that temperature fluctuations within the room did not affect the temperature of the spherical rotor. The fluctuation of the temperature was below 0.7 °C, indicating little dependence of temperature on MAS frequencies. A slight temperature

decrease at the rotor was observed when the spinning frequency went up. We attribute this cooling to the increased cooling capacity of air at higher flow rate. At frequencies <10 kHz, the heat transferred from kinetic energy friction of the air molecules at the rotor surface does not seem to be enough to induce heating.

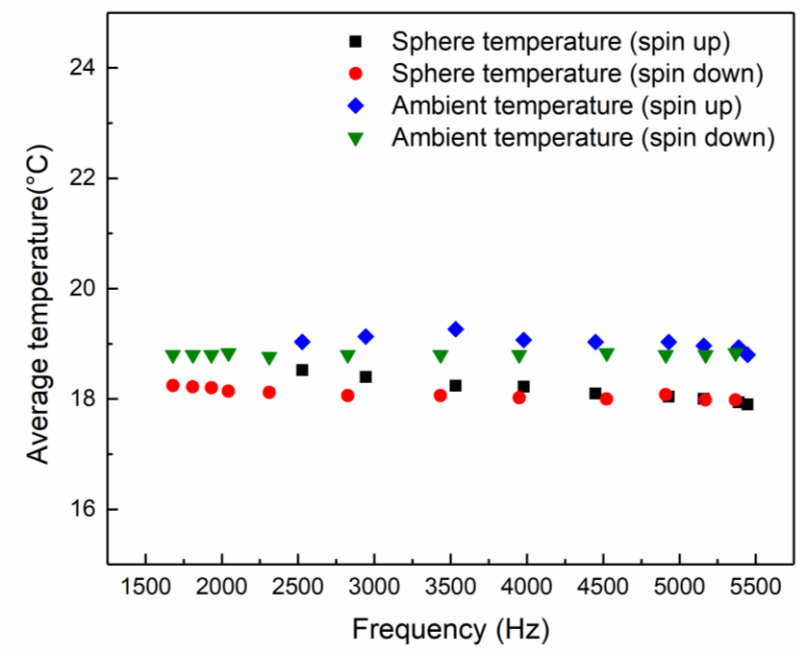

Figure 2.9 Correlation between temperature and spinning frequency of spherical rotor.

2.4 Conclusions and Outlook

MAS spheres have been demonstrated with practical advantages over their cylindrical counterparts. Future implementation of spherical rotors is expected to lead to higher spinning frequencies through the optimization of turbine and stator geometry. With the relatively straightforward design of the current spherical rotors and supporting stators, the implementation of MAS spheres described here should scale well to micron-sized rotors. Access to small rotors will better enable MAS at frequencies > 150 kHz[34], and we are currently designing spheres ≤ 2 mm for MAS DNP.

The single aperture in stators used to spin spherical rotors could facilitate adoption of cryogenic MAS DNP into narrow-bore magnets. Currently, vacuum-jacketed transfer lines are required to

provide separate bearing, drive, and variable temperature (VT) gases. MAS spheres, as demonstrated herein, only require a single gas stream, decreasing the space required within high-field superconducting magnet bores.

NMR sensitivity of samples packed within spherical rotors will be improved through modifications of the transmit-receive coil and stators. For instance, coil geometries such as saddle coils will yield better filling factors and are still amenable to simplified vertical sample exchange. Such inductors will also permit more efficient microwave coupling to the sample for MAS DNP experiments, while maintaining sample exchange ability.

Finally, spherical rotors for magnetic resonance could also have widespread application in switched angle spinning (SAS)[38–40] and double angle rotation (DOR)[41,42]. For instance, introducing a second gas inlet into the stator to establish spinning off of the magic angle. Spherical rotors are expected to play a prominent role in the future development of MAS NMR.

2.5 References

1. Lowe, I. J. Free induction decays of rotating solids. *Phys. Rev. Lett.* **2**, 285–287 (1959).
2. Andrew, E. R., Bradbury, A. & Eades, R. G. Nuclear Magnetic Resonance Spectra from a Crystal Rotated at High Speed. *Nature* **182**, 1659 (1958).
3. Tuttle, M. D. *et al.* Solid-state NMR structure of a pathogenic fibril of full-length human α-synuclein. *Nat. Struct. Mol. Biol.* **23**, 1–9 (2016).
4. Kaplan, M. *et al.* EGFR Dynamics Change during Activation in Native Membranes as Revealed by NMR. *Cell* **167**, 1241-1251.e11 (2016).
5. Castellani, F. *et al.* Structure of a protein determined by solid-state magic-angle-spinning NMR spectroscopy. *Nature* **420**, 98–102 (2002).
6. Zech, S. G., Wand, A. J. & McDermott, A. E. Protein Structure Determination by High-Resolution Solid-State NMR Spectroscopy: Application to Microcrystalline Ubiquitin. *J. Am. Chem. Soc.* **127**, 8618–8626 (2005).
7. Caulkins, B. G. *et al.* NMR Crystallography of a Carbanionic Intermediate in Tryptophan Synthase: Chemical Structure, Tautomerization, and Reaction Specificity. *J. Am. Chem.*

Soc. **138**, 15214–15226 (2016).

8. Retel, J. S. *et al.* Structure of outer membrane protein G in lipid bilayers. *Nat. Commun.* **8**, 1–10 (2017).

9. Eddy, M. T. *et al.* Magic angle spinning nuclear magnetic resonance characterization of voltage-dependent anion channel gating in two-dimensional lipid crystalline bilayers. *Biochemistry* **54**, 994–1005 (2015).

10. Ni, Q. Z. *et al.* Primary Transfer Step in the Light-Driven Ion Pump Bacteriorhodopsin: An Irreversible U-Turn Revealed by Dynamic Nuclear Polarization-Enhanced Magic Angle Spinning NMR. *J. Am. Chem. Soc.* **140**, 4085–4091 (2018).

11. McDermott, A. Structure and Dynamics of Membrane Proteins by Magic Angle Spinning Solid-State NMR. *Annu. Rev. Biophys.* **38**, 385–403 (2009).

12. Yang, H. *et al.* REDOR NMR reveals multiple conformers for a protein kinase c ligand in a membrane environment. *ACS Cent. Sci.* **4**, 89–96 (2018).

13. Baker, L. A. *et al.* Combined 1 H-Detected Solid-State NMR Spectroscopy and Electron Cryotomography to Study Membrane Proteins across Resolutions in Native Environments. 161–170 (2018). doi:10.1016/j.str.2017.11.011

14. Renault, M. *et al.* Solid-state NMR spectroscopy on cellular preparations enhanced by dynamic nuclear polarization. *Angew. Chemie - Int. Ed.* **51**, 2998–3001 (2012).

15. Kaplan, M. *et al.* Probing a cell-embedded megadalton protein complex by DNP-supported solid-state NMR. *Nat. Methods* **12**, 649–652 (2015).

16. Siemer, A. B., Ritter, C., Ernst, M., Riek, R. & Meier, B. H. High-Resolution Solid-State NMR Spectroscopy of the Prion Protein HET-s in Its Amyloid Conformation. *Angew. Chem. Int. Ed.* **44**, 2–5 (2005).

17. Hoop, C. L. *et al.* Huntingtin exon 1 fibrils feature an interdigitated β-hairpin–based polyglutamine core. *Proc. Natl. Acad. Sci.* **113**, 1546–1551 (2016).

18. Theint, T. *et al.* Species-dependent structural polymorphism of Y145Stop prion protein amyloid revealed by solid-state NMR spectroscopy. *Nat. Commun.* **8**, (2017).

19. Petkova, a. T. *et al.* Self-propagating, molecular-level polymorphism in Alzheimer's beta-amyloid fibrils. *Science (80-.).* **307**, 262–265 (2005).

20. McCrate, O. A., Zhou, X., Reichhardt, C. & Cegelski, L. Sum of the parts: Composition and architecture of the bacterial extracellular matrix. *J. Mol. Biol.* **425**, 4286–4294 (2013).

21. Thongsomboon, W. *et al.* Phosphoethanolamine cellulose: A naturally produced chemically modified cellulose. *Science* **359**, 334–338 (2018).

22. Bertmer, M., Nieuwendaal, R. C., Barnes, A. B. & Hayes, S. E. Solid-state photodimerization kinetics of alpha-trans-cinnamic acid to alpha-truxillic acid studied via solid-state NMR. *J. Phys. Chem. B* **110**, 6270–6273 (2006).

23. Rossini, A. J. *et al.* Dynamic Nuclear Polarization Enhanced Solid-State NMR Spectroscopy of Functionalized Metal-Organic Frameworks. *Angew. Chemie* **124**, 127–131 (2012).

24. Wang, Z. *et al.* Quantitative atomic-scale structure characterization of ordered mesoporous carbon materials by solid state NMR. *Carbon N. Y.* **131**, 102–110 (2018).

25. Lesage, A. *et al.* Surface enhanced NMR spectroscopy by dynamic nuclear polarization. *J. Am. Chem. Soc.* **132**, 15459–61 (2010).

26. Andreas, L. B. *et al.* Structure of fully protonated proteins by proton-detected magic-angle spinning NMR. *Proc. Natl. Acad. Sci. U. S. A.* **113**, 9187–92 (2016).

27. Zhou, D. H., Graesser, D. T., Franks, W. T. & Rienstra, C. M. Sensitivity and resolution in proton solid-state NMR at intermediate deuteration levels: Quantitative linewidth characterization and applications to correlation spectroscopy. *J. Magn. Reson.* **178**, 297–307 (2006).

28. Wickramasinghe, N. P. & Ishii, Y. Sensitivity enhancement, assignment, and distance measurement in C-13 solid-state NMR spectroscopy for paramagnetic systems under fast magic angle spinning. *J. Magn. Reson.* **181**, 233–243 (2006).

29. Chevelkov, V. *et al.* H-1 detection in MAS solid-state NMR Spectroscopy of biomacromolecules employing pulsed field gradients for residual solvent suppression. *J. Am. Chem. Soc.* **125**, 7788–7789 (2003).

30. Barnes, A. B. *et al.* Cryogenic sample exchange NMR probe for magic angle spinning dynamic nuclear polarization. *J. Magn. Reson.* **198**, 261–270 (2009).

31. Saliba, E. P. *et al.* Electron Decoupling with Dynamic Nuclear Polarization in Rotating Solids. *J. Am. Chem. Soc.* **139**, 6310–6313 (2017).

32. Hoff, D. E. M. *et al.* Frequency swept microwaves for hyperfine decoupling and time domain dynamic nuclear polarization. *Solid State Nucl. Magn. Reson.* **72**, 79–89 (2015).

33. Can, T. V., Weber, R. T., Walish, J. J., Swager, T. M. & Griffin, R. G. Frequency-Swept Integrated Solid Effect. *Angew. Chemie - Int. Ed.* **56**, 6744–6748 (2017).

34. Xue, K. *et al.* C : Physical Processes in Nanomaterials and Nanostructures Magic Angle Spinning Frequencies Beyond 300 kHz are Necessary to Yield Maximum Sensitivity in Selectively Methyl Protonated Protein Samples in Solid State NMR Magic Angle Spinning Frequencies beyo. (2018). doi:10.1021/acs.jpcc.8b05600

35. Schuck, M., Steinert, D., Nussbaumer, T. & Kolar, J. W. Ultrafast rotation of magnetically levitated macroscopic steel spheres. *Sci. Adv.* **4**, (2018).

36. Frye, J. S. & Maciel, G. E. Setting the magic angle using a quadrupolar nuclide. *J. Magn. Reson.* **48**, 125–131 (1982).

37. Mihaliuk, E. & Gullion, T. Using heat to control the sample spinning speed in MAS

NMR. *J. Magn. Reson.* **212**, 249–253 (2011).

38. Terao, T., Fujii, T., Onodera, T. & Saika, A. Switching-angle sample-spinning nmr spectroscopy for obtaining powder-pattern-resolved 2D spectra: Measurements of 13C chemical-shift anisotropies in powdered 3,4-dimethoxybenzaldehyde. **107**, 145–148 (1984).

39. Kolbert, A. C., Grandinetti, P. J., Baldwin, M. & Prusiner, S. B. Measurement of Internuclear Distances by Switched Angle Spinning. 7936–7938 (1994).

40. Litvak, I. M. *et al.* Pneumatic switched angle spinning NMR probe with capacitively coupled double saddle coil. *J. Magn. Reson.* **206**, 183–189 (2010).

41. Chmelka, B. F. *et al.* Oxygen-17 NMR in solids by dynamic-angle spinning and double rotation. *Nature* **339**, 42–43 (1989).

42. Samoson, A., Lippmaa, E. & Pines, A. High resolution solid-state N.M.R. *Mol. Phys.* **65**, 1013–1018 (1988).

Chapter 3: Perspectives on Microwave Coupling into Cylindrical and Spherical Rotors with Dielectric Lenses for Magic Angle Spinning Dynamic Nuclear Polarization

Dynamic nuclear polarization (DNP) improves NMR sensitivity, allowing for the investigation of complicated biological systems; however, transitioning magic angle spinning (MAS) DNP to the time domain requires intense microwave fields. Dielectric lenses are described in this chapter to effectively couple the microwaves into the sample and improve the electron Rabi frequency, ν_{1s}. This chapter introduces designs from 3.2 mm cylindrical rotors, 9.5 mm cylindrical rotors, 9.5 mm spherical rotors, to 0.5 mm diamond spheres. Approaches to better couple the microwaves include decreasing the sample size, installing a dielectric lens within the rotor to avoid some physical constrains, changing the shape of the rotor to be spherical due to the microwave distribution, and proposing diamond as a promising material for rotors. Effective microwave coupling and higher ν_{1s} can enable time-domain DNP experiments. The improved MAS DNP NMR instrumentation will be beneficial for biomedical research. This chapter is adapted from "Perspectives on Microwave Coupling into Cylindrical and Spherical Rotors with Dielectric Lenses for Magic Angle Spinning Dynamic Nuclear Polarization" published in *Journal of Magnetic Resonance*, article in press, July 2019, by Pin-Hui Chen, Chukun, and Alexander B. Barnes. DOI: https://doi.org/10.1016/j.jmr.2019.07.005.

Abstract

Continuous wave dynamic nuclear polarization (DNP) increases the sensitivity of NMR, yet intense microwave fields are required to transition magic angle spinning (MAS) DNP to the time

domain. Here we describe and analyze Teflon lenses for cylindrical and spherical MAS rotors that focus microwave power and increase the electron Rabi frequency, ν_{1s}. Using a commercial simulation package, we solve the Maxwell equations and determine the propagation and focusing of millimeter waves (198 GHz). We then calculate the microwave intensity in a time-independent fashion to compute the ν_{1s}. With a nominal microwave power input of 5 W, the average ν_{1s} is 0.38 MHz within a 22 μL sample volume in a 3.2 mm outer diameter (OD) cylindrical rotor without a Teflon lens. Decreasing the sample volume to 3 μL and focusing the microwave beam with a Teflon lens increases the ν_{1s} to 1.5 MHz. Microwave polarization and intensity perturbations associated with diffraction through the radiofrequency coil, losses from penetration through the rotor wall, and mechanical limitations of the separation between the lens and sample are significant challenges to improving microwave coupling in MAS DNP instrumentation. To overcome these issues, we introduce a novel focusing strategy using dielectric microwave lenses installed within spinning rotors. One such 9.5 mm OD cylindrical rotor assembly implements a Teflon focusing lens to increase the ν_{1s} to 2.7 MHz within a 2 μL sample. Further, to access high spinning frequencies while also increasing ν_{1s}, we analyze microwave coupling into MAS spheres. For 9.5 mm OD spherical rotors, we compute a ν_{1s} of 0.36 MHz within a sample volume of 161 μL, and 2.5 MHz within a 3 μL sample placed at the focal point of a novel double lens insert. We conclude with an analysis and discussion of sub-millimeter diamond spherical rotors for time domain DNP at spinning frequencies > 100 kHz. Sub-millimeter spherical rotors better overlap a tightly focused microwave beam, resulting in a ν_{1s} of 2.2 MHz. Lastly, we propose that sub-millimeter dielectric spherical microwave resonators will provide a means to substantially improve electron spin control in the future.

3.1 Introduction

Magic angle spinning (MAS) nuclear magnetic resonance (NMR) is a powerful technique to investigate molecular structure [1–8]. However, the low sensitivity of NMR spectroscopy hinders experiments and can lead to long signal averaging times. Dynamic nuclear polarization (DNP) increases MAS-NMR sensitivity by orders of magnitude by transferring polarization from electron to nuclear spins[9–14]. Common continuous-wave (CW) DNP mechanisms include the solid effect, the cross effect, and the Overhauser effect[15]. However, CW-DNP does not perform as well at room temperature and high magnetic fields[16–22], and current limitations in microwave intensity curtail the transition of DNP from CW to pulsed regimes[23].

Time domain DNP with subsequent pulsed electron decoupling is a promising route to DNP at room temperature[24]. The integrated solid effect (ISE)[25–27], nuclear orientation via electron spin locking (NOVEL)[28–30], electron-nuclear cross-polarization (eNCP)[31,32], and time-optimized (TOP) DNP[33] are all promising time domain DNP approaches that can be implemented with readily available frequency-tunable gyrotron oscillators[23,34], and semiconductor microwave switches[35]. However, these time domain DNP experiments require a high electron Rabi frequency, ν_{1s}. For example, using the frequency-swept integrated solid effect, an ν_{1s} of 1.5 MHz yields sufficient electron spin control for time domain DNP[26]. We therefore set out to design and analyze instrumentation to increase the electron Rabi frequency to greater than 1.5 MHz.

Different methods to increase ν_{1s} include high-power microwave sources[36–42], and also improving microwave coupling through the use of microwave resonators[43–45] and dielectric lenses[46,47]. For instance, a cylindrical Teflon lens has been shown to increase ν_{1s} from 0.84 MHz to 0.91 MHz[46].

In addition to achieving intense microwave fields, MAS DNP instrumentation must also provide intense radiofrequency (RF) fields to control and detect nuclear spins, cryogenic cooling of samples to extend spin relaxation, and sample rotation to partially average anisotropic interactions within the spin Hamiltonian[42,48,49]. Therefore, significant challenges associated with increasing the ν_{1s} in MAS DNP experiments by improving microwave coupling to the sample include microwave diffraction through the RF coil, losses from penetration through the rotor wall, and mechanical limitations to the optimal distance between the Teflon lens and sample.

To achieve higher spinning frequencies and better couple the microwaves into the sample, we have developed spherical MAS rotors for DNP-NMR[50]. For example, we have demonstrated 9.5 mm outside diameter (OD) spherical rotors can spin stably up to 10.6 kHz at the magic angle[50]. Performing time domain DNP with electron decoupling in MAS spherical rotors will be a powerful technique to investigate biological and chemical structures[23].

High Frequency Structure Simulator (HFSS; Ansys, Canonsburg, PA), a commercially available simulation package that solves Maxwell equations, determines the propagation and focusing of millimeter waves in a time-independent fashion to compute the ν_{1s} of electron spins[24,46,51]. We employ this microwave analysis strategy to investigate Teflon lenses with different sizes and shapes of rotors to improve ν_{1s}.

3.2 Methods

HFSS requires incident microwave power, dielectric constants (ε), and probe geometry to accurately model microwave coupling to the sample. In our laboratory, 198 GHz microwaves are generated by custom-built gyrotrons[42] and transmitted to DNP-NMR probes[52] with a corrugated

waveguide. The output power of our gyrotrons currently spans from 10 to 40 W, and transmission losses are typically 3 dB, resulting in a consistent minimum power delivery of 5 W to the probe[52].

Here we modeled the microwave input into the stator as a pure Gaussian beam with a waist of 3.175 mm and a power of 5.0 W[51]. The spinning apparatus, waveguide, and radiofrequency coil for each simulation resides inside of an air box, and with exterior interfaces defined as a radiation boundary. In other words, all of the microwave power incident on the surface of the box is transmitted to the surroundings, without any power reflecting back. Meshing of the computation voxels varies depending on the size of the structures in the simulation, with typical meshing density totaling one million voxels.

The sample in the simulations is a cryoprotecting glycerol-water frozen glass. The dielectric constant ($\varepsilon=\varepsilon_r+i\varepsilon_i$) of this matrix at 77 K and 140 GHz is 3.5 (ε_r), with a loss tangent ($\tan\delta=\varepsilon_i/\varepsilon_r$) of 0.005[46]. To model the dielectric constant at 198 GHz, we retained the real part (ε_r = 3.5) and scaled the imaginary part (ε_i = 0.007), because ε_r is expected to be mostly invariant to a frequency change of 58 GHz, and ε_i scales linearly with frequency[53,54].

The pass number, how many times HFSS calculates the same model, is typically between 15 to 25 before the calculation converges and requires approximately one day of computation on a desktop computer. We calculate the electron Rabi frequency ν_{1s} after the calculation converges.

The average ν_{1s} is calculated using the same method as described previously[46,51]. This calculation method includes conversion of laboratory frame from HFSS coordinate and volume average of the peak transverse magnetic field[51]. The following equation is used to calculate ν_{1s}:

$$\nu_{1s} = \frac{1}{2} \times \gamma_s \times \frac{\mu}{V} \int_V \sqrt{|\mathrm{H} \cdot \hat{\mathrm{x}}|^2 + |\mathrm{H} \cdot \hat{y}|^2} dV$$

where γ_s is the gyromagnetic ratio of the electron spins, μ is permeability of free space, V is the sample volume, and H is the magnetic field.

Importantly, all of these simulations have been benchmarked with experimental data previously. For example, Nanni & Barnes et al. determined a ν_{1s} of 0.84 MHz with 5 W of 250 GHz microwave power incident on a 4 mm sapphire rotor[46]. Note, that study included a Teflon lens and metallic coating on the interior of the stator to increase microwave intensity in the sample. That Nanni & Barnes et al. study also verified the value of 0.84 MHz (with 5 W of incident microwave power) using published values of electron relaxation, and a theoretical treatment of cross effect DNP performance involving Bloch equations and electron spin saturation. In a subsequent study[51], we showed that our simulations closely matched the results of Nanni & Barnes et al. for 4 mm sapphire rotors. We also have previously employed a microwave analysis to 3.2 mm cylindrical zirconia rotors[24].

In the present study, the results shown in **Figure 1A** closely match the results of these previous studies, and therefore act as an experimental verification and important benchmark for all other microwave analysis presented herein. We emphasize that the goal of this study is to improve microwave coupling to MAS samples. Even if the absolute magnitude of the electron spin Rabi frequencies is not precise, the relative improvement in microwave performance is the salient aspect of the microwave analysis presented in the following sections.

3.3 Results & Discussion

3.3.1 Cylindrical Rotor with a 3.2 mm OD

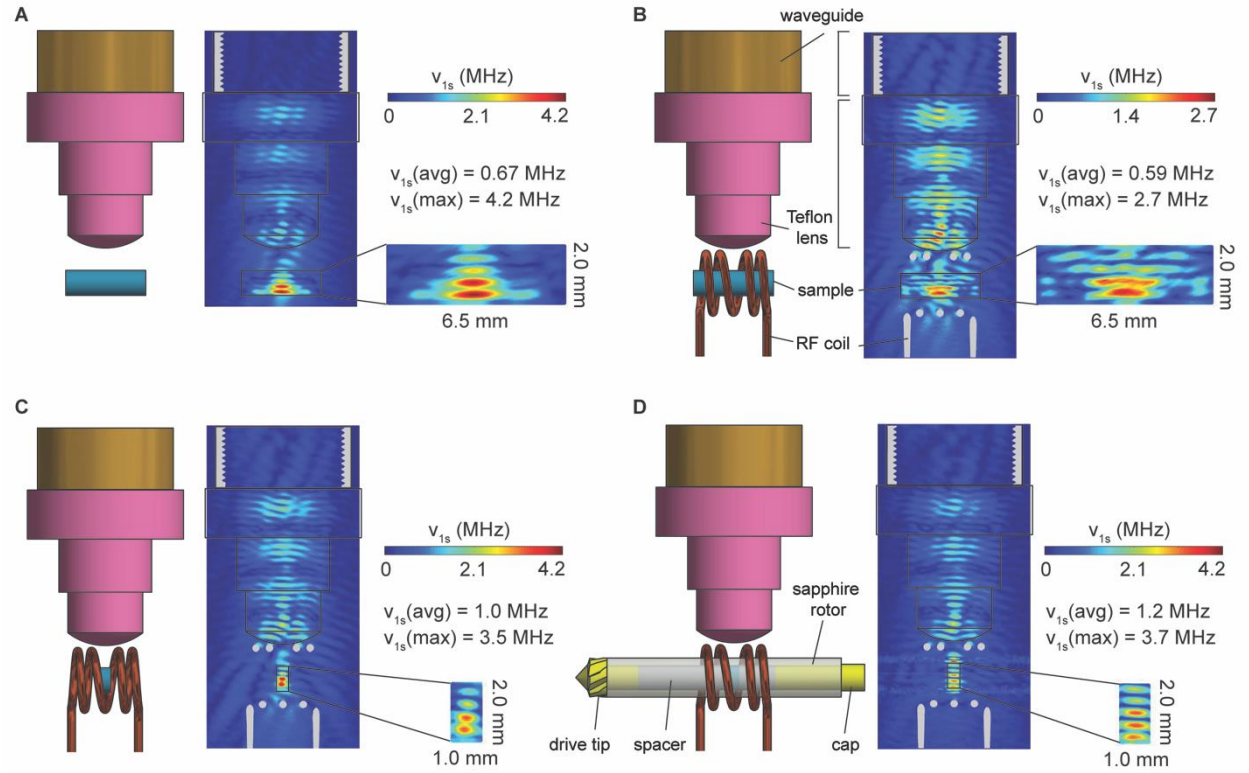

Figure 3.1 HFSS results at 198 GHz with increasing system complexity. (A) Schematics and HFSS of a waveguide, Teflon focusing lens, and cryoprotected sample (~22 μL). (B) Schematics and HFSS with the addition of an RF coil. (C) Schematics and HFSS with a sample size reduction (~3 μL). (D) Schematics and HFSS results with the addition of a sapphire rotor.

Components were included sequentially into the simulation geometry to analyze the effects of the RF coil and rotor on the microwave beam (**Figure 3.1**). **Figure 3.1 A** shows a Teflon lens (ε_r=2.1) focusing the microwave beam into a cylindrical 22 μL sample (ε_r=3.5). This model yields an average ν_{1s} of 0.67 MHz throughout the sample. The Teflon lens is composed of a curvature end with a radius of 5 mm to focus the microwaves[46] and a cylindrical stalk to fit the lens with different geometries (waveguide, stator, 9.5 mm cylindrical or spherical rotors). The focused beam results in high microwave intensity in the middle of the sample and very low power delivery at the ends. The simulation in **Figure 3.1 B** also includes a four-turn spaced RF coil that diffracts and attenuates the microwave beam, resulting in a reduction of the average ν_{1s} to 0.59 MHz. Previously,

it has been calculated that an RF coil of thin wire and a tight pitch will pass microwave power without such losses[46]. However, we have not pursued this strategy because flow dynamics from variable temperature fluid can result in mechanical instability of such weakly supported coils. Such mechanical instability can have detrimental effects on RF performance, especially with high variable temperature fluid streams required for cryogenic MAS experiments below 6 Kelvin[48].

As demonstrated by Zilm and Carroll[55], the ν_{1s} can be increased by focusing the microwave beam into small volume samples. Our microwave analysis (**Figure 3.1 C**) shows an average ν_{1s} of 1.0 MHz throughout a 3 μL sample employing this strategy. Including a cylindrical sapphire rotor results in yet additional microwave focusing into the sample, and a ν_{1s} of 1.2 MHz throughout the 3 μL sample volume (**Figure 3.1 D**).

To examine the ability of the lens to focus microwaves within the context of the complex geometry of the stator, we also performed simulations which include the Kel-F stator body and bearings (**Figure 3.2**). **Figure 3.2** compares the ν_{1s} with and without the Teflon lens. Based on HFSS, the average ν_{1s} is 1.5 MHz with a Teflon lens and a small volume of 3 μL, almost four-times greater than without a Teflon lens (0.38 MHz) over a sample volume of 22 μL. We emphasize that these results compare favorably to a previous microwave analysis which has been confirmed experimentally, providing an important benchmark for our study[46]. Also note that more incident microwave power will increase ν_{1s} accordingly. Gyrotron development to generate intense microwave and frequencies suitable for high-resolution NMR is an active field of research[16,34,38,42,56]. In addition to developing higher power microwave sources (>100 kW) to perform time domain DNP on larger samples, we will also make the best use of currently available power by implementing Teflon lenses and microwave resonators.

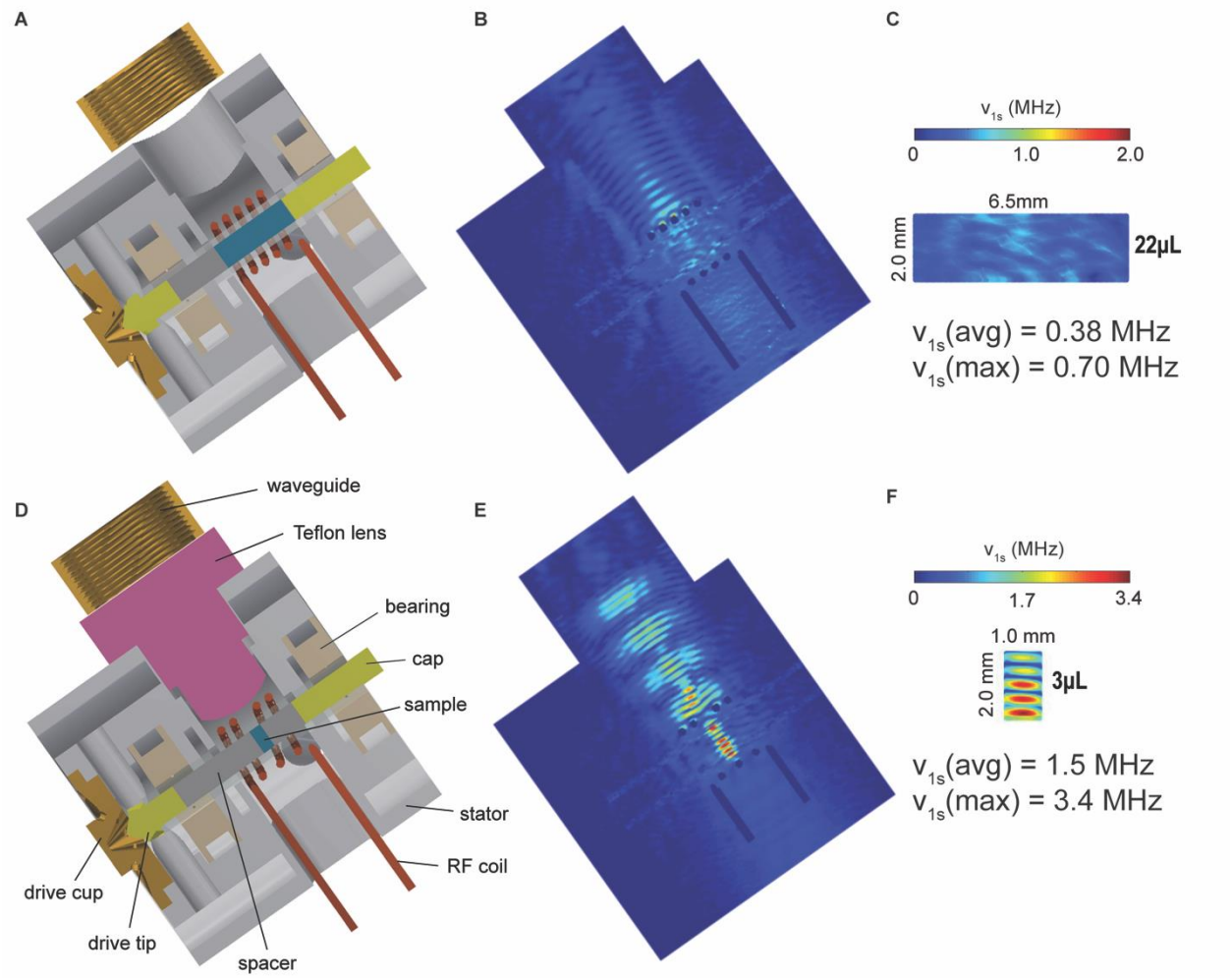

Figure 3.2 Microwave simulation of 3.2 mm cylindrical rotor in the stator with and without Teflon lens. (A) Schematics for a 3.2 mm cylindrical rotor inside the MAS stator. (B) HFSS of the setup shown in (A). (C) Expansion of the sample in (B). (D) Schematics showing the installation of the Teflon focusing lens. (E) HFSS of the setup in (D). (F) Expansion of the sample in (E).

Implementing Teflon lenses to focus power into 3.2 mm cylindrical rotors is challenged by not only diffraction through the RF coil, but also the steric hindrance of bringing the lens millimeters away from the rotor in order to maximize focusing. Therefore, we designed a 9.5 mm OD cylindrical rotor assembly that employs a Teflon lens within the rotor at the optimal distance to the sample (**Figure 3.3**).

3.3.2 Cylindrical Rotor with a 9.5 mm OD

Microwaves are introduced along the spinning axis in simulations of a 9.5 mm OD cylindrical rotor (**Figure 3.3 A**)[20,56]. The simulation includes the entire 9.5 mm OD cylindrical rotor, coil, waveguide, and also a thin copper disc between the drive tip and the sample for microwave reflection, which has been shown to improve DNP enhancements employing axial coupling[20,56]. Without a Teflon lens, the average simulated ν_{1s} of a 690 μL sample (ε_r=3.5) is 0.34 MHz (**Figure 3.3 B**). Although this ν_{1s} is sufficient to generate large DNP enhancements with the cross effect, which would result in very high signal-to-noise when combined with the large sample volume, there are considerable experimental challenges to spinning 9.5 mm cylindrical rotors for cryogenic MAS DNP. For instance, spinning frequencies of 9.5 mm cylindrical rotors are limited to roughly 4 kHz and it is difficult to generate the required RF field, ν_{1I}, for proton decoupling[52]. Cryogen consumption levels for cryogenic MAS of 9.5 mm OD cylinders would also be substantial.

However, we continued to explore microwave coupling into 9.5 mm rotors with the objective of performing pulsed DNP and electron decoupling at room temperature, which would not require cryogens for MAS. We decreased the sample volume in the 9.5 mm OD cylindrical rotors (**Figure 3.3 C**), with the idea of surrounding the sample with an inductively coupled magic angle spinning coil to improve RF performance[44,57]. The spacer on the sample holder was designed such that the sample could be placed at the optimal distance for the Teflon lens to focus microwaves. We determined the optimal distance by changing the distance between the Teflon lens and the sample in HFSS (**Figure 3.3 D-F**). A lens-sample distance of 3.5 mm was found to be the optimal separation, which yields an average ν_{1s} over a 2 μL sample volume of 2.7 MHz (**Figure 3.3 F**). We note this ν_{1s} is almost eight-times greater than the ν_{1s} over 690 μL of sample in the 9.5 mm

cylindrical rotor without a Teflon lens (**Figure 3.3 B**). However, we do note that maximum spinning frequency of this 9.5 mm OD cylindrical rotor apparatus is quite limited.

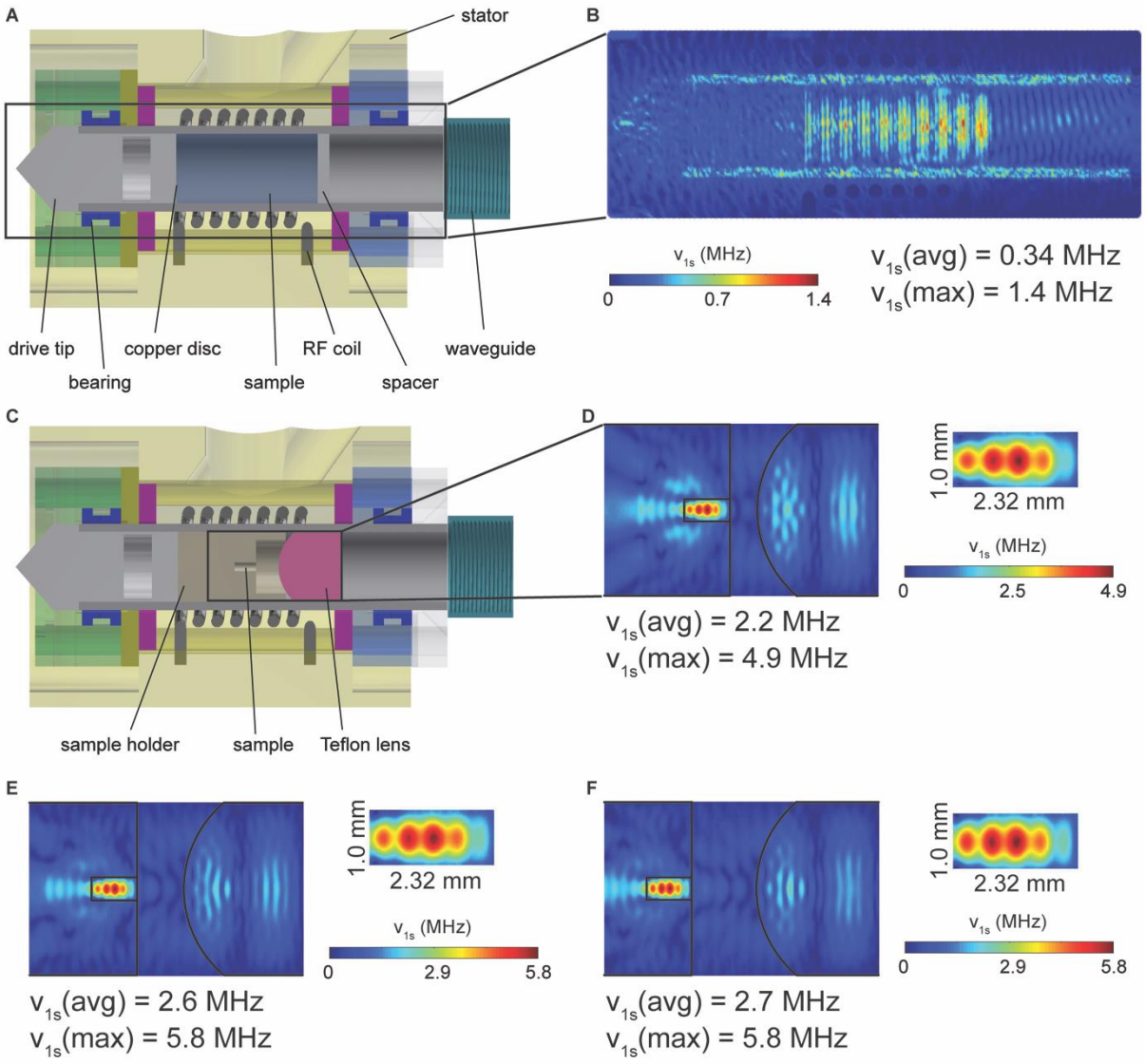

Figure 3.3 Teflon lens inserted in 9.5 mm OD cylindrical rotor to focus microwave irradiation. (A) Schematics of a 9.5 OD mm cylindrical rotor inside the MAS stator. (B) HFSS of setup in the box in (A). (C) Schematics of a 9.5 mm OD cylindrical rotor, MAS stator, and Teflon focusing lens. HFSS results of the setup in the box in (C) at a distance of (D) 1.5 mm, (E) 2.5 mm, and (F) 3.5 mm. The expansions indicate the microwave intensity only of the sample.

3.3.3 Spherical Rotor with a 9.5 mm OD

In order to access higher spinning frequencies and improve MAS instrumentation, we have recently introduced MAS spherical rotors[50]. Whereas 9.5 mm OD cylindrical rotors are typically

limited to 4 kHz spinning, we demonstrated 9.5 mm OD spherical rotors spinning stably at 10.6 kHz[50]. We therefore performed microwave analysis of spherical rotors. The analysis shown in **Figure 3.4 A** includes a Teflon lens within the waveguide to focus microwaves into 9.5 mm OD spherical rotors[50]. The zirconia spherical rotor (ε_r=20), two polyethylene plugs (ε_r=2.25), and a 161 μL sample were also included in the simulation (**Figure 3.4 A**). We found the average ν_{1s} to be 0.36 MHz over the 161 μL sample (**Figure 3.4 B**).

To improve the ν_{1s} in large volume spherical rotors, we devised a geometry which includes two Teflon lenses within the rotor (**Figure 3.4 C**). This assembly, with lenses on both spinning poles, is invariant to either orientation of the sphere with respect to the waveguide. The opposing lens also acts as a reflector to further increase the microwave intensity between the two lenses. The flat feature of the lenses on the exterior of the rotor reduces reflectance and increases microwave coupling into the spinning spheres. A Teflon lens (ε_r=2.1), zirconia spherical rotor (ε_r=20), interior polyethylene container (ε_r=2.25), and a 3 μL sample (ε_r=3.5) were included in the simulation. The average ν_{1s} is 2.5 MHz (**Figure 3.4 D**), almost seven-times greater than that in the 9.5 mm spherical rotor without the double lens insert (**Figure 3.4 B**). Although the ν_{1s} is improved to 2.5 MHz, and the filling factor of these geometries could be optimized with inductively coupled microcoils, the spinning frequency of the large 9.5 mm spherical rotors is currently limited to 10.6 kHz. Sub-millimeter spherical rotors are expected to achieve much higher spinning frequencies, and are also advantageous for microwave coupling.

3.3.4 Spherical Rotor with a 0.5 mm OD

The focused microwave intensity in **Figure 3.3 F** shows a spherical, not cylindrical distribution, of a tightly focused microwave beam. Indeed, the cross section of tightly focused electromagnetic radiation is a circle, not a rectangle. We therefore turned to spherical samples and rotors to match

the natural geometry of the microwave intensity. The sub-millimeter length scale of the spherical microwave intensity shown in **Figure 3.3 F** indicates an OD of 0.5 mm would result in effective overlap of the sample with the focused microwave beam.

We therefore turned to sub-millimeter spherical rotors to optimize microwave performance. Additionally, sub-millimeter cylindrical rotors enable spinning frequencies >110 kHz, which results in significant averaging of homonuclear proton interactions and pronounced improvements in NMR spectra[58]. The advantages of spherical rotors for MAS DNP with sub-millimeter diameters is therefore clear both in terms of electron paramagnetic resonance (EPR) performance (microwave control of electron spins) and NMR performance (spatial averaging of anisotropic interactions).

We also considered other materials for sub-millimeter spherical rotors with improved microwave transmission, thermal conduction, and mechanical strength. Yitria stabilized zirconia, sapphire, and silicon nitride are commonly employed in MAS rotors, but diamond has far superior material properties. Diamond is commonly employed in windows of megawatt gyrotrons due to both the extremely small loss tangent (5×10^{-5} at 145 GHz[59]), and also very high thermal conductivity (2400 W/m·K at 300 K, five-times higher than that of copper[59,60]). In addition to minimizing microwave losses and dissipating heat, the mechanical strength of diamond also will enable thinner rotor walls to improve sample filling factors.

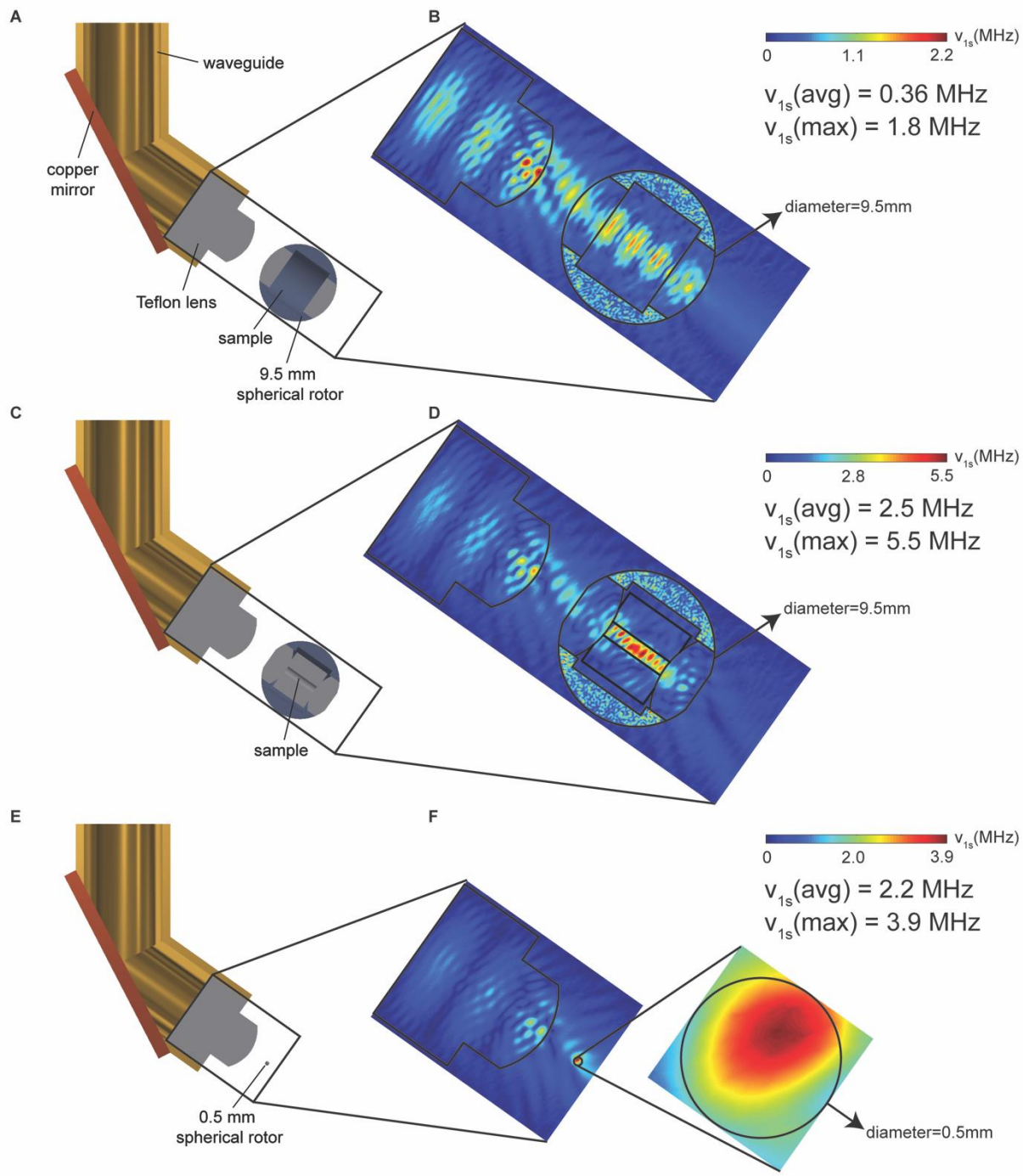

Figure 3.4 Focusing microwave irradiation into spherical rotors. (A) Schematics of waveguide, Teflon lens, and 9.5 mm spherical rotor. (B) Microwave analysis of the geometry shown in (A). (C) Schematics with the addition of the double lens insert. (D) Microwave analysis of the geometry shown in (C). The double lens insert helps further focus the microwave on the sample. (E) Schematics of waveguide, Teflon lens, and 0.5 mm OD spherical rotor. (F) Microwave analysis of the geometry shown in (E).

In this initial investigation into spherical diamond rotors for MAS DNP, we simulate a solid 0.5 mm OD diamond sphere (ε_r=5.7) (**Figure 3.4 E**). Cylindrical rotors with an OD of 0.5 mm have been successfully spun up to 126 kHz[61]. Applying MAS spheres at micron scales has considerable promise to access even higher spinning frequencies. The implementation of spherical diamond rotors for MAS will require cylindrical holes or hollowed cavities for sample loading. Due to the similar dielectric constants of diamond and glycerol-water, we expect the results shown in **Figure 3.4 F** will be generalizable to loaded spherical diamond rotors.

Microwave analysis shows an average ν_{1s} of 2.2 MHz with 5 W of microwave power (**Figure 3.4 F**). The ν_{1s} is far more homogenous in the sub-millimeter diamond sphere than larger geometries explored previously. Although adiabatic passages achieved with microwave chirped pulses are very robust to ν_{1s} inhomogeneity [46], we expect sub-millimeter sample geometries with improved ν_{1s} homogeneity to play an important role in the implementation of truly pulsed (i.e., hard pulses) EPR control with MAS. Finally, we note that sub-millimeter spherical rotors are a promising geometry for spherical dielectric microwave resonators, which could combine the advantages of microwave focusing from lenses with high quality factors.

3.5 Conclusions & Outlook

We analyze geometries that include Teflon lenses to couple microwave power into both cylindrical and spherical rotors for MAS-DNP. HFSS was used to simulate the microwave distribution and calculate the ν_{1s}. **Table 3.1** summarizes the ν_{1s} of the simulated geometries. The computed ν_{1s} of a 3.2 mm OD cylindrical rotor without and with a Teflon focusing lens was 0.38 MHz and 1.5 MHz, respectively. The computed ν_{1s} over 690 μL of sample within a 9.5 mm OD cylindrical rotor is 0.34 MHz, while implementing a Teflon lens increases the ν_{1s} to 2.7 MHz, albeit with a reduced

sample size of 2 μL. We also analyzed 9.5 mm OD spherical rotors. The computed ν_{1s} is 0.36 MHz with a Teflon focusing lens exterior to the rotor, and 2.5 MHz with a double lens insert. A 0.5 mm OD diamond spherical rotor was also analyzed to combine advantages of high electron Rabi frequencies with high spinning frequencies. The computed ν_{1s} of the 0.5 mm OD diamond sphere was 2.2 MHz using a Teflon focusing lens.

DNP has already shown promise scaling to higher magnetic fields. For example, in addition to DNP performed at 900 MHz[62], a gyrotron operating in the 2nd harmonic has already demonstrated microwave power output of 5-10 W at a frequency of 0.8 THz, suitable for DNP at 28 Tesla (1.2 GHz ^{1}H frequency) using a novel double-electron beam magnetron injection gun[63]. The microwave beam will be able to be focused to even smaller volume at higher frequencies due to the inverse scaling of wavelength. All of the microwave simulations in this study employed a nominal input of 5 W of microwave power. However, these results are general and scalable to higher microwave powers. For instance, we are currently constructing a frequency-tunable gyrotron which is modeled to produce 400 W of microwave power at 198 GHz. Assuming 3 dB loss during transmission to the probe and 200 W of incident microwave power, we expect the ν_{1s} within 0.5 mm OD diamond spheres to increase to ν_{1s} = 14 MHz. Access to such high electron Rabi frequencies is expected to play a pivotal role in the implementation of time domain DNP, improved electron decoupling, and a new suite of coherent EPR pulse sequences for MAS NMR spectroscopy.

Table 3.1 Summary of computed electron Rabi frequencies ν_{1s} with a nominal microwave power of 5 W within different MAS rotors.

	3.2 mm cylindrical rotor		9.5 mm cylindrical rotor		9.5 mm spherical rotor		0.5 mm sphere
	No Lens	Lens	No Lens	Lens	Lens	Double lens	Lens
Average ν_{1s} (MHz)	0.38	1.5	0.34	2.7	0.36	2.5	2.2
Maximum ν_{1s} (MHz)	0.70	3.4	1.4	5.8	1.8	5.5	3.9

3.6 References

1. Retel, J. S. *et al.* Structure of outer membrane protein G in lipid bilayers. *Nat. Commun.* **8**, 1–10 (2017).

2. Eddy, M. T. *et al.* Magic angle spinning nuclear magnetic resonance characterization of voltage-dependent anion channel gating in two-dimensional lipid crystalline bilayers. *Biochemistry* **54**, 994–1005 (2015).

3. Ni, Q. Z. *et al.* Primary Transfer Step in the Light-Driven Ion Pump Bacteriorhodopsin: An Irreversible U-Turn Revealed by Dynamic Nuclear Polarization-Enhanced Magic Angle Spinning NMR. *J. Am. Chem. Soc.* **140**, 4085–4091 (2018).

4. McDermott, A. Structure and Dynamics of Membrane Proteins by Magic Angle Spinning Solid-State NMR. *Annu. Rev. Biophys.* **38**, 385–403 (2009).

5. Yang, H. *et al.* REDOR NMR reveals multiple conformers for a protein kinase c ligand in a membrane environment. *ACS Cent. Sci.* **4**, 89–96 (2018).

6. Baker, L. A. *et al.* Combined ^{1}H-Detected Solid-State NMR Spectroscopy and Electron Cryotomography to Study Membrane Proteins across Resolutions in Native Environments. *Structure* **26**, 161-170.e3 (2018).

7. Renault, M. *et al.* Solid-state NMR spectroscopy on cellular preparations enhanced by dynamic nuclear polarization. *Angew. Chemie - Int. Ed.* **51**, 2998–3001 (2012).

8. Kaplan, M. *et al.* Probing a cell-embedded megadalton protein complex by DNP-supported solid-state NMR. *Nat. Methods* **12**, 649–652 (2015).

9. Ni, Q. Z. *et al.* High frequency dynamic nuclear polarization. *Acc. Chem. Res.* **46**, 1933–1941 (2013).

10. Rossini, A. J., Zagdoun, A., Lelli, M., Lesage, A. & Cop, C. Dynamic Nuclear Polarization Surface Enhanced NMR Spectroscopy. *Acc. Chem. Res.* **46**, (2013).

11. Tycko, R. NMR at Low and Ultralow Temperatures. *Acc. Chem. Res.* **46**, 1923–1932 (2013).

12. Maly, T. *et al.* Dynamic nuclear polarization at high magnetic fields. *J. Chem. Phys.* **052211**, (2008).

13. Barnes, A. B. *et al.* High-field dynamic nuclear polarization for solid and solution biological NMR. *Appl. Magn. Reson.* **34**, 237–263 (2008).

14. Can, T. V., Ni, Q. Z. & Griffin, R. G. Mechanisms of dynamic nuclear polarization in insulating solids. *J. Magn. Reson.* **253**, 23–35 (2015).

15. Lilly Thankamony, A. S., Wittmann, J. J., Kaushik, M. & Corzilius, B. Dynamic nuclear polarization for sensitivity enhancement in modern solid-state NMR. *Prog. Nucl. Magn. Reson. Spectrosc.* **102**–**103**, 120–195 (2017).

16. Becerra, L. R., Gerfen, G. J., Temkin, R. J., Singel, D. J. & Griffin, R. G. Dynamic nuclear polarization with a cyclotron resonance maser at 5 T. *Phys. Rev. Lett.* **71**, 3561–3564 (1993).

17. Lelli, M. *et al.* Solid-State Dynamic Nuclear Polarization at 9.4 and 18.8 T from 100 K to Room Temperature. *J. Am. Chem. Soc.* **137**, 14558–14561 (2015).

18. Akbey, Ü. *et al.* Dynamic nuclear polarization of deuterated proteins. *Angew. Chemie - Int. Ed.* **49**, 7803–7806 (2010).

19. Sauvøe, C. *et al.* Highly Efficient , Water-Soluble Polarizing Agents for Dynamic Nuclear Polarization at High Frequency. *Angew. Chemie Int. Ed.* **52**, 10858–10861 (2013).

20. Afeworki, M., McKay, R. A. & Schaefer, J. Dynamic nuclear polarization enhanced nuclear magnetic resonance of polymer-blend interfaces. *Mater. Sci. Eng. A* **162**, 221–228 (1993).

21. Afeworki, M., Schaefer, J. & Vega, S. Direct Electron-to-Carbon Polarization Transfer in Homogeneously Doped Polycarbonates. *Macromolecules* **25**, 4100–4105 (1992).

22. Afeworki, M. & Schaefer, J. Mechanism of DNP-Enhanced Polarization Transfer across the Interface of Polycarbonate/Polystyrene Heterogeneous Blends. *Macromolecules* **25**, 4092–4096 (1992).

23. Saliba, E. P., Sesti, E. L., Alaniva, N. & Barnes, A. B. Pulsed Electron Decoupling and Strategies for Time Domain Dynamic Nuclear Polarization with Magic Angle Spinning. *J. Phys. Chem. Lett.* **9**, 5539–5547 (2018).

24. Saliba, E. P. *et al.* Electron Decoupling with Dynamic Nuclear Polarization in Rotating Solids. *J. Am. Chem. Soc.* **139**, 6310–6313 (2017).

25. Henstra, A., Dirksen, P. & Wenckebach, W. T. Enhanced dynamic nuclear polarization by the integrated solid effect. *Phys. Lett. A* **134**, 134–136 (1988).

26. Can, T. V., Weber, R. T., Walish, J. J., Swager, T. M. & Griffin, R. G. Frequency-Swept Integrated Solid Effect. *Angew. Chemie - Int. Ed.* **56**, 6744–6748 (2017).

27. Can, T. V. *et al.* Frequency-Swept Integrated and Stretched Solid Effect Dynamic Nuclear Polarization. *J. Phys. Chem. Lett.* **9**, 3187–3192 (2018).

28. Henstra, A. & Wenckebach, W. T. The theory of nuclear orientation via electron spin locking (NOVEL). *Mol. Phys.* **106**, 859–871 (2008).

29. Can, T. V., Walish, J. J., Swager, T. M. & Griffin, R. G. Time domain DNP with the NOVEL sequence. *J. Chem. Phys.* **143**, 1–8 (2015).

30. Jain, S. K., Mathies, G. & Griffin, R. G. Off-resonance NOVEL. *J. Chem. Phys.* **147**, (2017).

31. Rizzato, R. & Bennati, M. Cross-Polarization Electron-Nuclear Double Resonance Spectroscopy. *ChemPhysChem* **16**, 3769–3773 (2015).

32. Weis, V. & Griffin, R. G. Electron-nuclear cross polarization. *Solid State Nucl. Magn. Reson.* **29**, 66–78 (2006).

33. Tan, K. O., Yang, C., Weber, R. T., Mathies, G. & Griffin, R. G. Time-optimized pulsed dynamic nuclear polarization. *Chemcial Phys.* **5**, 1–8 (2019).

34. Alberti, S. *et al.* Nanosecond Pulses in a THz Gyrotron Oscillator Operating in a Mode-Locked Self-Consistent Q -Switch Regime. *Phys. Rev. Lett.* **111**, 1–5 (2013).

35. Takahashi, S. *et al.* pulsed electron paramagnetic resonance spectroscopy powered by a free-electron laser. *Nature* **489**, 409–413 (2012).

36. V.S. Bajaj, C.T. Farrar, M.K. Hornstein, I. Mastovsky, J. Vieregg, J. Bryant, B. Elena, K.E. Kreischer, R.J. Temkin, R. G. G. & A. Dynamic nuclear polarization at 9T using a novel 250 gyrotron microwave source. *J. Magn. Reson.* **160**, 85–90 (2003).

37. Torrezan, A. C. *et al.* Continuous-wave operation of a frequency-tunable 460-GHz second-harmonic gyrotron for enhanced nuclear magnetic resonance. *IEEE Trans. Plasma Sci.* **38**, 1150–1159 (2010).

38. Barnes, A. B., Nanni, E. A., Herzfeld, J., Griffin, R. G. & Temkin, R. J. A 250 GHz gyrotron with a 3 GHz tuning bandwidth for dynamic nuclear polarization. *J. Magn. Reson.* **221**, 147–153 (2012).

39. Alberti, S. *et al.* Experimental study from linear to chaotic regimes on a terahertz-frequency gyrotron oscillator. *Phys. Plasmas* **19**, (2012).

40. Yoon, D. *et al.* Dynamic nuclear polarization by frequency modulation of a tunable gyrotron of 260 GHz. *J. Magn. Reson.* **262**, 62–67 (2016).

41. Matsuki, Y., Idehara, T., Fukazawa, J. & Fujiwara, T. Advanced instrumentation for DNP-enhanced MAS NMR for higher magnetic fields and lower temperatures. *J. Magn. Reson.* **264**, 107–115 (2016).

42. Scott, F. J. *et al.* Frequency-agile gyrotron for electron decoupling and pulsed dynamic nuclear polarization. *J. Magn. Reson.* **289**, 45–54 (2018).

43. Denysenkov, V. & Prisner, T. Liquid state Dynamic Nuclear Polarization probe with Fabry-Perot resonator at 9.2 T. *J. Magn. Reson.* **217**, 1–5 (2012).

44. Kiss, S. Z. *et al.* A microwave resonator integrated on a polymer microfluidic chip. *J. Magn. Reson.* **270**, 169–175 (2016).

45. Scott, F. J. *et al.* Magic angle spinning NMR with metallized rotors as cylindrical microwave resonators. *Magn. Reson. Chem.* **56**, 831–835 (2018).

46. Nanni, E. A. *et al.* Microwave field distribution in a magic angle spinning dynamic nuclear polarization NMR probe. *J. Magn. Reson.* **210**, 16–23 (2011).

47. Purea, A. *et al.* Improved waveguide coupling for 1 . 3 mm MAS DNP probes at 263 GHz. *J. Magn. Reson.* **302**, 43–49 (2019).

48. Sesti, E. L. *et al.* Magic Angle Spinning NMR Below 6 K with a Computational Fluid Dynamics Analysis of Fluid Flow and Temperature Gradients. *J. Magn. Reson.* **286**, 1–9 (2017).

49. Lowe, I. J. Free induction decays of rotating solids. *Phys. Rev. Lett.* **2**, 285–287 (1959).

50. Chen, P. *et al.* Magic angle spinning spheres. *Sci. Adv.* 1–8 (2018). doi:10.1126/sciadv.aau1540

51. Hoff, D. E. M. *et al.* Frequency swept microwaves for hyperfine decoupling and time domain dynamic nuclear polarization. *Solid State Nucl. Magn. Reson.* **72**, 79–89 (2015).

52. Scott, F. J. *et al.* A Versatile Custom Cryostat for Dynamic Nuclear Polarization Supports Multiple Cryogenic Magic Angle Spinning Transmission Line Probes. *J. Magn. Reson.* **297**, 23–32 (2018).

53. Jiang, J. H. & Wu, D. L. Ice and water permittivities for millimeter and sub-millimeter remote sensing applications. *Atmos. Sci. Lett.* **5**, 146–151 (2004).

54. Lamb, J. Miscellaneous data on materials for millimetre and submillimetre optics. *Int. J. Infrared Millim. Waves* **17**, 1997–2034 (1996).

55. Carroll A., Eaton S., Eaton G., Z. K. *Characterizing Microwave Efficiency in DNP Instrumentation by Frequency Swept EPR. 59th Rocky Moutain Conference on Magnetic Resonance* **7426**, (2018).

56. Pike, K. J. *et al.* A spectrometer designed for 6.7 and 14.1 T DNP-enhanced solid-state MAS NMR using quasi-optical microwave transmission. *J. Magn. Reson.* **215**, 1–9 (2011).

57. Sakellariou, D., Goff, G. Le & Jacquinot, J. F. High-resolution, high-sensitivity NMR of nanolitre anisotropic samples by coil spinning. *Nature* **447**, 694–697 (2007).

58. Xue, K. *et al.* Magic-Angle Spinning Frequencies beyond 300 kHz Are Necessary to Yield Maximum Sensitivity in Selectively Methyl Protonated Protein Samples in Solid-State NMR. *J. Phys. Chem. C* **122**, 16437–16442 (2018).

59. Materials, D. The CVD diamond booklet. *Online Cat.* 4 (2014).

60. Graebner, J. E. Thermal Conductivity of Diamond BT - Diamond: Electronic Properties and Applications. in (eds. Pan, L. S. & Kania, D. R.) 285–318 (Springer US, 1995). doi:10.1007/978-1-4615-2257-7_7

61. Penzel, S. *et al.* Spinning faster : protein NMR at MAS frequencies up to 126 kHz. *J. Biomol. NMR* **0**, 0 (2019).

62. Björgvinsdóttir, S., Walder, B. J., Pinon, A. C., Yarava, J. R. & Emsley, L. DNP enhanced NMR with flip-back recovery. *J. Magn. Reson.* **288**, 69–75 (2018).

63. Idehara, T. *et al.* A novel THz-band double-beam gyrotron for high-field DNP-NMR spectroscopy. *Rev. Sci. Instrum.* **88**, (2017).

Chapter 4: Magic Angle Spinning Micron Spheres for Nuclear Magnetic Resonance

In solid-state NMR, magic angle spinning (MAS), which can partially average anisotropic spin interactions, is commonly used to improve sensitivity and spectral resolution. While cylindrical rotors have conventionally been used for MAS NMR, spherical rotors have been demonstrated to spin stably at the magic angle and exhibit several advantages over cylindrical rotors. 9.5 mm outer diameter (OD) and 4 mm OD spherical rotors can be spun at 10.6 kHz and 28 kHz, respectively using He (g). Given the advantages of faster spinning in NMR and the ability to spin smaller rotors faster, 240 μm OD spherical rotors and stators were fabricated by three-dimensional direct laser writing (3D-DLW). In order to effectively house the sub-millimeter stators, novel microstructures were fabricated by ultraviolet (UV) lithography. Additionally, potential future designs are discussed to improve MAS DNP NMR instrumentation.

4.1 Introduction

Nuclear magnetic resonance (NMR) spectroscopy is a powerful analytical tool capable of investigating molecular structure and dynamics of liquids and solids with atomic resolution. In solid-state NMR, magic angle spinning (MAS) can partially average anisotropic spin interactions in the magnetic resonance Hamiltonian by mechanically rotating the sample an axis of 54.7° with respect to the external magnetic field[1–4]. The spatial averaging in MAS improves sensitivity and spectral resolution in solid-state NMR; therefore, MAS NMR has been used to characterize diverse biological samples and molecular architectures[5–13].

Cylindrical rotors are conventionally used for MAS[14–17]; however, MAS spherical rotors that exhibit several advantages over cylindrical rotors have been introduced recently to spin stably at

the magic angle[18]. Spherical rotors require only a single gas stream that serves as bearing gas to suspend the rotor, drive gas to spin the rotor, and variable temperature line to regulate sample temperature. Moreover, implementation of spherical rotors enables better microwave illumination and a simplified vertical sample exchange for cryogenic dynamic nuclear polarization (DNP). 9.5 mm outer diameter (OD) spherical rotors can be spun stably at the magic angle up to 10.6 kHz with He (g)[18]. Scaling the spherical rotor OD down to 4 mm enables a higher spinning frequency at 28 kHz[19]. Access to sub-millimeter cylindrical rotors can significantly average homonuclear proton interactions, leading to pronounced improvements in NMR spectra[20,21]. Cylindrical rotors with an OD of 0.5 mm have been successfully spun up to 126 kHz[21]. Sub-millimeter spherical rotors have not been reported yet. Ultra-fast, stable MAS on sub-millimeter spherical rotors is promising to substantially improve the spectral resolution and sensitivity in solid-state NMR.

In addition to achieving fast and stable spinning, effective microwave coupling into the sample must also be considered in MAS DNP instrumentation. Dielectric lenses for cylindrical and spherical MAS rotors have been analyzed to increase the electron Rabi frequency[22]. Based on the simulations, the focused microwave intensity displays a spherical distribution rather than a cylindrical one (**Figure 3.3 F** and **Figure 3.4 F**). A potential strategy to increase the electron Rabi frequency is to create a resonant cavity within the sphere body. Based on the tightly focused microwave beam shown in the simulations, 240 μm was chosen here to be the OD of the spherical rotor.

Sub-millimeter spherical rotors and stators are difficult to fabricate due to high-precision requirements. Implementing sub-millimeter spherical rotors and stators in the NMR probe is also challenging because observing and handling them without a microscope is nearly impossible. Here, three-dimensional direct laser writing (3D-DLW, Photonic Professional GT; Nanoscribe GmbH,

Germany), which provides the desired precision, was used to fabricate these 240 µm spherical rotors and stators. In order to effectively house the 240 µm stators in the MAS DNP NMR probe, an adaptor consisting of microstructures was designed to interface the 240 µm stator with the MAS DNP NMR probe.

4.2 Materials and Methods

4.2.1 Three-dimensional Direct Laser Writing (3D-DLW)

Sub-millimeter spherical rotors and stators (**Figure 4.1**) are fabricated by 3D-DLW, which provides the desired precision for 3D polymer nano- and microstructures[23–25]. With this method, a laser beam (780 nm) is focused on a diffraction-limited spot within a volume of a photoresist, which is a light-sensitive material that can be cross-linked after exposed to the light. By applying two-photon absorption, this volume can be restricted to a voxel, a small volume element[23,26,27]. The precision is determined by the laser beam waist that is usually several hundreds of nanometers. 3D-DLW can achieve arbitrary nano- and microstructures by scanning in three dimensions. The writing time, depending on the volume and the filling factor of the structure, is usually within a few hours, which allows relatively quick prototyping. However, the sample size is limited by the field of view of the objective lens on the microscope.

During 3D-DLW, IP-S photoresists (Nanoscribe GmbH, Germany) and indium-tin-oxide-(ITO) coated glass substrates (Nanoscribe GmbH, Germany) were chosen to fabricate 240 µm spherical rotors and stators. After the microstructures were fabricated, they were developed in propylene glycol methyl ether acetate (PGMEA) and isopropyl alcohol (IPA) to remove photoresist residues. After fabrication, scanning electron microscopy (SEM) was used to examine the microstructures.

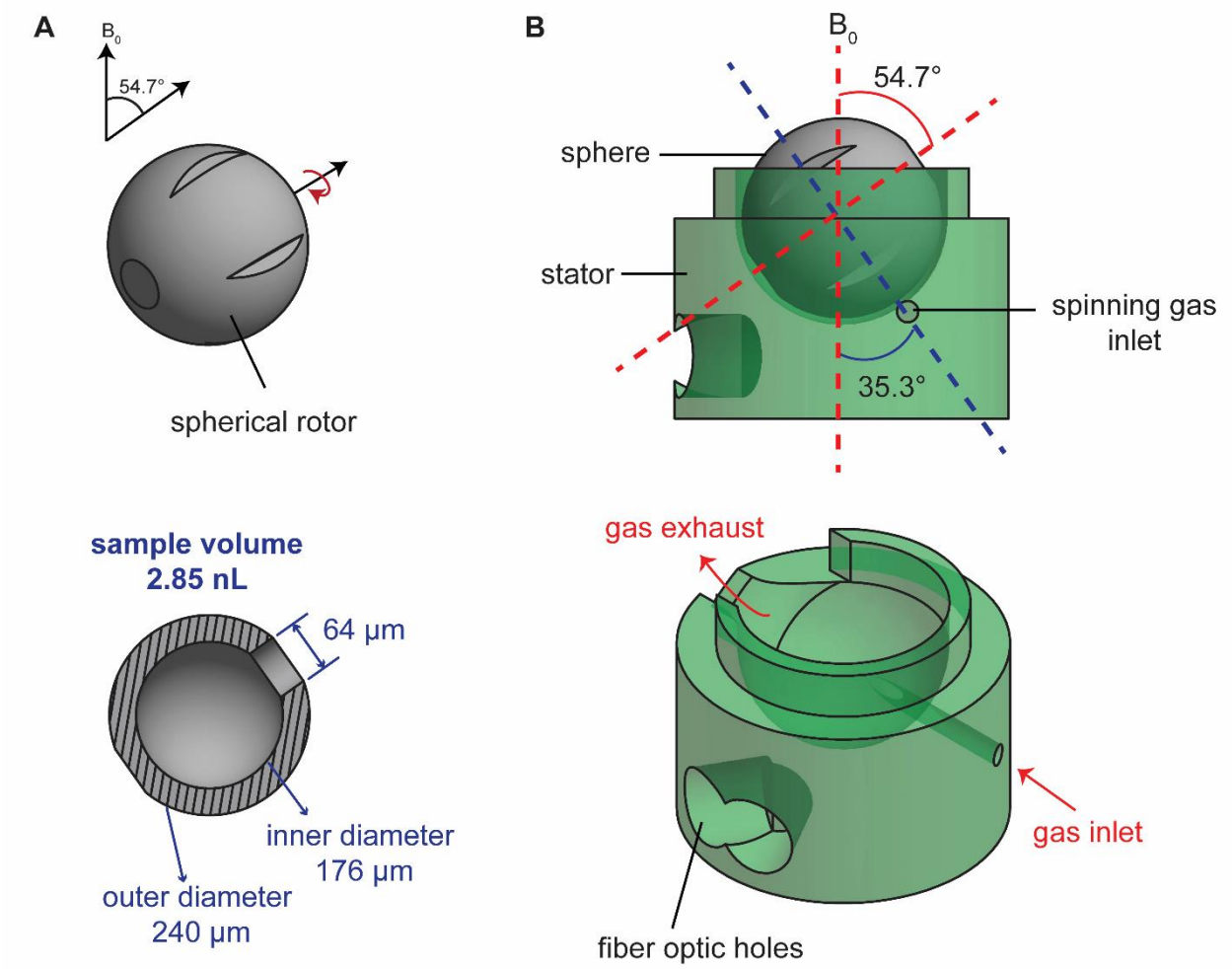

Figure 4.1 240 µm spherical rotor and stator for MAS DNP NMR. (A) 240 µm OD spherical rotor with a sample volume of 2.85 nL. (B) The stator with a single gas stream at the complement of the magic angle can spin the sphere at the magic angle.

4.2.2 Ultraviolet (UV) Lithography

An adaptor was designed and fabricated to interface the 240 µm stator with the MAS DNP NMR probe. This adaptor improves handling of the sub-millimeter stator as well as facilitates access to the gas inlet of the stator. Additional holes for fiber optics that enable spinning frequency detection were also considered in this adaptor. The adaptor consists of a 10mm×10mm, 500 µm-thick, glass substrate and a patterned structure fabricated by ultraviolet (UV) lithography (**Figure 4.2 A-E**). After UV lithography, the stator was fabricated by performing 3D-DLW in the cylindrical cut (**Figure 4.2 F**). The cross section of the gas inlet on the adaptor was designed to be >50 times

larger than the cross section of the gas inlet on the 240 µm stator to avoid the necessity of perfectly aligning the gas inlets (**Figure 4.2 F**). Even if the alignment is slightly off, the gas can be directed into the stator. The cross sections of the gas inlet and the fiber optic holes on the adaptor were designed to be rectangular instead of circular for effective lithography fabrication.

With UV lithography, dry, negative photoresists (Ordyl SY 320 and SY 390, Elga Europe, Italy) with thicknesses of 20 µm and 90 µm were combined to fabricate the gas inlet and the fiber optic holes on 500 µm-thick, 4-inch glass wafers (**Figure 4.2 A-E**). For a standard process, the dry photoresist was first laminated at 85 °C on the glass wafer. Then, the dry photoresist was exposed to the UV beam (365 nm) through a photo-mask using a mask aligner (EVG 620, EV Group). The exposed photoresist, not covered by the mask, is cross-linked. Exposure doses of 180mJ/cm^2 and 225mJ/cm^2 were used for 90µm- and 110µm-thick photoresist layers, respectively. Then, the sample was soaked in an Ordyl developer (Elga Europe, Italy) in an ultrasonic bath to remove the non-cured photoresist following by 5 minutes of hard-bake at 150 °C to alleviate any residual stress in the structure. In order to fabricate the adaptor, four different masks are required and a similar process has been achieved for each individual mask (**Figure 4.2 B-E**). 25 adaptors can be fabricated on a 4-inch glass wafer.

After these UV lithography steps, the samples were diced into 10mm×10mm pieces by a dicing machine (DAD 3430, DISCO, Japan). Then, the 240 µm stator was fabricated on each 10mm×10mm adaptor using 3D-DLW (**Figure 4.2 F**). In this case, the stator is directly housed on the adaptor after 3D-DLW.

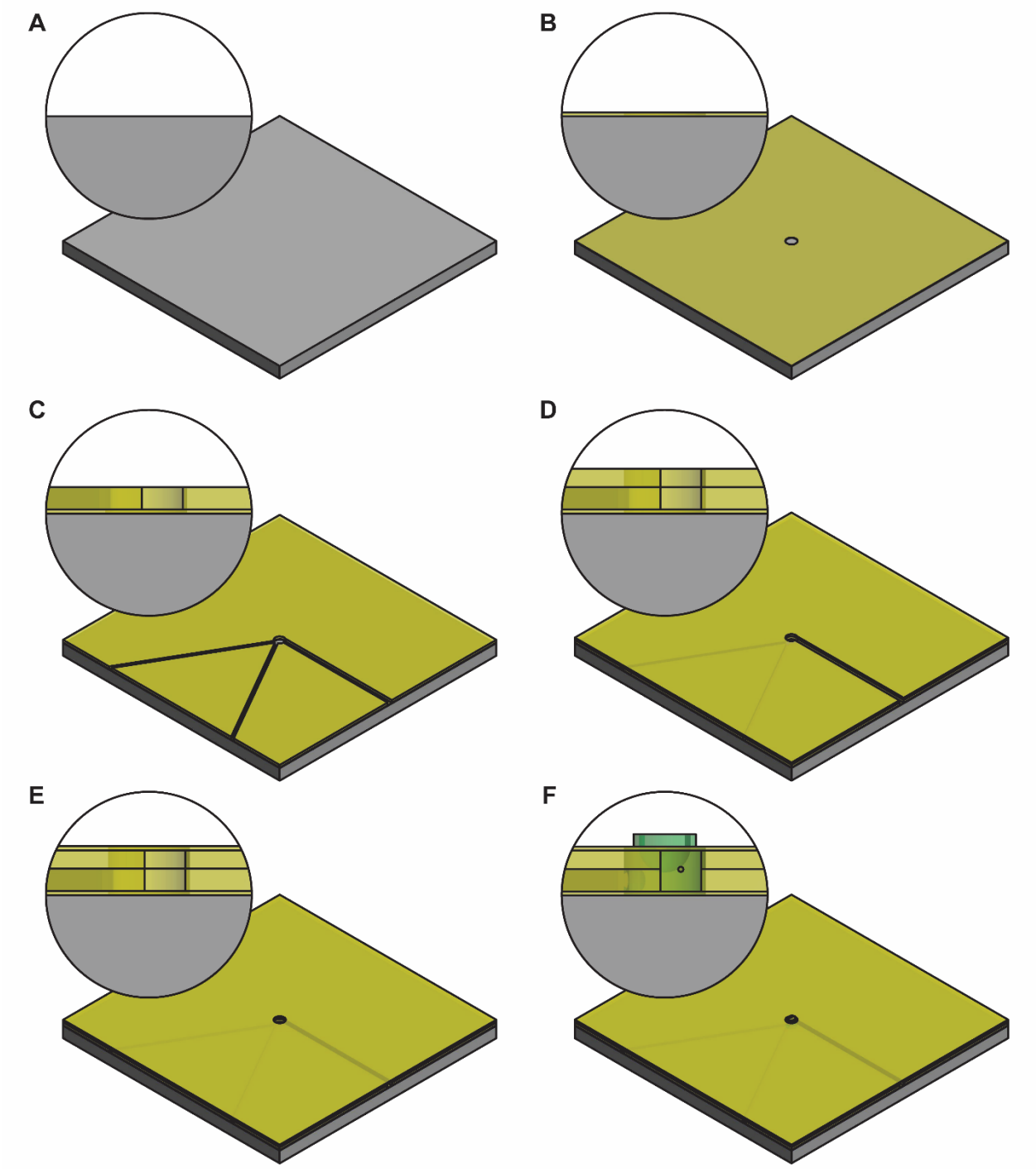

Figure 4.2 Schematic illustrations of the microstructure fabrication by UV lithography and 3D-DLW. (A) A 10mm×10mm glass substrate. (B) First-layer dry photoresist with a 400 μm OD cut for the stator. (C) Second-layer dry photoresist with the cut, the gas inlet and fiber optic holes. (D) Third-layer dry photoresist with the cut and the gas inlet. (E) Fourth-layer dry photoresist only with the cut to seal the gas inlet. (F) The stator fabricated by 3D-DLW.

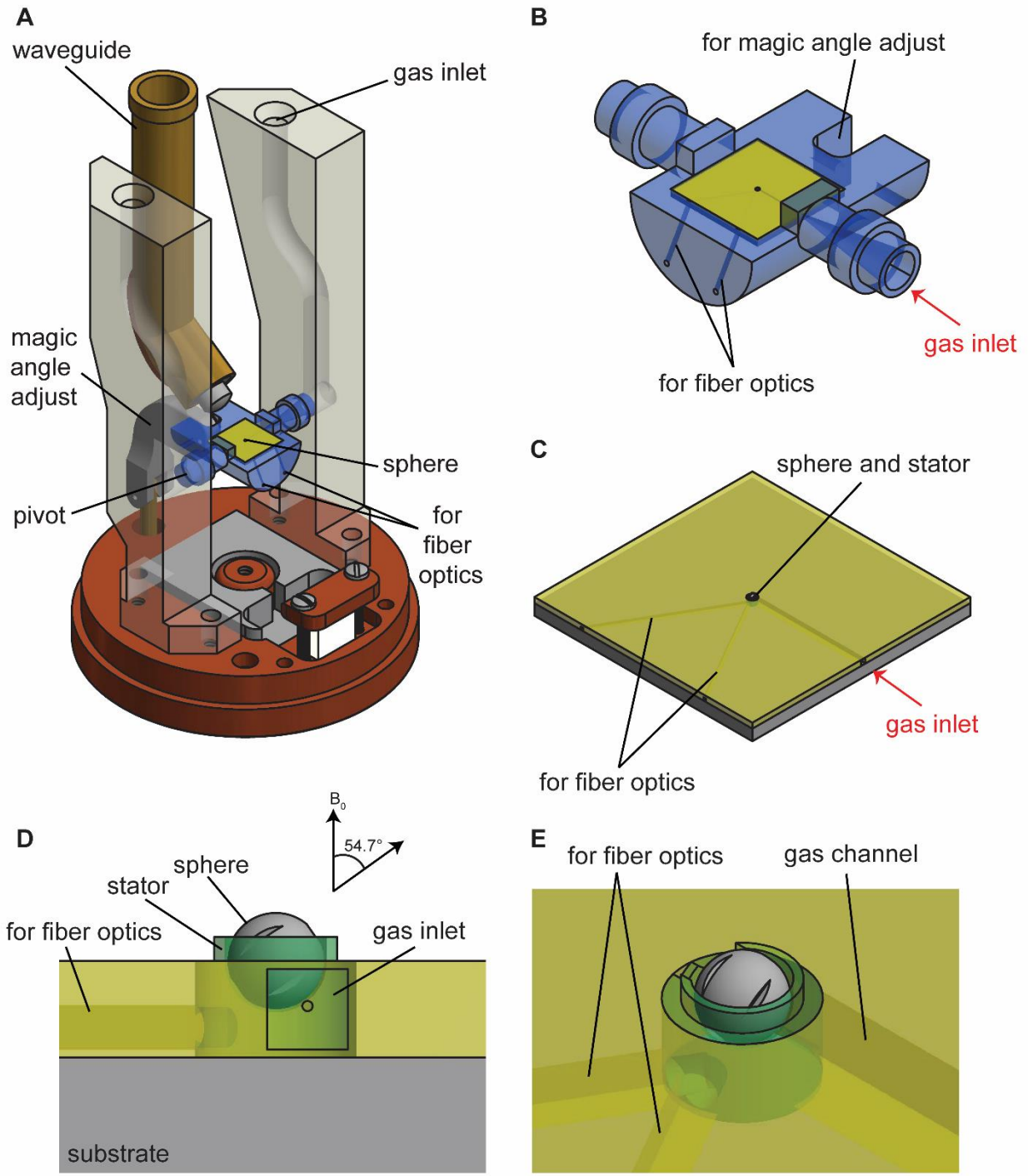

Figure 4.3 Implementation of spheres into a transmission-line probe for MAS DNP NMR. (A) The NMR probe head contains a gas inlet for spinning, fiber optics for spinning frequency detection, and magic angle adjustment. The pivots of the 3D printed part serve as pivot points for magic angle adjustment. The 3D-printed part also provides the gas inlet to spin the spheres. (B) Expansion of the 3D-printed part. (C) The adaptor contains the microstructures for spinning gas and fiber optics. (D) Expansion of the adaptor shows how the 240 µm OD spherical rotor and the stator are housed. (E) An isometric view of the adaptor, the spherical rotor, and the stator.

4.2.3 Implementation in MAS DNP NMR Probe

The NMR probe head includes a gas inlet for spinning, fiber optics for spinning frequency detection, and magic angle adjustment (**Figure 4.3 A**). The pivots of the 3D printed part serve as the gas inlet and as the pivot point for the magic angle adjustment. The 10mm×10mm cut on the 3D-printed part is designed to house the adaptor that contains the microstructure (**Figure 4.3 B**). The adaptor contains the stator for spinning the 240 μm OD spherical rotor, the gas inlet for spinning, and the fiber optic holes for spinning frequency detection (**Figure 4.3 C-E**).

4.3 Results and Discussion

4.3.1 240 μm OD Spherical Rotor and Stators

The 240 μm OD spherical rotor was scaled down from the 4 mm OD spherical rotor[19] and modified to contain more sample volume (**Figure 4.1 A**). Grooves are directly fabricated on the sphere, convert the rotor body into a robust turbine with high torque, and establish a preferred axis of rotation about a single axis. The 240 μm stator, which was modified from the 9.5 mm stator[18], introduces the gas at the complement of the magic angle, 35.3°, and spins the spherical rotor at the magic angle, 54.7° (**Figure 4.1 B**).

When fabricating 240 μm spherical rotors and stators by 3D-DLW, we use the software DeScribe (Nanoscribe GmbH, Germany), which converts computer-assisted design (CAD) files to machine-readable files. In DeScribe, the main parameters that determine the surface quality are hatching and slicing. Hatching defines the lateral print resolution, while slicing defines the print resolution in the z-direction. The hatch and slice thicknesses change the surface roughness of the microstructures, thus influencing the spinning; therefore, choosing the appropriate hatch and slice thicknesses is important. Retaining the hatch thickness as 0.5 μm, we varied the slice thickness to optimize the smoothness. From some preliminary results (not shown here), a slice thickness larger

than 0.5 μm is not ideal because the surface roughness is clearly visible. Here, spherical rotors containing a slice thickness of 0.1 μm and 0.25 μm were investigated. In order to control the quality of the spherical rotors, 16 of each were fabricated by 3D-DLW and examined by SEM. **Figure 4.4** displays SEM images for a selection of those spherical rotors with a slice thickness of 0.1 μm or 0.25 μm. The cloudy features on the spherical rotors are some residues from the drying process and usually do not affect the functionality.

Before fabricating 240 μm stators directly on the adaptor, we fabricated them on an empty ITO-coated glass substrate and examined the quality by SEM. **Figure 4.5** shows the SEM images for a 240 μm stator with a slice thickness of 0.25 μm, indicating that the gas inlet, the gas exhaust, and the fiber optic holes can be fabricated by 3D-DLW.

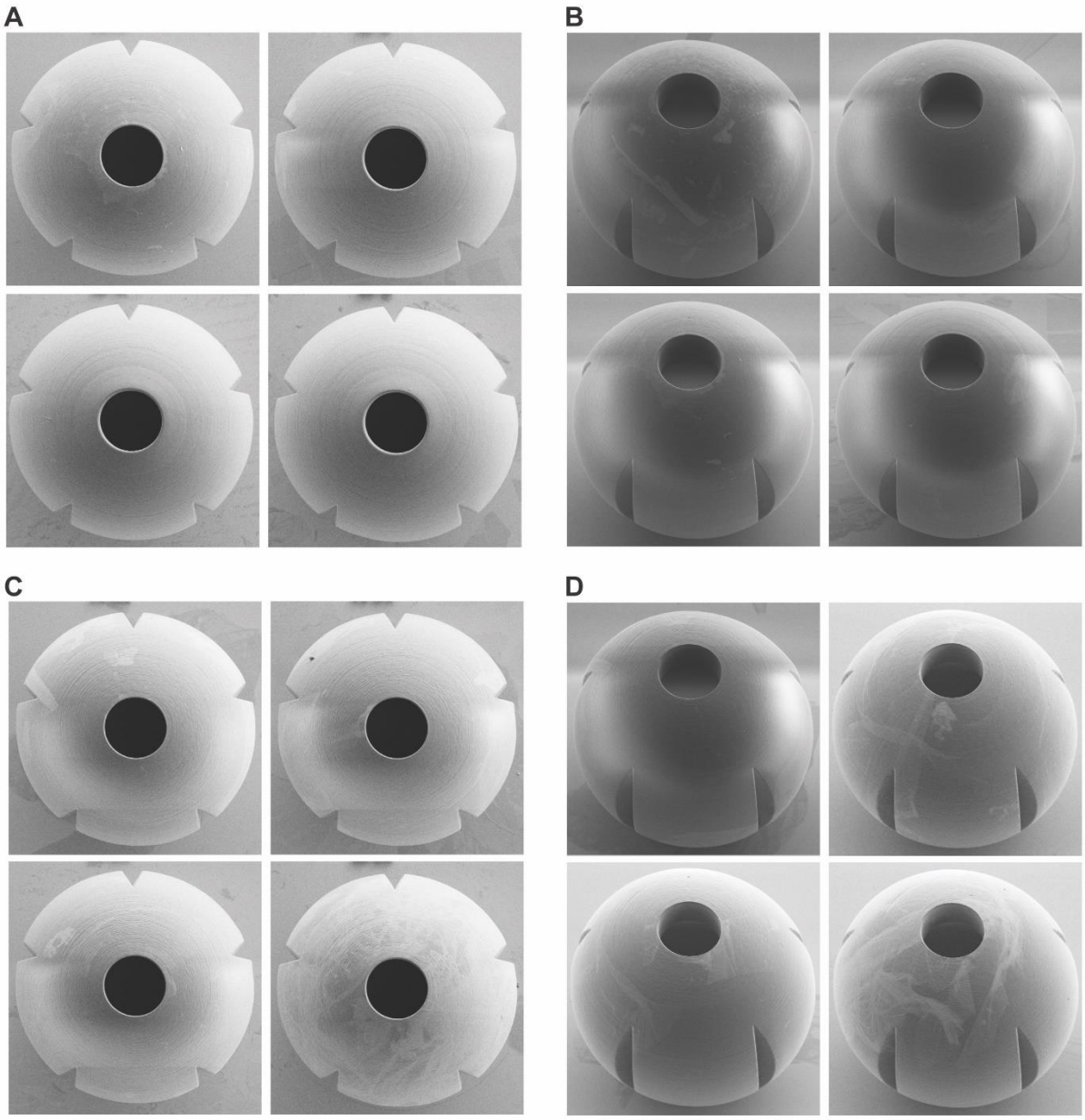

Figure 4.4 SEM images for a selection of 240 µm OD spherical rotors with a slice thickness of 0.1 µm or 0.25 µm. (A) and (B) spherical rotors with a slice thickness of 0.1 µm. (C) and (D) spherical rotors with a slice thickness of 0.25 µm.

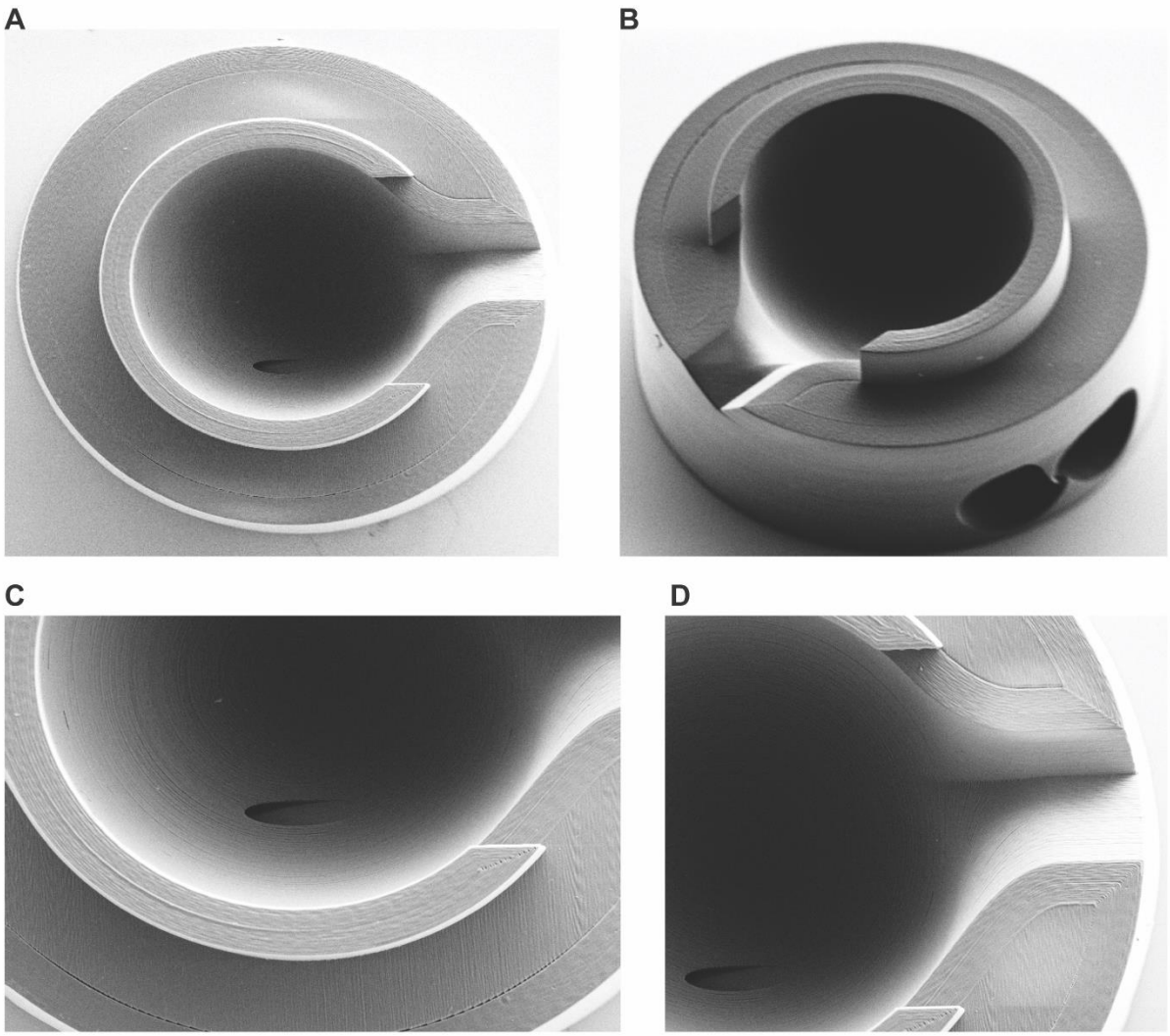

Figure 4.5 SEM images for a 240 μm stator with a slice thickness of 0.25 μm. (A) Top view of the stator. (B) An isometric view of the stator. The two holes on the side are for fiber optics. (C) Expansion of the gas inlet. (D) Expansion of the gas exhaust.

4.3.2 240 μm Stator on the Adaptor

After the UV lithography (**Figure 4.2 A-E**), a 240 μm stator was fabricated on the 10mm×10mm adaptor by 3D-DLW (**Figure 4.2 F**). However, the SEM images reveal that the stator fabrication was sub-optimal (**Figure 4.6 A-B**): the cup of the stator was not smooth; the fiber optic holes went through the cup; the gas inlet was not fabricated successfully. The main reason could be the focusing issue of the laser during fabrication. In 3D-DLW, the laser beam focuses at a specific angle to provide the desired precision. The dry photoresists around the cut might have blocked the

laser beam (**Figure 4.6 C**). Therefore, the laser beam could not focus well on the edge, leading to the sub-optimal precision in 3D-DLW.

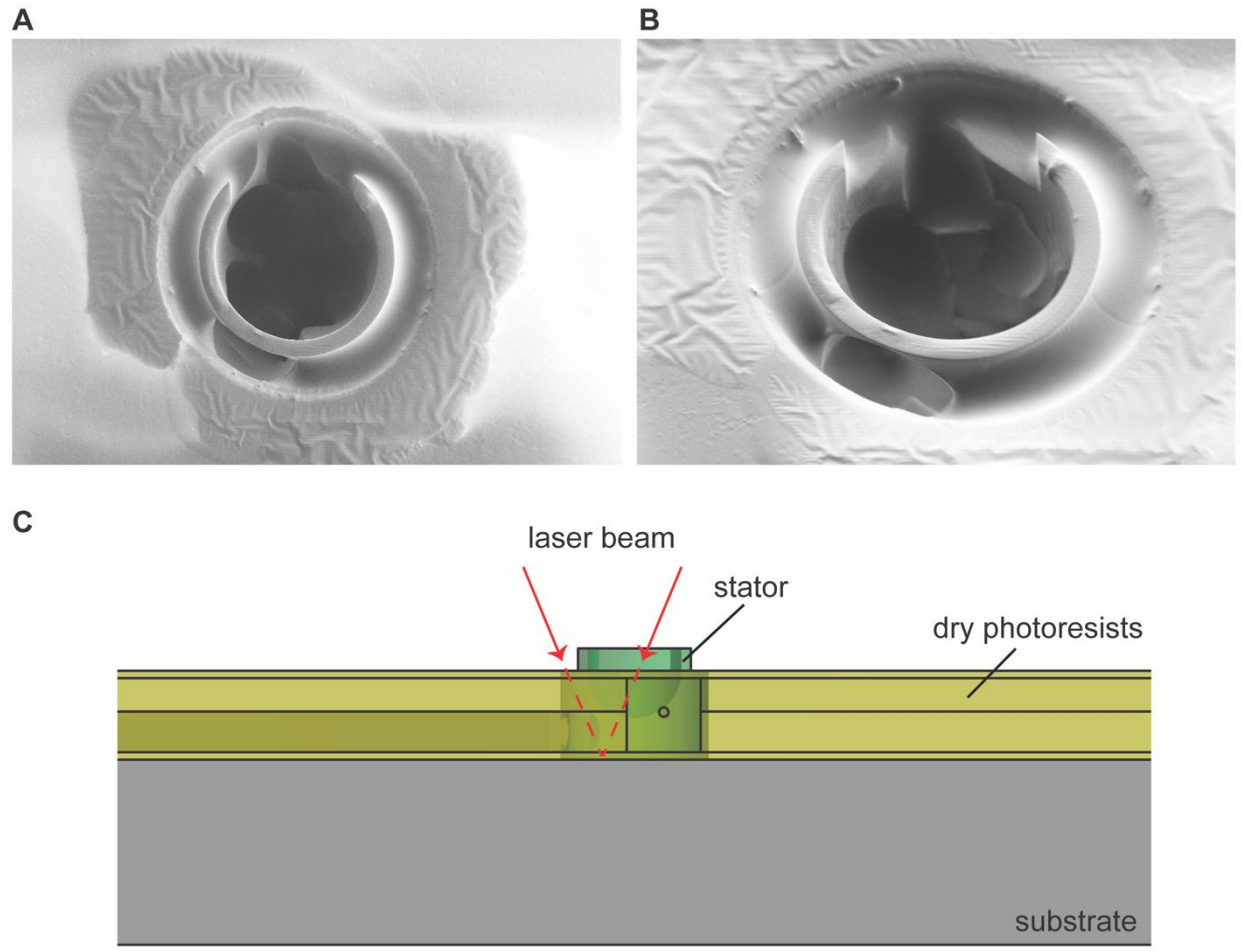

Figure 4.6 240 μm stator on the adaptor. (A) and (B) SEM images of a 240 μm stator which was directly fabricated on the adaptor. (C) Schematic illustrations of the laser beam blocked by the dry photoresists.

Another possible reason could be the sub-optimal conditions in the UV lithography process. Dry photoresists with different thicknesses require different exposure time and development time. From some preliminary results (not shown here), dry photoresist residues occurred on the bottom of the cut after the lithography process in **Figure 4.2 A-E**, which could also lead to sub-optimal precision in 3D-DLW.

In order to alleviate the focusing issue of the laser beam, future designs could be attempted where the lithography plate is flat on the top in order that the laser beam could be focused on any spot of the stator. More details of this design will be further discussed in the next section.

4.4 Conclusions and Outlook

The 240 μm spherical rotors and stators were successfully fabricated by 3D-DLW. Fabricating the 240 μm stator directly on the adaptor could be an effective way to install the sub-millimeter stators. However, the focusing issue of the laser beam caused sub-optimal precision in 3D-DLW. A new stator (**Figure 4.7 A-C**) and a new adaptor that houses the stator were designed (**Figure 4.7 D-E**) in order to solve the focusing issue mentioned above. Instead of fabricating a cylindrical cut on the adaptor, the new adaptor is now flat on the top. Thus, the laser beam can be focused on any spot of the stator to provide the desired precision during 3D-DLW (**Figure 4.7 D**). The gas stream can exit from a small hole on the top of the adaptor, leading to a flat surface on the top (**Figure 4.7 D**). After exiting from the adaptor, the gas stream can enter the bottom of the stator. The gas stream then enters a chamber before being directed into the cup to spin the spherical rotor (**Figure 4.7 A-C**).

In this design, the lithography process is also simplified so the optimal conditions is easier to achieve (**Figure 4.8**). By combing the dry photoresist with the same thickness, the gas channel can be fabricated on the adaptor. (**Figure 4.8 B-C**). Optimizing the parameters for dry photoresists with the same thickness is easier than combining dry photoresists with different thickness. In this design, the fiber optic holes are only included in the stator but excluded in the adaptor. However, the fiber optics can be cured by glue on the adaptor.

In addition to spinning frequency detection, NMR instrumentation must also consider transmit-receive coils. Coil geometries such as Helmholtz coils[28,29] and double helix dipole coils[30] could be beneficial for cryogenic DNP NMR due to the possibility of vertical sample exchange.

Sub-millimeter spherical resonators could be a potential strategy to improve microwave coupling for DNP. The microwave simulations have shown a spherical distribution of a tightly focused microwave beam[22]. Determining the appreciate size of sub-millimeter spherical resonators to improve the control over electron spins could pave the way towards pulsed DNP.

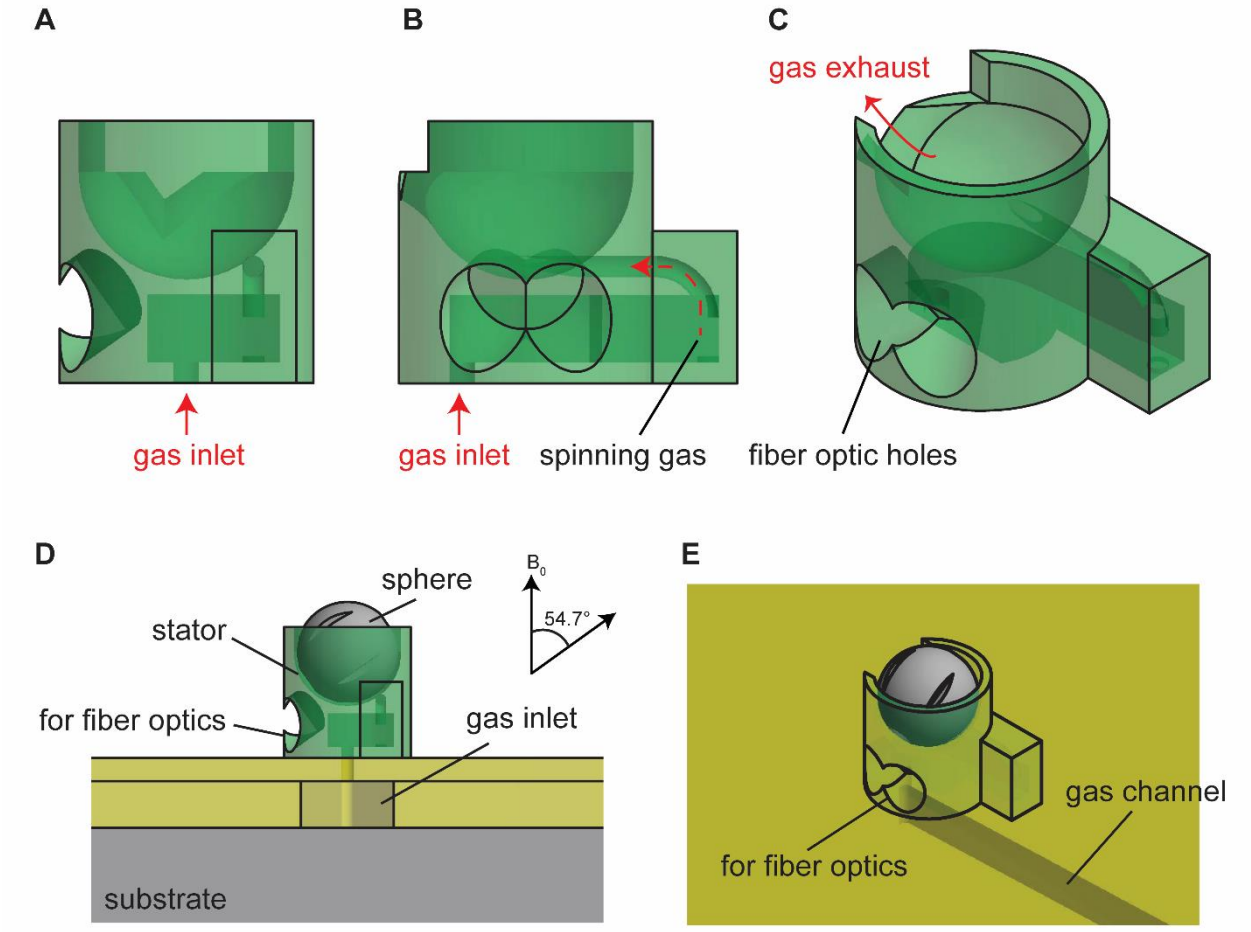

Figure 4.7 Proposed design for better fabrication in 3D-DLW. (A) The gas is introduced from the bottom, enters in a chamber, and is directed into the cup to spin the sphere. (B) and (C) Two separate isometric views show the gas flow path. (D) The lithography plate is designed to be flat on the top for 3D-DLW. (E) An isometric view shows how the spherical rotor and stator would be installed.

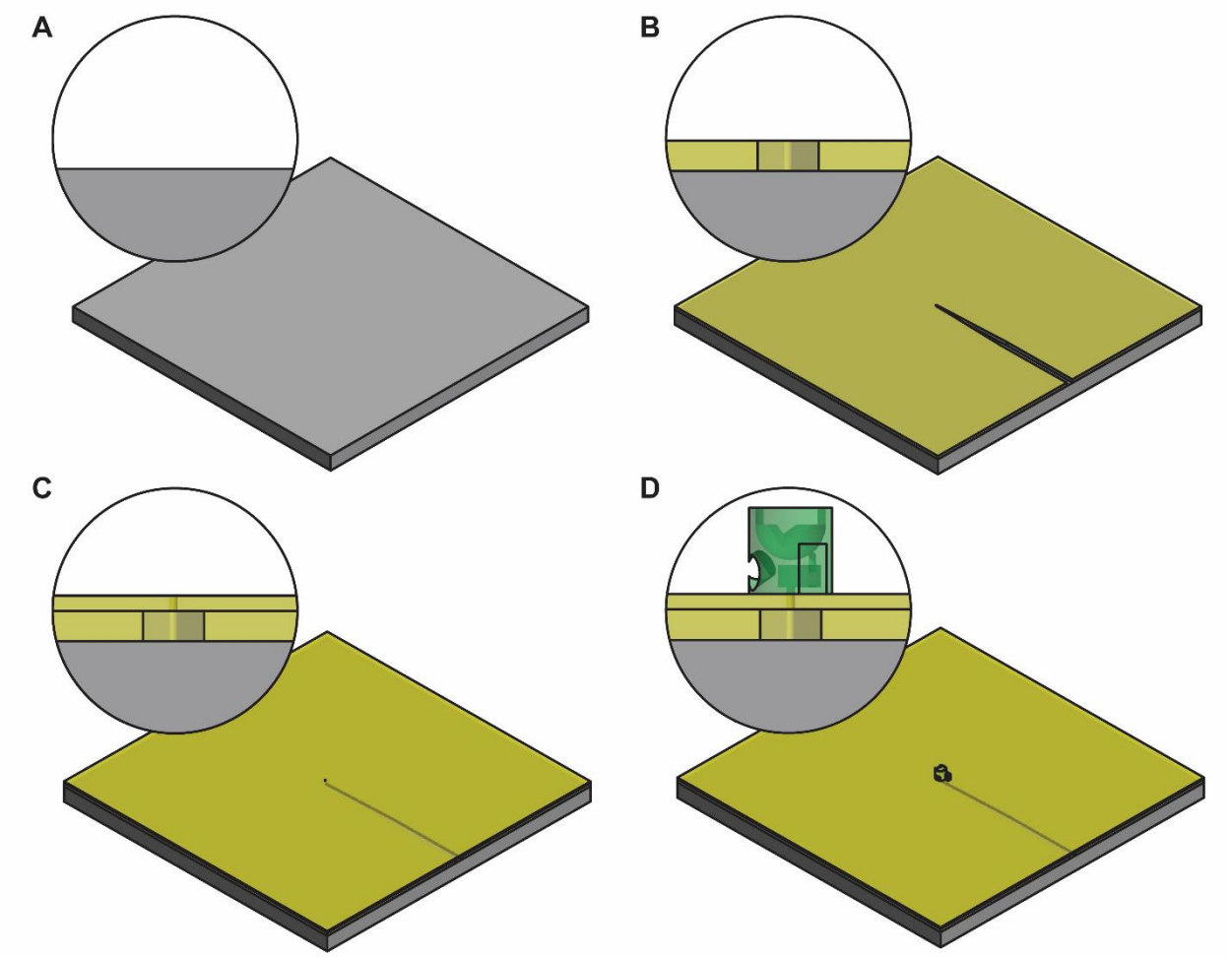

Figure 4.8 Schematic illustrations of the proposed microstructure fabrication by UV lithography and 3D-DLW. (A) A 10mm×10mm glass substrate. (B) First-layer dry resist with the gas inlet by combining two layers of 55 μm dry resist. (C) Second-layer dry resist with the gas channel directing up by one layer of 55 μm dry resist. (D) The stator fabricated by 3D-DLW.

Acknowledgement

This research is in collaboration with Professor Jan G. Korvink and Dr. Vlad Badilita at Karlsruhe Institute of Technology in Germany. We thank Stefan Hengsbach, Emil Mamleyev, Florian Rupp, Shyam Adhikari, Hossein Davoodi, and Dr. Lorenzo Bordonali for technical assistance and helpful discussion.

4.5 References

1. Lowe, I. J. Free induction decays of rotating solids. *Phys. Rev. Lett.* **2**, 285–287 (1959).
2. Andrew, E. R., Bradbury, A. & Eades, R. G. Nuclear Magnetic Resonance Spectra from a Crystal Rotated at High Speed. *Nature* **182**, 1659 (1958).

3. Schaefer, J. & Stejskal, E. O. Carbon-13 nuclear magnetic resonance of polymers spinning at the magic angle. *J. Am. Chem. Soc.* **98**, 1031–1032 (1976).

4. Herzfeld, J. & Berger, A. E. Sideband intensities in NMR spectra of samples spinning at the magic angle. *J. Chem. Phys.* **73**, 6021–6030 (1980).

5. Siemer, A. B., Ritter, C., Ernst, M., Riek, R. & Meier, B. H. High-Resolution Solid-State NMR Spectroscopy of the Prion Protein HET-s in Its Amyloid Conformation. *Angew. Chem. Int. Ed.* **44**, 2–5 (2005).

6. Hoop, C. L. *et al.* Huntingtin exon 1 fibrils feature an interdigitated β-hairpin–based polyglutamine core. *Proc. Natl. Acad. Sci.* **113**, 1546–1551 (2016).

7. Theint, T. *et al.* Species-dependent structural polymorphism of Y145Stop prion protein amyloid revealed by solid-state NMR spectroscopy. *Nat. Commun.* **8**, (2017).

8. Petkova, a. T. *et al.* Self-propagating, molecular-level polymorphism in Alzheimer's beta-amyloid fibrils. *Science (80-.).* **307**, 262–265 (2005).

9. Castellani, F. *et al.* Structure of a protein determined by solid-state magic-angle-spinning NMR spectroscopy. *Nature* **420**, 98–102 (2002).

10. Bertini, I. *et al.* High-resolution solid-state NMR structure of a 17.6 kDa protein. *J. Am. Chem. Soc.* **132**, 1032–1040 (2010).

11. Retel, J. S. *et al.* Structure of outer membrane protein G in lipid bilayers. *Nat. Commun.* **8**, 1–10 (2017).

12. Eddy, M. T. *et al.* Magic angle spinning nuclear magnetic resonance characterization of voltage-dependent anion channel gating in two-dimensional lipid crystalline bilayers. *Biochemistry* **54**, 994–1005 (2015).

13. Thongsomboon, W. *et al.* Phosphoethanolamine cellulose: A naturally produced chemically modified cellulose. *Science* **359**, 334–338 (2018).

14. Eckman, R., Alla, M. & Pines, A. Deuterium NMR in solids with a cylindrical magic angle sample spinner. *J. Magn. Reson.* **41**, 440–446 (1980).

15. Lee, J. N. *et al.* Cylindrical spinner and speed controller for magic angle spinning nuclear magnetic resonance. *Rev. Sci. Instrum.* **55**, 516–520 (1984).

16. Barnes, A. B. *et al.* Cryogenic sample exchange NMR probe for magic angle spinning dynamic nuclear polarization. *J. Magn. Reson.* **198**, 261–270 (2009).

17. Scott, F. J. *et al.* A Versatile Custom Cryostat for Dynamic Nuclear Polarization Supports Multiple Cryogenic Magic Angle Spinning Transmission Line Probes. *J. Magn. Reson.* **297**, 23–32 (2018).

18. Chen, P. *et al.* Magic angle spinning spheres. *Sci. Adv.* 1–8 (2018). doi:10.1126/sciadv.aau1540

19. Gao, C. *et al.* Four millimeter spherical rotors spinning at 28 kHz with double-saddle coils for cross polarization NMR. *J. Magn. Reson.* **303**, 1–6 (2019).

20. Xue, K. *et al.* Magic-Angle Spinning Frequencies beyond 300 kHz Are Necessary to Yield Maximum Sensitivity in Selectively Methyl Protonated Protein Samples in Solid-State NMR. *J. Phys. Chem. C* **122**, 16437–16442 (2018).

21. Penzel, S. *et al.* Spinning faster: protein NMR at MAS frequencies up to 126 kHz. *J. Biomol. NMR* **73**, 19–29 (2019).

22. Chen, P.-H., Gao, C. & Barnes, A. B. Perspectives on Microwave Coupling into Cylindrical and Spherical Rotors with Dielectric Lenses for Magic Angle Spinning Dynamic Nuclear Polarization. *J. Magn. Reson.* 1–8 (2019). doi:10.1016/j.jmr.2019.07.005

23. Maruo, S. & Fourkas, J. T. Recent progress in multiphoton microfabrication. *Laser Photonics Rev.* **2**, 100–111 (2008).

24. Von Freymann, G. *et al.* Three-dimensional nanostructures for photonics. *Adv. Funct. Mater.* **20**, 1038–1052 (2010).

25. Bückmann, T. *et al.* Tailored 3D mechanical metamaterials made by dip-in direct-laser-writing optical lithography. *Adv. Mater.* **24**, 2710–2714 (2012).

26. Maruo, S., Nakamura, O. & Kawata, S. Three-dimensional microfabrication with two-photon-absorbed photopolymerization. *Opt. Lett.* **22**, 132 (1997).

27. Farsari, M. & Chichkov, B. N. Materials processing: Two-photon fabrication. *Nat. Photonics* **3**, 450–452 (2009).

28. Spengler, N. *et al.* Micro-fabricated Helmholtz coil featuring disposable microfluidic sample inserts for applications in nuclear magnetic resonance. *J. Micromechanics Microengineering* **24**, (2014).

29. Spengler, N. *et al.* Heteronuclear micro-helmholtz coil facilitates μm-range spatial and sub-Hz spectral resolution NMR of nL-volume samples on customisable microfluidic chips. *PLoS One* **11**, 1–16 (2016).

30. Alonso, J., Soleilhavoup, A., Wong, A., Guiga, A. & Sakellariou, D. Double helix dipole design applied to magnetic resonance: A novel NMR coil. *J. Magn. Reson.* **235**, 32–41 (2013).

Chapter 5: Complementary Metal-Oxide-Semiconductor Low Noise Amplifier in Close Proximity to Receive Coil to Decrease Measurement Noise for Nuclear Magnetic Resonance

Excellent sensitivity in solid-state nuclear magnetic resonance (NMR) is required to investigate molecular structure and dynamics with atomic resolution. In contrast with directly increasing the NMR signal, decreasing measurement noise is an effective strategy to improve the signal-to-noise ratio (SNR). Installing a broadband, high-impedance complementary metal-oxide-semiconductor (CMOS) low noise amplifier (LNA) chip in close proximity to the receive coil has been demonstrated to decrease measurement noise. Here, in addition to installing the LNA chip, the receiving and transmitting circuits are separated in order to reduce the complexity of the receiving circuit and the resulting noise from the circuit. A printed circuit board (PCB) for the receiving circuit is designed for the receiving circuit and installed in the magic angle spinning (MAS) dynamic nuclear polarization (DNP) NMR probe head. The LNA chip along with the PCB has achieved a total voltage gain of 30 dB.

5.1 Introduction

Magic angle spinning (MAS) nuclear magnetic resonance (NMR) spectroscopy can be utilized to characterize molecular architectures[1–7]. However, excellent NMR sensitivity is required to study complicated biological systems. Different methods have been developed to improve the NMR sensitivity, including performing experiments at higher magnetic fields[8–10] or lower temperatures[11–13], improving filling factors by implementing inductively-coupled coils[14–18], and

boosting the sensitivity using hyperpolarization techniques such as dynamic nuclear polarization (DNP)[19–24].

In addition to directly increasing the NMR signal, decreasing measurement noise can effectively improve the signal-to-noise ratio (SNR) in NMR spectroscopy. In magnetic resonance imaging (MRI), an improved SNR has been demonstrated by placing a broadband, high-impedance complementary metal-oxide-semiconductor (CMOS) low noise amplifier (LNA) chip in close proximity to the receive coil[25]. Here, a similar strategy is proposed for the custom-built MAS DNP NMR spectrometer. The LNA chip is installed close to the receive coil in order to amplify the NMR signal immediately after the detection. Moreover, the receiving and transmitting circuits of the probe are separated, so junction noise from the transmitting circuit does not diminish the SNR in the receiving circuit.

5.2 Designs

5.2.1 Separation of Receiving and Transmitting Circuits

The transmit and receive coils, in separate circuits, are orthogonal to each other; thus, pulsing in the transmitting circuit does not interfere with detection in the receiving circuit. A 4-channel transmission-line probe for spherical rotors is demonstrated as an example of a transmitting circuit[26–28]. The transmitting circuit, which can be replaced with another NMR probe, contains a double-saddle transmit coil and several electronic components such as capacitors rated to handle high-power pulses[26] (**Figure 5.1 A**). Junctions between these electronic components can cause noise in the transmitting circuit. Separating the transmitting and receiving circuits can reduce the complexity in the receiving circuit and prevent the junction noise from interfering with the SNR in the receiving circuit.

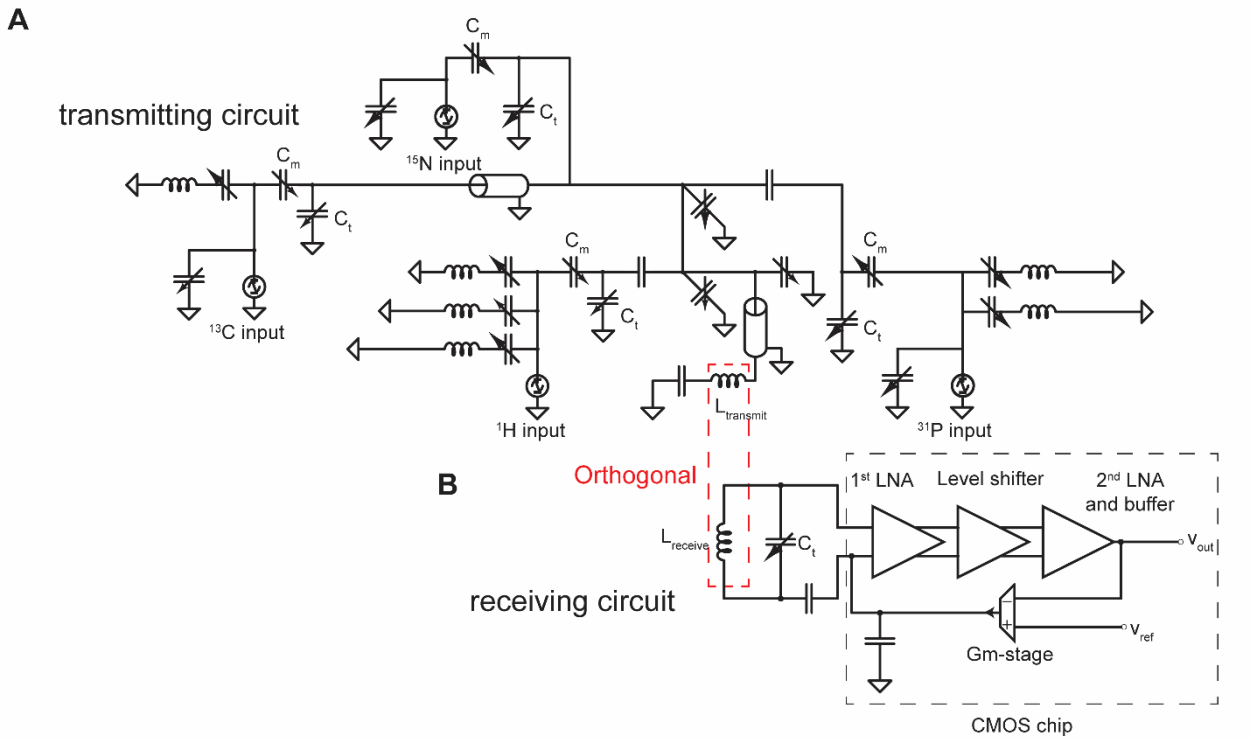

Figure 5.1 Circuit diagram of the separate transmitting and receiving circuits. (A) The transmit coil is part of a 4-channel transmission-line probe. (B) The receive coil only connects to the CMOS LNA chip, a variable capacitor, and several tiny capacitors.

The receiving circuit, on the other hand, contains only a double-saddle receive coil orthogonal to the transmit coil, the CMOS LNA chip in close proximity to the receive coil, a digitally programmable variable capacitor, and several millimeter-scale capacitors that are not rated to handle high-power NMR pulses (**Figure 5.1 B**). The receive coil can be tuned to the desired operating frequencies by a single variable capacitor, which is a digitally programmable capacitor such as IXYS NCD 2400 (IXYS Corporation, CA, USA)[25]. The entire receiving circuit can be connected to a printed circuit board (PCB) and installed in the MAS DNP NMR probe head.

5.2.2 Printed Circuit Board (PCB)

A PCB was designed and customized to install the receiving circuit in the MAS DNP NMR probe head. The PCB contains the receiving circuit including the receive coil, the LNA chip, the tuning capacitor, and two connectors for the power supply and the spectrometer (**Figure 5.2 A**). The

connectors are housed on the right side of the PCB, providing the cables a better access to connecting with the power supply and the spectrometer through an additional hole drilled on the probe head base. **Figure 5.2 B** shows a picture of the customized PBC after the LNA chip is connected, and **Figure 5.2 C** shows the PCB with the addition of several millimeter-scale capacitors and the two connectors for the power supply and the spectrometer.

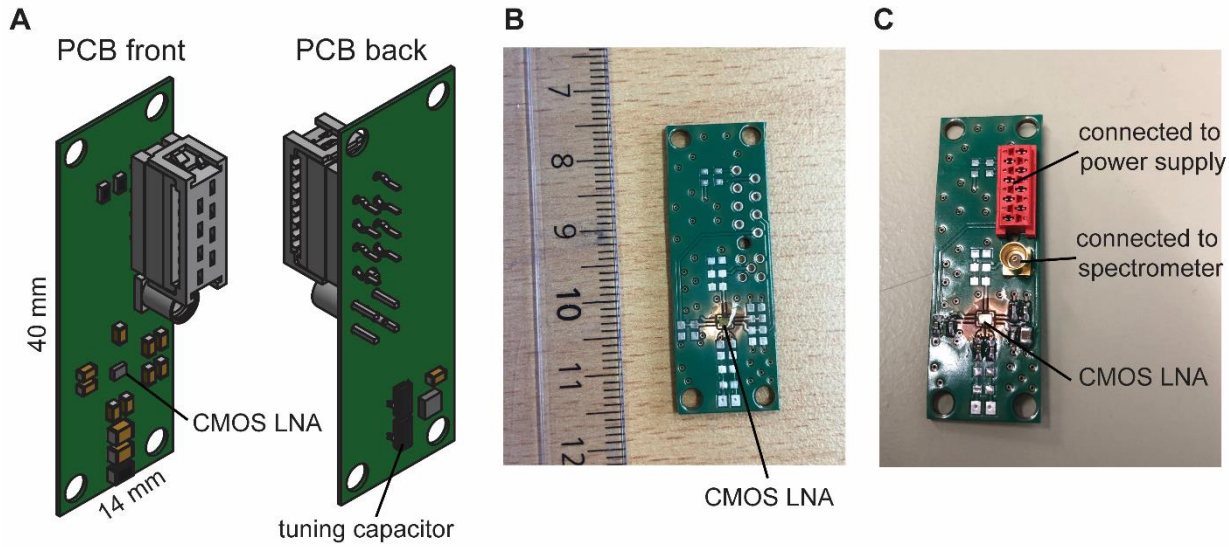

Figure 5.2 PCB design for installing the receiving circuit. (A) Schematic illustrations of the PCB with a size of 40mm×14mm that can be housed on one of the legs in the probe head. (B) The customized PBC including the LNA chip. (C) The PCB with the addition of several capacitors and two connectors.

5.2.3 Implementation in MAS DNP NMR probe

The PCB with a size of 40mm×14mm can be housed on one of the legs in the MAS DNP NMR probe head (**Figure 5.3 A**). The additional hole on the probe head base is drilled for the cables to be connected with the power supply and the spectrometer. The double-saddle transmit coil, orthogonal to the receive coil, is connected to the 4-channel transmission-line probe (**Figure 5.3 B**).

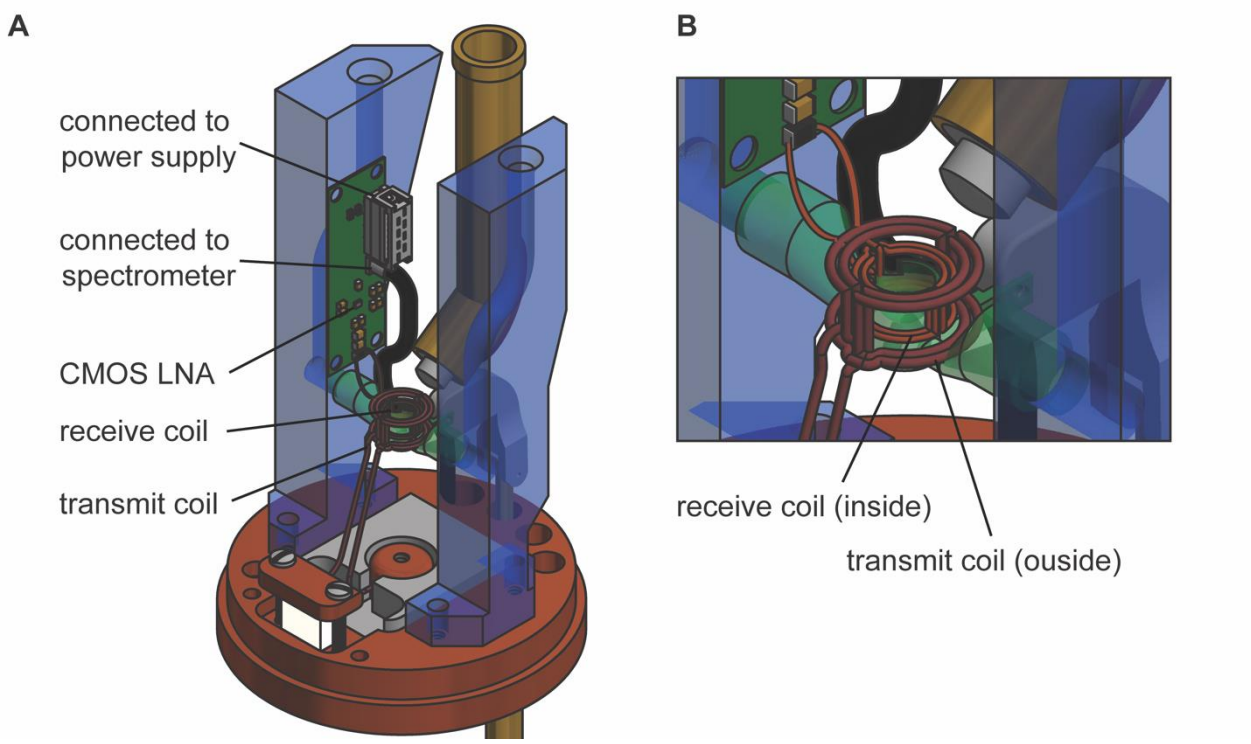

Figure 5.3 Implementation of PCB, receive coil, and transmit coil in the MAS DNP NMR probe. (A) The receive coil is connected to the PCB, and the transmit coil is connected to the probe head base. (B) Expansion of (A) shows the receive and transmit coils, orthogonal to each other.

5.3 Electrical Measurements

In order to verify the performance of the LNA chips, the voltage gain is measured by employing a network analyzer along with a 180° power splitter and a broadband 50 Ω input termination at the LNA input[25]. The voltage gain, which indicates the performance of pre-amplification, can be expressed in decibels (dB) and is given by

$$x = 20\ \log\left(\frac{V}{V_0}\right) \qquad (5.1)$$

where x is the voltage gain in dB, V_0 is the input voltage, and V is the amplified voltage. The relation between them can also be given by

$$V = V_0 \cdot 10^{\frac{x}{20}} \qquad (5.2)$$

Measurements of the voltage gain as a function of frequency are usually carried out on several different LNA chips to characterize the electrical properties. The CMOS LNA chip on the PCB designed here has achieved a total voltage gain of 30 dB, indicating $V = 32\,V_0$.

5.4 Discussion and Outlook

In comparison with 30 dB ($V = 32\,V_0$), the same CMOS LNA chip on a different PCB has achieved a total voltage gain of 44 dB ($V = 158\,V_0$) for MRI[25]. The sub-optimal performance could be resulted from the different PCB or the variant performance of the LNA chips. Optimization on the PCB designed here and the LNA chips is critical before the LNA chip is implemented for NMR experiments.

Installing the CMOS LNA chip in the probe head paves the way towards cooling the receiving circuit to cryogenic temperatures. Cooling the electronic components in the receiving circuit could significantly decrease the measurement noise and thus increase the SNR for MAS DNP NMR. Modifications of the CMOS LNA and PCB designs might be necessary for low temperature experiments because current designs are for room temperature. Capacitors suitable for cryogenic temperatures also need to be considered.

Acknowledgement

This research is in collaboration with Professor Jens Anders at University of Stuttgart in Germany. We thank Heiko Bürkle for technical assistance and helpful discussion.

5.5 References

1. Hoop, C. L. *et al.* Huntingtin exon 1 fibrils feature an interdigitated β-hairpin–based polyglutamine core. *Proc. Natl. Acad. Sci.* **113**, 1546–1551 (2016).
2. Theint, T. *et al.* Species-dependent structural polymorphism of Y145Stop prion protein amyloid revealed by solid-state NMR spectroscopy. *Nat. Commun.* **8**, (2017).

3. Petkova, a. T. *et al.* Self-propagating, molecular-level polymorphism in Alzheimer's beta-amyloid fibrils. *Science (80-.).* **307**, 262–265 (2005).

4. Castellani, F. *et al.* Structure of a protein determined by solid-state magic-angle-spinning NMR spectroscopy. *Nature* **420**, 98–102 (2002).

5. Retel, J. S. *et al.* Structure of outer membrane protein G in lipid bilayers. *Nat. Commun.* **8**, 1–10 (2017).

6. Thongsomboon, W. *et al.* Phosphoethanolamine cellulose: A naturally produced chemically modified cellulose. *Science* **359**, 334–338 (2018).

7. McCrate, O. A., Zhou, X., Reichhardt, C. & Cegelski, L. Sum of the parts: Composition and architecture of the bacterial extracellular matrix. *J. Mol. Biol.* **425**, 4286–4294 (2013).

8. Samoson, A., Tuherm, T. & Gan, Z. High-field high-speed MAS resolution enhancement in 1H NMR spectroscopy of solids. *Solid State Nucl. Magn. Reson.* **20**, 130–136 (2001).

9. Moser, E., Laistler, E., Schmitt, F. & Kontaxis, G. Corrigendum: Ultra-High Field NMR and MRI–The Role of Magnet Technology to Increase Sensitivity and Specificity. *Front. Phys.* **5**, 1–15 (2017).

10. Berthier, C., Horvatić, M., Julien, M. H., Mayaffre, H. & Krämer, S. Nuclear magnetic resonance in high magnetic field: Application to condensed matter physics. *Comptes Rendus Phys.* **18**, 331–348 (2017).

11. Ripmeester, J. A. & Ratcliffe, C. I. Low-temperature cross-polarization/magic angle spinning carbon-13 NMR of solid methane hydrates: structure, cage occupancy, and hydration number. *J. Phys. Chem.* **92**, 337–339 (1987).

12. Kloepper, K. D. *et al.* Temperature-dependent sensitivity enhancement of solid-state NMR spectra of α-synuclein fibrils. *J. Biomol. NMR* **39**, 197–211 (2007).

13. Sesti, E. L. *et al.* Magic angle spinning NMR below 6 K with a computational fluid dynamics analysis of fluid flow and temperature gradients. *J. Magn. Reson.* **286**, 1–9 (2018).

14. Sakellariou, D., Goff, G. Le & Jacquinot, J. F. High-resolution, high-sensitivity NMR of nanolitre anisotropic samples by coil spinning. *Nature* **447**, 694–697 (2007).

15. Badilita, V. *et al.* Microfabricated inserts for magic angle coil spinning (MACS) wireless NMR spectroscopy. *PLoS One* **7**, (2012).

16. Spengler, N., While, P. T., Meissner, M. V., Wallrabe, U. & Korvink, J. G. Magnetic Lenz lenses improve the limit-of-detection in nuclear magnetic resonance. *PLoS One* **12**, 1–17 (2017).

17. Schoenmaker, J., Pirota, K. R. & Teixeira, J. C. Magnetic flux amplification by Lenz lenses. *Rev. Sci. Instrum.* **84**, 1–4 (2013).

18. Jouda, M. *et al.* A comparison of Lenz lenses and LC resonators for NMR signal

enhancement. *Concepts Magn. Reson. Part B Magn. Reson. Eng.* **47B**, 1–10 (2017).

19. Ni, Q. Z. *et al*. High frequency dynamic nuclear polarization. *Acc. Chem. Res.* **46**, 1933–1941 (2013).

20. Rossini, A. J., Zagdoun, A., Lelli, M., Lesage, A. & Cop, C. Dynamic Nuclear Polarization Surface Enhanced NMR Spectroscopy. *Acc. Chem. Res.* **46**, (2013).

21. Tycko, R. NMR at Low and Ultralow Temperatures. *Acc. Chem. Res.* **46**, 1923–1932 (2013).

22. Maly, T. *et al.* Dynamic nuclear polarization at high magnetic fields. *J. Chem. Phys.* **052211**, (2008).

23. Barnes, A. B. *et al.* High-field dynamic nuclear polarization for solid and solution biological NMR. *Appl. Magn. Reson.* **34**, 237–263 (2008).

24. Can, T. V., Ni, Q. Z. & Griffin, R. G. Mechanisms of dynamic nuclear polarization in insulating solids. *J. Magn. Reson.* **253**, 23–35 (2015).

25. Horneff, A. *et al.* A New CMOS Broadband, High Impedance LNA for MRI Achieving an Input Referred Voltage Noise Spectral Density of 200pV/Hz√. *2019 IEEE Int. Symp. Circuits Syst.* 1–5 (2019). doi:10.1109/iscas.2019.8702445

26. Scott, F. J. *et al.* A Versatile Custom Cryostat for Dynamic Nuclear Polarization Supports Multiple Cryogenic Magic Angle Spinning Transmission Line Probes. *J. Magn. Reson.* **297**, 23–32 (2018).

27. Chen, P. *et al.* Magic angle spinning spheres. *Sci. Adv.* 1–8 (2018). doi:10.1126/sciadv.aau1540

28. Gao, C. *et al.* Four millimeter spherical rotors spinning at 28 kHz with double-saddle coils for cross polarization NMR. *J. Magn. Reson.* **303**, 1–6 (2019).

Chapter 6: Conclusions and Outlook

Advanced MAS DNP NMR instrumentation has been developed and improved by introducing spherical rotors for stable and fast spinning, analyzing dielectric lenses to improve microwave coupling, and separating the receiving and transmitting circuits along with installing pre-amplifiers in close proximity to receive coils to reduce measurement noise. MAS spheres, which require only one single gas stream to perform stable spinning, improve cryogenic DNP instrumentation due to a simplified vertical sample exchange and a better access for microwave illumination. Implementation of sub-millimeter spherical rotors, a potential path towards ultra-fast MAS and improved NMR spectroscopy, is under development. Moreover, in order to achieve time-domain DNP that requires intense microwave fields, dielectric lenses for cylindrical and spherical rotors are developed and analyzed to improve the electron Rabi frequency. To further improve the SNR by decreasing measurement noise, the receiving and transmitting circuits are separated while the broadband, high impedance CMOS LNA chip is installed in close proximity to the receive coil.

6.1 MAS Spheres

Spherical rotors have been demonstrated to be spun stably at the magic angle. 3D-printed stators that house the spherical rotors contain only one single gas stream that serves as drive and bearing gas to spin the spherical rotor and variable temperature control for thermostating. The 9.5 mm OD spherical rotors can be spun at frequencies up to 4.6 kHz with N_2 (g) and 10.6 kHz with He (g). Using a resistive heating feedback control enables a spinning frequency stability of ±1 Hz. Additionally, implementing spherical rotors allows a simplified vertical sample exchange and provides better access for microwave illumination for cryogenic DNP.

Access to smaller rotors lead to faster spinning and improved spectral resolution; therefore, 240 μm OD spherical rotors and stators are fabricated by three-dimensional direct laser writing (3D-DLW). An adaptor that contains a gas channel for spinning and holes for fiber optics improves handling of the sub-millimeter stator. Fabricating the 240 μm stators directly on the adaptor is a potential strategy to install the sub-millimeter stators. Despite sub-optimal conditions in the current attempt, future designs are proposed to improve the implementation. Ultra-fast MAS spheres will significantly improve spectral resolution by attenuating proton homonuclear couplings (>110 kHz) or even hyperfine interaction (>1 MHz).

6.2 Microwave Coupling

Dielectric lenses are designed for cylindrical and spherical rotors to effectively couple the microwave power and increase the electron Rabi frequency, ν_{1s}. Using a commercial simulation package, we solve the Maxwell equations, determine the propagation and focusing of millimeter waves (198 GHz), and calculate time-independent ν_{1s}. In comparison with conventional 3.2 mm OD cylindrical rotors (0.38 MHz), the ν_{1s} is improved to 1.5 MHz by implementing a Teflon lens and decreasing the sample size. To further improve the instrumentation, a Teflon lens is installed in a 9.5 mm OD cylindrical rotor to avoid microwave diffractions through the RF coil, losses from penetration through the rotor wall, and mechanical limitations of the separation between the lens and sample. Additionally, to access fast spinning while also increasing ν_{1s}, microwave coupling into MAS spheres is analyzed. Implementing a double-lens insert into a 9.5 mm OD spherical rotor improves the computed ν_{1s} to 2.5 MHz. A 0.5 mm diamond sphere with a computed ν_{1s} of 2.2 MHz is proposed to improve the control over electron spins for the future.

6.3 Future Directions

6.3.1 Implementation of Sub-millimeter Spherical Rotors

MAS DNP NMR implementation must consider spinning gas, spinning frequency detection, transmit-receive coils, and sample exchange. In addition to UV lithography, micro-machining could be an effective strategy to fabricate the adaptor for the sub-millimeter stators. Transmit-receive coil geometries, such as Helmholtz coils[1,2] and double helix dipole coils[3], enable the possibility of vertical sample exchange, which is beneficial for cryogenic DNP.

6.3.2 Spherical Resonators

Microwave resonators are commonly employed to enhance the electron Rabi frequency for DNP [4–6]. Due to the spherical distribution of a tightly focused microwave beam shown in **Figure 3.3 F**, spherical resonators are proposed to match the natural geometry of the microwave intensity. Turning the sphere's body into a resonant cavity could be a potential strategy to enhance the electron Rabi frequency. Materials with high dielectric constants are promising resonant cavities. The diameter of the spherical resonator, depending on the microwave frequency and the dielectric constant of the transmission medium, is a critical parameter. The simulated microwave distribution of a 0.5 mm diamond sphere shows a tightly focused microwave beam (**Figure 3.4 F**). Currently, the size of spherical resonators is being optimized between 0.5 mm and 1.0 mm.

6.3.3 Pre-amplifier at Cryogenic Temperature

Instead of directly increasing the NMR signal, decreasing measurement noise is another approach to improve NMR instrumentation. Separating the receiving and transmitting circuits and installing the LNA chip in close proximity of the NMR receive coil is a promising strategy to decrease measurement noise. Installing the LNA chip and the receiving circuit in the probe head enables the possibility of cooling the entire receiving circuit to cryogenic temperatures, which could lead to enormously low measurement noise.

6.4 References

1. Spengler, N. *et al.* Micro-fabricated Helmholtz coil featuring disposable microfluidic sample inserts for applications in nuclear magnetic resonance. *J. Micromechanics Microengineering* **24**, (2014).

2. Spengler, N. *et al.* Heteronuclear micro-helmholtz coil facilitates μm-range spatial and sub-Hz spectral resolution NMR of nL-volume samples on customisable microfluidic chips. *PLoS One* **11**, 1–16 (2016).

3. Alonso, J., Soleilhavoup, A., Wong, A., Guiga, A. & Sakellariou, D. Double helix dipole design applied to magnetic resonance: A novel NMR coil. *J. Magn. Reson.* **235**, 32–41 (2013).

4. Denysenkov, V. & Prisner, T. Liquid state Dynamic Nuclear Polarization probe with Fabry-Perot resonator at 9.2 T. *J. Magn. Reson.* **217**, 1–5 (2012).

5. Kiss, S. Z. *et al.* A microwave resonator integrated on a polymer microfluidic chip. *J. Magn. Reson.* **270**, 169–175 (2016).

6. Scott, F. J. *et al.* Magic angle spinning NMR with metallized rotors as cylindrical microwave resonators. *Magn. Reson. Chem.* **56**, 831–835 (2018).